Microfluidic Sample Preparation for High-Resolution EM and Single Cell Analysis

Inauguraldissertation

Zur
Erlangung der Würde eines Doktors der Philosophie
vorgelegt der
Philosophisch – Naturwissenschaftlichen Fakultät
der Universität Basel

von

Luca Rima

2021

Genehmigt von der Philosophisch-Naturwissenschatlichen Fakultät
auf Antrag von Dr. Thomas Braun, Prof. Dr. Henning Stahlberg,
Prof. Dr. Timm Maier & Prof. Dr. Wanda Kukulski

Basel, den 15. Dezember 2020

Prof. Dr. Martin Spiess, Dekan

Abstract

To understand and explain biological processes, the functions of the involved biological macromolecules must be known. These functions are directly linked to their three-dimensional structures and conformations. Therefore, knowledge of these structures and their dynamics is essential for understanding and can be used, for example, for the development of pharmaceutical products. In the past, X-ray crystallography (XRC) or nuclear magnetic resonance (NMR) were commonly used for structure elucidation. However, both techniques make high demands on the sample, which greatly limits specimen selection. In recent years, cryogenic electron microscopy (cryo-EM) has gained more and more importance. Formerly a niche technology, it has become the method of choice for many scientists due to continued developments in instrumentation, electron detectors, and data processing. Among its advantages are that smaller sample sizes are required and that crystallization is unnecessary. This allows the investigation of new, previously unavailable samples. However, not all samples can be analyzed, and cryo-EM is also limited if problems occur with expression, purification, or sample preparation. Yet these areas have hardly changed compared to the otherwise enormous progress that has been made in the field and therefore represent the biggest bottleneck in the cryo-EM pipeline today. Therefore, new methods are required to overcome the existing limitations. One approach is the use of microfluidic systems for sample preparation. This is possible because the number of particles required for successful structure elucidation is $\sim 10^4$ to $\sim 10^6$, and the required volumes are in the nanolitre range. Such a microfluidic approach is now the focus of the following thesis. Primarily, the system for sample preparation is presented. Alongside samples for cryo-EM, samples for negative staining EM can also be prepared. The system is also capable of lysing single cells and processing their lysate. Afterward, a new module of this system will be discussed, which improves the EM grid preparation and offers new possibilities to influence the sample preparation process. Furthermore, a method is presented that allows the isolation of proteins from minute amounts of starting material, which can then be directly prepared for structure elucidation by cryo-EM. The last part is dedicated to the combination of the microfluidic system with other techniques that can provide complementary information to EM analysis. We demonstrate that the use of this microfluidic system for sample purification and sample preparation has decisive advantages over classical methods. Therefore, it will help the future elucidation of structures that are currently still unattainable. Additionally, we show that the system is very versatile and thus opens up completely new experimental possibilities that go beyond structural elucidation.

Acknowledgements

Throughout my work I was always accompanied and supported by many people. Without them all of this would not have been possible.
First of all I would like to thank Thomas Braun. Thomas has made it possible for me to work on this exciting project, has always supported and advised me when necessary and has given me the opportunity to work freely and pursue my goals. My thanks also go to Henning Stahlberg, who gave me valuable input and who, as director, is responsible for the great atmosphere in which I was able to work and gave me access to a well-functioning EM-infrastructure. I also thank Timm Maier and Wanda Kukulski for being members of my PhD-advisory committee.
For the organizational and bureaucratic part I would like to thank Karen Bergmann, who has taken a lot of work off my hands over the years. For the support in the wet lab and for the organization of the orders I would like to thank Frank Lehmann.
Many thanks also to Rosmarie Sütterlin, who has always supported me in my work with cells. For EM matters I could count on the help of various people. Kenneth Goldie, Mohamed Chami, Lubomir Kovacik and Ariane Fecteau-LeFebvre. I would like to thank all of you at this point.
In all these years I have also been able to work with many other colleagues, for which I would like to thank them all. These include: Andri Fränkl, Michael Zimmermann, Xavier Wildermuth, Thomas Stohler, Paolo Oliva, Anastasia Syntychaki, Ricardo Righetto, Fabian Heule, Claudio Schmidli, Stefan Albiez, Cedric Leu, Andrej Bieri, Patrick Lattner, Jan Eisenmann and Stefan Arnold. Among these persons, some are particularly noteworthy. Stefan Arnold, who did an excellent job in the run-up to this project and introduced me very well to the whole topic. Claudio Schmidli, who was always friendly and helpful and did valuable work, and Paolo Oliva, who with his great knowledge and character has always been a great support. I am glad that I had the opportunity to work with such great people and scientists like you. Thank you very much.
At this point I would like to thank the remaining people of C-CINA, who all contributed to the good working atmosphere.
Many thanks also to Christian Berchtold from the Fachhochschule Nordwestschweiz for the good collaboration and the interesting discussions and to the mechanical workshop of the Biozentrum at the University of Basel for the technical support in the production of various parts.
And last but not least I would like to thank my whole family and all my friends. Especially my parents and my sister, who have always supported me, and my girlfriend and my daughter, who are always there for me and always back me up.

Contents

1. Introduction **3**
1.1. Sample Preparation 5
1.2. Properties of Thin Films During Sample Preparation 13
1.3. Single and Few Cell Analysis 24

2. Microfluidic Sample Preparation for Transmission Electron Microscopy **31**
2.1. Introduction 32
2.2. Protocol 34
2.3. Representative Results 45
2.4. Discussion 50

3. The *climateJet* - A New Tool for Grid Preparation for High-Resolution Cryogenic Electron Microscopy **55**
3.1. Introduction 56
3.2. Experimental Section 57
3.3. Results 59
3.4. Discussion 65
3.5. Conclusion 65

4. Microfluidic Sample Purification for Transmission Electron Microscopy Using Magnetic Microspheres **71**
4.1. Significance Statement 72
4.2. Introduction 72
4.3. Results 73
4.4. Conclusion 78
4.5. Material and Methods 80

5. Cell Analysis for Correlative Metabolomics and Targeted Proteomics **93**
5.1. Introduction 94
5.2. Experimental Section 95
5.3. Results 98
5.4. Discussion 102
5.5. Conclusion 103

6. Conclusion and Outlook **107**

A. *cryoWriter* setup **111**

List of Abbreviations **117**

List of Symbols **119**

List of Figures **121**

List of Tables **123**

References **125**

Thesis Overview

The aim of this thesis is to present a microfluidic sample preparation method together with its latest developments. Furthermore, the preparation of single cells for correlative metabolomics and proteomics is discussed. To this end, the following topics are covered:

- **Chapter 1** provides an overview of the current status of sample preparation for transmission electron microscopy. Furthermore, the properties of thin films, which play a major role in sample preparation, are reviewed. Finally, the importance of single cell research is discussed, with emphasis on related mass spectrometry techniques and their combination with our single cell preparation method.
- **Chapter 2** is a detailed description and instruction of sample preparation using the *cryoWriter* setup.
- **Chapter 3** describes a new feature for sample preparation with the *cryoWriter* setup that provides improved and extended control over the grid preparation process.
- **Chapter 4** introduces a new microfluidics module that enables purification of samples immediately prior to grid preparation.
- **Chapter 5** addresses the combination of single cell lysis with mass spectrometry and reverse-phase protein arrays for correlative metabolomics and proteomics.
- **Chapter 6** summarizes the thesis and gives an outlook on future developments and projects.
- **Appendix A** gives a detailed overview of the structure of the *cryoWriter* setup, which is discussed throughout the thesis.

1. Introduction

Knowledge of the three-dimensional structure of biological macromolecules is essential to understand their mechanisms and functions and to comprehend the biological processes in which they are involved. Today, three main techniques are used to study these structures. X-ray crystallography (XRC), nuclear magnetic resonance spectroscopy (NMR) and cryogenic electron microscopy (cryo-EM). Each of them has their own advantages and disadvantages. XRC has long been the predominant technology and is still widely used today. Because of its high efficiency, XRC is interesting for many scientists because it enables them to obtain high-resolution structures with short data acquisition times and comparatively low computational effort. Once suitable crystallization conditions are found, XRC delivers structures quickly, reproducibly and with a high throughput. Therefore, XRC is still the preferred technology when large amounts of samples have to be screened, as for example in the pharmaceutical industry. However, crystallization conditions must always be found first, which can prove difficult or even impossible. The reasons for this are that normally large sample quantities are required and membrane proteins, highly glycosylated proteins and large and flexible proteins are inherently difficult to crystallize. If a target cannot be crystallized then structure determination with XRC is not possible.

Contents

1.1. Sample Preparation **5**
1.2. Properties of Thin Films During Sample Preparation . . **13**
1.3. Single and Few Cell Analysis **24**

An alternative to XRC is NMR. NMR can be used to study biological macromolecules in solution. It provides information about the dynamics of the molecules in contrast to XRC, which only provides a snapshot in a given conformation. However, NMR also requires large sample quantities and high concentrations and can only be used for small proteins, small RNAs or even single domains due to the enormous computing effort involved. Furthermore, NMR often depends on isotope enrichment [Nogales 2015].

The last of these three main methods is cryo-EM. Although its origins date back to the 1970s and 1980s [Taylor & Glaeser 1974, Lepault *et al.* 1983, Dubochet *et al.* 1988], the breakthrough of this technology occurred only in the last decade, driven by developments in image processing as well as in electron detection [Lyumkis 2019]. Especially the development of direct electron detectors (DED) has led to a dramatic improvement of the achievable resolution. These detectors not only have a much higher contrast than the charge-coupled device (CCD) cameras used previously,

but their fast readout rate also enables the recording of videos instead of single images, which allows the mathematical correction of beam-induced motions of the sample. Together with the emergence of maximum-likelihood image processing routines [Scheres 2012], which permit averaging thousands of projections of individual particles and reconstructing a three-dimensional structure from them, this has led to the so-called resolution revolution in 2014 [Kuhlbrandt 2014] and to the award of the Nobel Prize in Chemistry to J. Dubochet, R. Henderson and J. Frank in 2017. Today's common approach in cryo-EM is called single particle analysis (SPA) and has several advantages over XRC and NMR. Among those advantages are the absence of the necessity to crystallize samples and the reduced sample volumes required. This facilitates the study of large and/or dynamic macromolecules in their native state, including post-translational modifications and other samples that were previously unattainable. Additionally, different conformational states can be observed in a single experiment, which can provide information about the dynamics of the sample [Renaud *et al.* 2018]. Combined these advantages alongside a much higher throughput have often made cryo-EM the method of choice today.

While hardware and software have evolved immensely, sample preparation and protein purification have not changed significantly and now represent the main bottleneck in the cryo-EM pipeline. In the following sections, EM sample preparation and sample purification are discussed in more detail. It will be shown which methods are currently used, which difficulties exist and where developments are taking place.

Although structural biology is compelling in elucidating biological phenomena, it is not enough to comprehend everything. Therefore, other methods must be employed that can provide complementary information. If different methods are cleverly combined, their individual strengths can be exploited and new experimental approaches become possible. In this context, the last part of this introduction is dedicated to single cell analysis using mass spectrometry and reversed-phase protein arrays, and a new approach for correlative metabolomics and proteomics is presented.

1.1. Sample Preparation

In principle, sample preparation for transmission electron microscopy (TEM) has three requirements. The samples must be sufficiently thin (<100 nm). The specimen must withstand the vacuum in the microscope and must be stabilized to withstand the electron beams' radiation. The most prominently used methods to achieve this are the cryoprotection by cryo-EM and heavy metal embedding (negative stain). Most of these are well established and have been used almost unchanged for a long time. However, with the advances in EM, there are now efforts to develop new methods of sample preparation to avoid some of the issues that the traditional approaches have. Today's methods that can be utilized for single particle analysis are now presented together with their advantages and disadvantages and their respective fields of application.

Negative Staining EM

Possibly the simplest way to prepare samples for TEM is the negative staining method. It uses 3 mm wide EM grids coated with two films. The grid is usually made out of copper, and sometimes of gold or nickel. The two films are a polymer film, such as Formvar or Parlodion, and a thin film of amorphous carbon (Figure 1.1b). In the first step, the sample is applied to the grid and incubated for a short time. During this process, the macromolecules are adsorbed on the carbon film and are thus concentrated for the subsequent microscopy examination. Afterwards, excess salt is removed with water in an optional washing step (not represented in the figure). Finally, a heavy-metal staining solution, such as uranyl acetate or methylamine tungstate, is applied to the grid. After each step, the excess solution is removed by a filter paper (Figure 1.1a). The stains heavy-metal salts are primarily deposited around the biological macromolecules, forming something similar to a mold. This mold is later imaged under the microscope and provides a high contrast in the images due to the strong scattering of the electrons at the heavy metal ions. The background mold appears darker than the macromolecules due to the weak electron scattering of the macromolecules. For this reason, this technique is called negative staining EM (Figure 1.1c). One of the main advantages of this method is the simplicity of quickly preparing samples and analyzing them at room temperature. It is also possible to prepare samples with a low concentration due to the carbon film's concentrating effect. On the other hand, the carbon background, together with the heavy-metal staining's grain size, makes it impossible to reach high resolutions. In the ideal case ∼15 Å can be achieved [Nogales 2015]. Therefore, negative staining is mainly used in a first step to evaluate the quality of a new sample. For example, its homogeneity and purity. Unfortunately, it is impossible to draw any further conclusions for a subsequent cryo-EM preparation, as the sample often behaves completely differently.

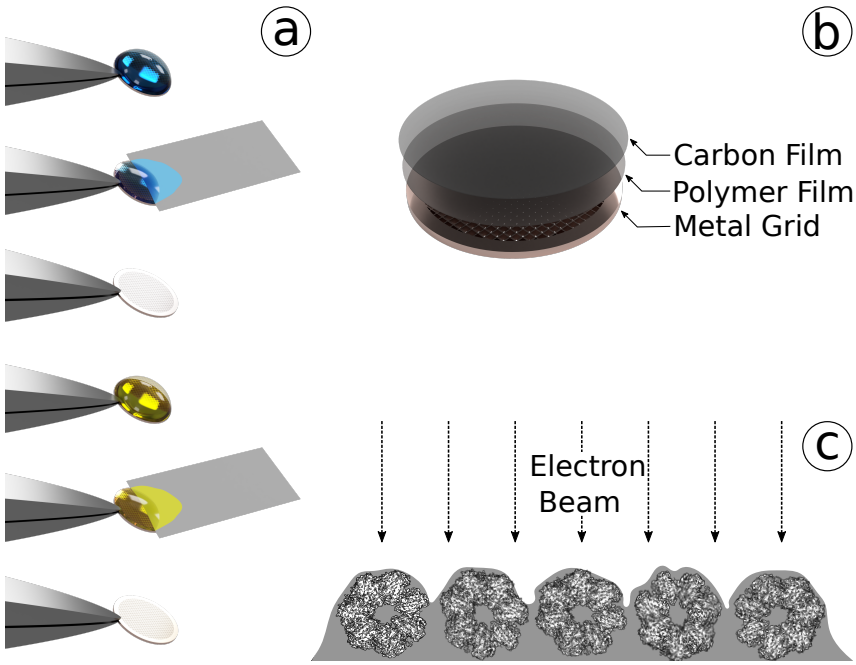

Figure 1.1: Negative Staining EM. **(a)** The procedure of sample on EM grid preparation chronologically from top to bottom. First, a sample is applied and incubated on the grid. The excess material is then removed through a filter paper, and a heavy-metal stain is applied for a few seconds. Finally, the excess staining material is removed, and the grid is ready for observation in the microscope. **(b)** Schematic structure of a sample grid. A metal support structure is covered by two thin films of a polymer and amorphous carbon. **(c)** Functional principle of negative staining EM. Heavy-metal salts accumulate around the adsorbed macromolecules. Due to the salts' strong electron scattering, the background in the pictures becomes dark, and the contours of the bright appearing macromolecules are clearly visible.

cryo-EM

Vitrification is the method of choice for high-resolution analysis of biological samples by EM. In the 1970s, it was shown that frozen samples can provide high-resolution data [Taylor & Glaeser 1974] and the first manual instruments for the vitrification of biological samples were established in the 1980s [Dubochet *et al.* 1988]. Since then, the sample preparation process has not changed much. A thin layer of the sample solution is quickly frozen by immersion in a cryogen, usually liquid ethane. The sample freezes so rapidly ($>10^4\,\mathrm{K\,s^{-1}}$) that no crystal structure is formed, and the ice remains in a glass-like state, which is where the name vitrification comes from [Tivol *et al.* 2008]. Today, commercially available grids are used as supports, consisting of a metal mesh, usually made of copper or gold, and a holey carbon film on top of it (Figure 1.2b). On these grids, about $\sim 3\,\mu\mathrm{L}$ of the sample are applied before the

excess material is removed with filter paper. The remaining thin sample layer that also covers the holes is then vitrified (Figure 1.2a). Nowadays, most scientists use automated plunge-freezing robots, such as the Thermo Fisher Scientific Vitrobot, the Leica EM GP, and the Gatan Cryoplunge, which can perform this preparation process under controlled conditions. Even though this sample preparation method has proven itself for a long time, it also has some disadvantages. The sample loss is enormous and 99.99 % ends up in the filter paper. The paper is also relatively rough, which is one reason for an uneven ice thickness distribution since the contact to the grid is not the same everywhere [Armstrong *et al.* 2019]. This filter paper is also suspected of releasing ions such as calcium into the sample, affecting certain macromolecules. Besides these points, since from the moment of blotting, the ratio between the surface and the bulk material is huge and several seconds can pass before the sample is vitrified. The macromolecules interact many times with the air-water interface, which can often lead to denaturation but also to sticking and arrangement of the protein to the air-water interface. This can result in damaged particles and preferred orientations. More on this topic follows in subsection 1.2. Despite all the drawbacks of this relatively simple sample preparation technique, it has enabled the investigation of many previously unfeasible macromolecules, thus laying the foundation for the success of cryo-EM.

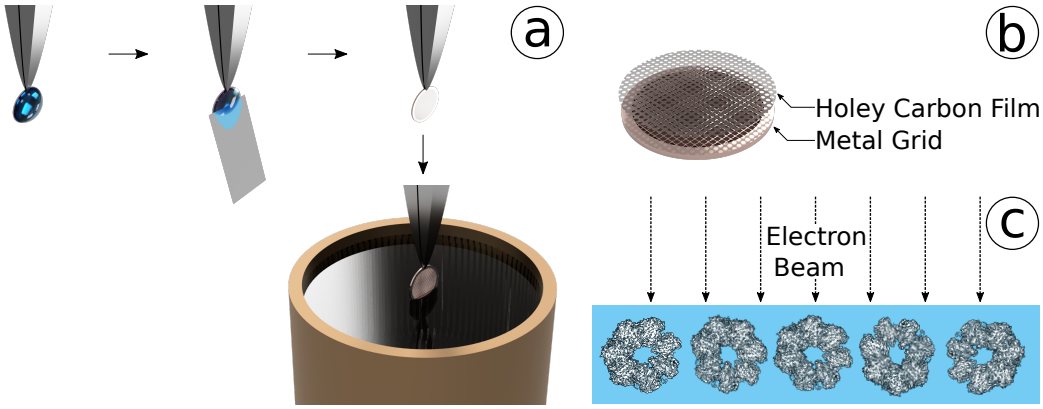

Figure 1.2: cryo-EM. **(a)** The procedure of sample on EM grid preparation chronologically from left to right. First, a sample is applied to the grid. Then the excess material is removed through filter paper. The remaining thin sample film is quickly frozen by immersion in a suitable cryogen. **(b)** Schematic structure of a sample grid. A thin holey carbon film covers a metal support structure. **(c)** Functional principle of cryo-EM. Macromolecules are distributed in the free-standing vitrified buffer layer in the carbon film holes and directly scatter the incident electrons.

When comparing cryo-EM with negative staining EM, some essential differences are worth mentioning. There is much less background noise because there is no carbon film in the path, and the electrons scatter from atoms of the sample itself

and not from the amorphous heavy-metal salts around it (Figure 1.2c). This is very good for high-resolution details but comes with the disadvantage that the atoms of a biological sample scatter electrons weakly because they are relatively lightweight. The resulting low contrast has to be compensated by averaging many particles. The absence of a carbon film is responsible for the fact that cryo-EM requires sample concentrations that are approximately one magnitude higher than in negative staining EM since there is no surface to which the molecules can adsorb. If too few molecules end up in the holes, thin films such as graphene or graphene oxide can be placed over them. However, this always happens at the expense of more background noise and complicates the sample preparation. A further difficulty in cryo-EM is the sample's movement during the acquisition, which, fortunately, can be computationally compensated relatively well thanks to the fast detectors that record videos instead of images. Nevertheless, the first few images in each video move too much for a movement correction, which is disappointing because the sample does not have any radiation damage in exactly these first frames. A new type of grid that has been recently presented may help solve this problem and possibly eliminate the drift problem once and for all [Naydenova *et al.* 2020]. Compared to negative staining EM, cryo-EM has a more complicated sample preparation, data acquisition, and data analysis, but is superior in the quality of the generated data.

Novel Approaches in Negative Staining EM

New developments in the field of negative staining EM have three main goals: (i) Saving time during screening by applying several samples on one grid. (ii) Analysing smaller sample quantities. (iii) Development of novel staining techniques. One approach is the use of inkjet technology, which allows smallest quantities of samples in the pico- to nanolitre range to be sprayed onto a grid [Jain *et al.* 2012]. This can also be done in a well-defined pattern on a single grid [Mulligan *et al.* 2015]; however, these systems must be primed first with volumes in the µL range. Another approach to applying small amounts of samples in a pattern on a grid is the use of microarray deposition machines [Castro-Hartmann *et al.* 2013]. However, these methods have the disadvantages that the negative staining must still be carried out using the classical procedure, which carries cross-contamination risk. Methods that allow automated staining using microfluidic chips [Mukhitov *et al.* 2016] or microdialysis fibers [Kemmerling *et al.* 2012] have also been developed but lack the ability to process small amounts of samples. However, all these newly developed methods have a niche existence. Many laboratories use negative staining EM only as quality control for new samples and therefore do not need fast high throughput screening as the classical method meets their requirements.

Novel Approaches in cryo-EM

In recent years, several developments have addressed some of the problems associated with classical sample preparation for cryo-EM. Among these problems are : (i) the large sample volume of ∼3 µL and the high sample loss of 99.99 %, (ii) the detrimental filter blotting step, (iii) the slow nature of the sample preparation process and the related problems with the air-water interface and fast reactions. Certainly, all new approaches have their advantages. However, they are always accompanied by either higher complexity of sample preparation or higher costs. To date, no method managed to become the new standard in cryo-EM, but they could be used for certain specific experiments.

Time-resolved cryo-EM, for example, addresses the problem of the speed of classical preparation to study reactions that can occur only fractions of a second before vitrification. This was first accomplished by spraying one reactant onto a grid on which another reactant was already present and then rapidly freezing it [Berriman & Unwin 1994]. Newer approaches use electrosprays to atomize the samples [White *et al.* 2003] or include microfluidic mixing devices to allow the reactants to react briefly and then quickly spray them onto a grid, using either humidified gas streams that flow past the sample nozzle and entrain micrometer-sized droplets [Lu *et al.* 2009, Lu *et al.* 2014, Chen *et al.* 2015], sophisticated micro-sprayers [Feng *et al.* 2017] or voltage-assisted spraying [Kontziampasis *et al.* 2019]. Often the greatest difficulty of these methods is to achieve a sufficient quantity of good ice. Another approach that tries to both reduce sample consumption and speed up the process use the well-established inkjet spotter technology to spray samples onto grids before vitrification [Jain *et al.* 2012, Dandey *et al.* 2018]. However, this requires special "self-blotting" grids that rely on grown nanowires on the copper surface at the grid's backside to obtain ice with the right thickness [Razinkov *et al.* 2016, Wei *et al.* 2018]. A relatively simple device that utilizes the same grids but uses a piezoelectric transducer for atomizing the sample promises similar results but is much cheaper to acquire [Rubinstein *et al.* 2019]. A kind of miniaturized version of these piezoelectric transducers and a relatively new way of spraying even the smallest amounts of samples onto a grid is the atomization of samples by surface acoustic waves (SAW) [Ashtiani *et al.* 2018]. Another device exists that applies small amounts of the sample via pin printing and does not require filter-blotting nor "self-blotting" grids. Here a pin passes a small amount of sample to the grid before freezing [Ravelli *et al.* 2020]. Like many other methods that apply tiny amounts of sample to the grids, this method also suffers from the fact that the sample is lost through the system's priming. Also, it is not fast enough to offer the possibility of fast time-resolved experiments. Another filter-blotting-free method allows almost shear-free sample thinning by using capillaries [Lee *et al.* 2012]. An approach not based on the development of new hardware is the use of thin surfactant layers to better control the sample layer's thickness and

reproducibility before freezing [Glaeser *et al.* 2016].

To summarize, it can be said that the main problems of classical preparation have been tackled with the above-mentioned methods, and various improvements have been achieved. Still, not all problems have been solved yet, and there are also new hurdles to overcome, such as successfully freezing several samples on a single grid. The final solution has yet to be found. However, it may also lead to the development of specific methods for certain types of experiments.

cryoWriter

Another approach, not discussed in the previous sections, has been developed by our group over the last few years. The *cryoWriter* is able to prepare grids for both negative staining EM as well as cryo-EM using only minute amounts of sample [Arnold *et al.* 2016, Arnold *et al.* 2017, Rima *et al.* 2018]. Its microfluidic design also enables other applications such as the integrated purification of samples [Schmidli *et al.* 2019] and the lysis of single cells and the subsequent processing of the lysates [Kemmerling *et al.* 2013]. The main functions are now described and discussed below.

Grid preparation

The preparation of specimens in the *cryoWriter* does not require special grids, so standardized commercial grids as shown in Figure 1.1 and Figure 1.2 can be used. The process of sample preparation for cryo-EM is shown in Figure 1.3a and for negative staining EM in Figure 1.3b.
For negative staining EM, 3 nL to 10 nL of sample are first aspirated with a capillary and then immersed into a reservoir with stain. This creates two interfaces: in the capillary with the system liquid and at the tip with the stain in the reservoir. The system liquid is normally degassed water, but the capillary can also be precharged with stain for stronger staining. In a diffusion-driven process, heavy metal ions will then migrate into the sample plug, while salt molecules will leave simultaneously. Macromolecules leave the plug at a much slower rate because they have much lower diffusion coefficients. After 2 min to 12 min, depending on the buffer conditions, the sample can be applied to a glow-discharged grid where it is slowly dried on a temperature-controlled stage to minimize the coffee ring effect. It is important to note that no stains with cross-linking properties such as uranyl acetate should be used in a diffusion-driven staining process, as the macromolecules will otherwise aggregate. Substances such as methylamine tungstate can be used instead.

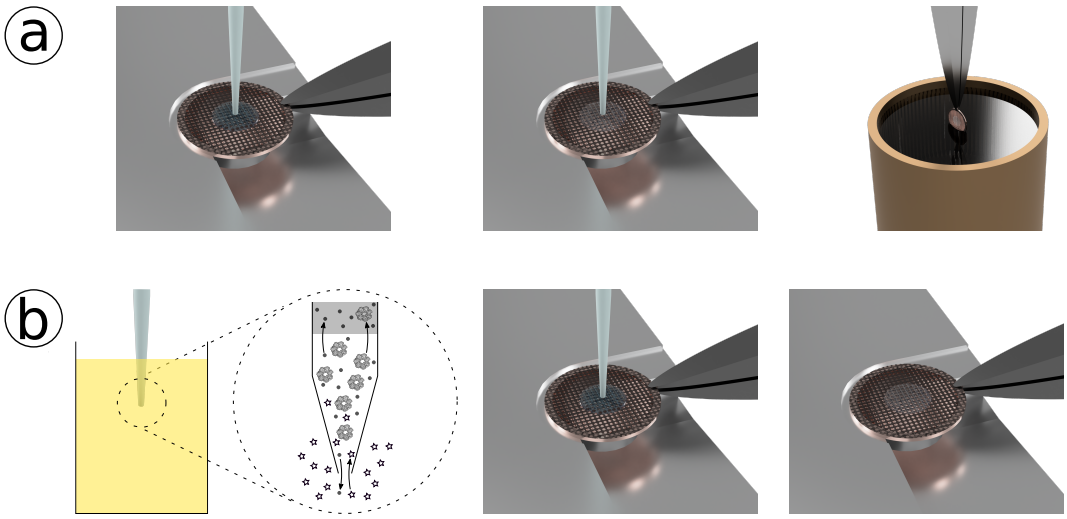

Figure 1.3: Grid Preparation using the *cryoWriter* setup. **(a)** cryo-EM. 3 nL to 20 nL of sample are deposited on a grid, then excess material is aspirated and the remaining thin layer is rapidly vitrified by immersion in a cryogen. **(b)** Negative Staining EM. After sample uptake, the capillary is immersed in a reservoir of stain and through a diffusion-driven process, the sample is desalted and simultaneously stained (Stain molecules are represented as stars, salt molecules as dots). After a few minutes, the sample is applied to a grid and then slowly dried.

For cryo-EM, 3 nL to 30 nL of sample are first aspirated with a capillary and then applied to a glow-discharged grid. This is preferably done by writing a pattern, such as a spiral, to maximize the wetted surface area. Subsequently, the capillary is brought as close as possible to the grid, and the excess sample is aspirated. The grid is then rapidly immersed in a cryogen, which vitrifies the sample's remaining thin layer.
Both grip preparation variants are fully automated using the openBEB framework [Ramakrishnan *et al.* 2014].

Sample purification

The structure determination by cryo-EM SPA starts with the production, isolation, and purification of the target structure from cells. An ideal sample should be as pure and homogeneous as possible, and the biological macromolecules should be intact and active. If a sample is not pure, it can be purified *in silico*, but this makes processing more difficult and requires large data sets, so optimizing the purification is usually the best solution. In principle, $\sim 10^4$ particles to $\sim 10^6$ particles are sufficient for a high-resolution three-dimensional reconstruction. However, as mentioned in

the sections on sample preparation, cryo-EM requires relatively high concentrations (in the micromolar range). Besides, 99.99 % of the sample is lost in the classic but still the most common method of sample preparation. This also means that sample purification usually starts with large volumes to obtain sufficient sample material after all centrifugation, filtration, and chromatography steps. This is especially true for macromolecules that cannot be expressed recombinantly and must be obtained from crude cell lysate. If the enormous sample waste during preparation is eliminated, large starting volumes could be avoided, and microfluidic systems can handle the required volumes. Since the *cryoWriter* is a microfluidic system capable of preparing specimens without wasting significant amounts of sample, a microfluidic purification module is a useful addition [Schmidli *et al.* 2019].

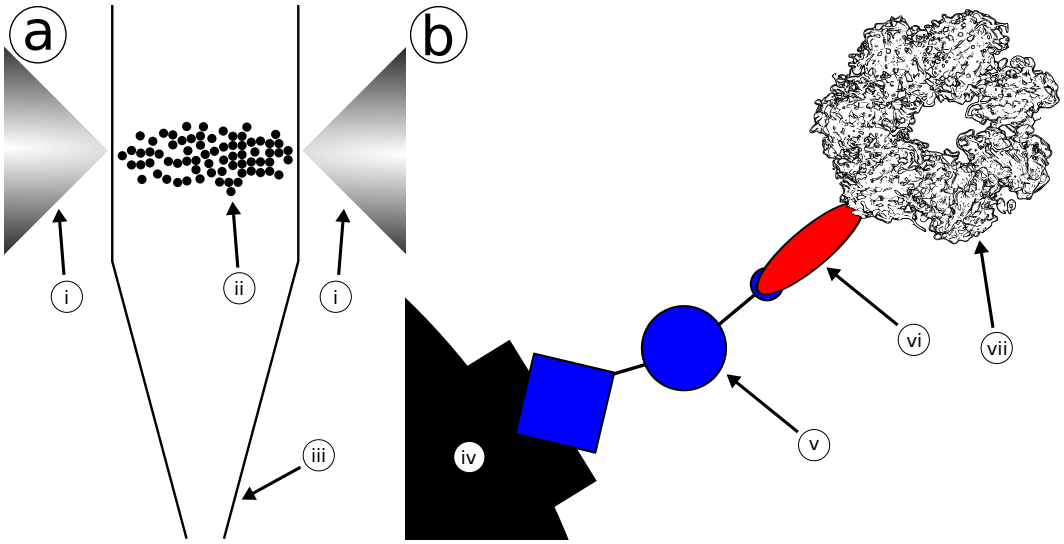

Figure 1.4: Sample purification using the magnetic trap module of the *cryoWriter*. **(a)** Functionalized magnetic nanoparticles are immobilized in a capillary using two electromagnets. **(i)** Iron tips of the electromagnets, **(ii)** Plug of magnetic nanoparticles, **(iii)** Glass capillary for sample uptake and deposition. **(b)** Schematic structure of the binding of the target macromolecule to the magnetic nanoparticles. **(iv)** Magnetic nanoparticle with a streptavidin coating, **(v)** Photocleavable NHS-Biotin crosslinker, **(vi)** Antibody or FAB, **(vii)** Target macromolecule.

The microfluidic protein isolation principles are simple . The same capillary used to manipulate the sample during grid preparation is placed between two electromagnets that create a high magnetic field gradient. This gradient can be used to immobilize magnetic nanoparticles and form a plug in the capillary (Figure 1.4a). These particles often consist of magnetite ($Fe^{2+}(Fe^{3+})_2O_4$) and if they fall below a critical size of about 30 nm, they exhibit superparamagnetic properties, which is desirable as they have no remanence [Bedanta & Kleemann 2008, Brullot *et al.* 2012]. If larger particles

with these properties are required, this can be achieved by coating them, e.g., with a polymer [Petri-Fink *et al.* 2008]. Such particles can be functionalized with different ligands. Often streptavidin, which enables the binding of biotinylated molecules, is used. In our case, antibodies and/or FAB fragments were attached to the magnetic particles using a crosslinker with an amine-reactive ester group and a biotin moiety at its other end. In between, an optional photo-cleavable nucleus was employed to facilitate the separation of the antibody/FAB fragment and magnetic particle by illumination of ultra-violet (UV) light (Figure 1.4b). Furthermore, a photo-cleavable NTA crosslinker, which allows binding His-tagged proteins, has already been tested successfully. Using such functionalized magnetic nanoparticles to form the plug in between the two electromagnets allows the immobilization of target macromolecules in the capillary while other materials can be washed away. After separating the target structures, they can then be applied to an EM grid using the grid preparation protocols mentioned before by breaking the crosslinker by UV exposure or switching off the electromagnets. If the crosslinker is not cleaved before grid preparation, the magnetic particles can serve as electron-dense labels in the microscope, e.g., as fiducials for tomography.

This miniaturized EM pipeline of sample purification and grid preparation is fast and cost-effective and was used to get a high-resolution 3D reconstruction of the endogenous 20S proteasome from only 900 nL of crude cell lysate [Schmidli *et al.* 2019]. In the future, it will give us the possibility to tackle structures that were so far unachievable due to problems during expression and/or purification.

1.2. Properties of Thin Films During Sample Preparation

As previously mentioned, samples for TEM must be sufficiently thin to be analyzed. This means that for cryo-EM at the time of vitrification, aqueous films with a thickness of <100 nm must be present on the grid. Ideally, the resulting ice layer should be only slightly thicker than the sample size to minimize inelastic electron scattering. This is remarkable because aqueous films of this dimension are inherently unstable and cause difficulties during sample preparation. They also have an extensive surface to volume ratio, leading to further problems with biological samples. The origins and implications of these unstable films and the large air-water interface issues are explained and discussed below. Various possible solutions for better sample preparation are also suggested.

Film Formation

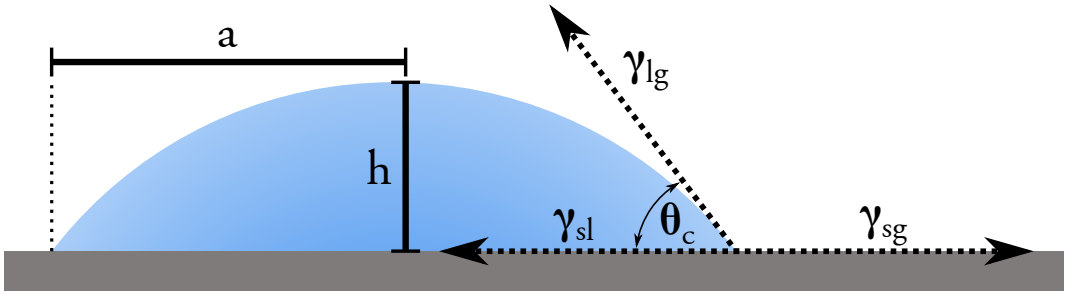

Figure 1.5: A drop of liquid deposited on a hydrophilic surface. Where **a** is the radius and **h** the height of the droplet. $\boldsymbol{\theta_c}$ is the angle which the liquid (l) and the gas (g) form on the solid surface (s) and the $\boldsymbol{\gamma}$ are the corresponding surface tensions.

If a drop of liquid is placed on a smooth, clean surface, it will form a contact angle with that surface (Figure 1.5) that follows the Young equation [Young 1805]:

$$cos\theta_c = \frac{\gamma_{sg} - \gamma_{sl}}{\gamma_{lg}}, \tag{1.1}$$

where θ_c is the contact angle, γ_{sg} the surface tension of the solid-gas interface, γ_{sl} the surface tension of the solid-liquid interface and γ_{lg} the surface tension of the liquid-gas interface. Below a certain size, called the capillary length λ_c, the influence of gravity on the shape of this deposited drop can be neglected.

$$\lambda_c = \sqrt{\frac{\gamma_{lg}}{\rho \cdot g}}, \tag{1.2}$$

where ρ is the liquid density and g the gravitational acceleration. The capillary length for water on earth is ~2.7 mm. Accordingly, for a 3 µL drop on a standard EM grid with a much smaller height, the shape can be assumed to be that of a truncated sphere. This allows to calculate the height of the drop in its center:

$$h = \frac{a}{sin\theta_c} \cdot (1 - cos\theta_c) \approx \frac{a \cdot \theta_c}{2}, \tag{1.3}$$

where a is the radius of the drop and the approximation suitable for small angles. The volume of the drop can then be derived as:

$$V = \frac{\pi \cdot h}{6} \cdot (3a^2 + h^2) \approx \frac{\pi}{4} a^3 \theta_c. \tag{1.4}$$

The approximation again applies to small angles and is obtained by inserting the approximation of Equation 1.3. Putting all this into the context of cryo-EM grid

preparation, the following can be deduced: If a 3 µL large drop is deposited on a 3 mm grid, a drop with a larger contact angle than given by Equation 1.1 and a higher height than given by Equation 1.3 will form first, because the surface of the grid is limiting. If a filter paper is then used to blot on the side of the grid, liquid is sucked off until the contact angle of the drop and not the available surface of the grid is the limiting factor. Although this contact angle is relatively small due to the commonly used grid surface activation by a plasma treatment, [Glaeser *et al.* 2016] have measured with a microbalance that there is at least 20 nL of liquid left after blotting, which, considering Equation 1.3 and Equation 1.4, corresponds to a contact angle of ∼0.4° and a drop height of ∼6 µm, which is too thick to be examined in a TEM. For this reason the blotting is usually not done laterally, but rather the filter paper is pressed flat on the grid surface. This causes on the one hand an absorption of the water at several points simultaneously and on the other hand a mechanical forming of the drop into a thinner layer than described by the formulas above. After blotting, the aim is to quickly vitrify this thin remaining film. However, it turns out that the resulting ice rarely or never has a homogeneous thickness on the whole grid. The reason for this is the rough surface of the filter paper coupled with the fact that very thin aqueous films are inherently unstable. In order to explain this better, the following section will take a closer look at the forces that are important for the stability of thin films.

Thin-film stability

When a volume of liquid contacts a solid surface, the solid's surface wetting depends on the properties of the interface between the liquid and the solid and the respective interfaces to the gas-phase. For the spreading of the liquid on the surface, two energies must be considered: Adhesion and cohesion. We can consider the following master equation for the change in the Gibbs free energy dG:

$$dG = -SdT + VdP + \sum_i \mu_i dn_i + \sum_j \gamma_j dA_j \,, \tag{1.5}$$

with S being the entropy, V the volume, and μ the chemical potential. For constant temperature $dT = 0$, constant pressure $dP = 0$, and the absence of evaporation or chemical reactions ($dn_i = 0$), we see that the change of the dG changes with the area dA. If a volume of liquid gets in contact with the interface, a contacted area dA between the liquid in the interface is established. According to Figure 1.5 we get $dA = dA_{sl} = -dA_{sg} = -dA_{lg}$, and we obtain for dG for adhesion and cohesion

$$dG = \underbrace{dA \cdot (\gamma_{sl} - \gamma_{lg} - \gamma_{sg})}_{\text{Adhesion}} + \underbrace{dA \cdot 2\gamma_{lg}}_{\text{Cohesion}} . \tag{1.6}$$

We can define the the spreading coefficient ($S = -dG/dA$) of the droplet to the surface:

$$S = \gamma_{sg} - \gamma_{sl} - \gamma_{lg} , \tag{1.7}$$

which is the difference between the adhesion-work and the cohesion-work.

Inserting of Equation 1.7 into Equation 1.1 the result is:

$$S = \gamma_{lg} \cdot (cos\theta_c - 1) . \tag{1.8}$$

Looking at this formula, it is obvious that a calculation of the contact angle is only possible if the spreading parameter is negative. This leads to the distinction between two regimes. Total wetting if $S \geqslant 0$ and partial wetting if $S < 0$. In the total wetting regime $\theta_c = 0$ and thus the liquid spreads completely, in the partial wetting regime a drop is formed which has a contact angle like in Figure 1.5 [Widom 2004].

The spreading coefficient can be divided into its polar (P) and apolar Lifshitz van der Waals (LW) components [Sharma 1993]. This results in:

$$S^{LW} = \gamma_{sg}^{LW} - \gamma_{sl}^{LW} - \gamma_{lg}^{LW} , \tag{1.9}$$

$$S^{P} = \gamma_{sg}^{P} - \gamma_{sl}^{P} - \gamma_{lg}^{P} , \tag{1.10}$$

Using this notation, it can be stated that S^{LW} is almost always positive for aqueous films since $\gamma_{sg}^{LW} > \gamma_{lg}^{LW}$, which signifies a net van der Waals repulsion. On the other hand, S^P is always negative because γ_{lg}^{P} is very large due to the high polar cohesion energy of water molecules, which signifies polar hydrophobic attraction [Padmakar *et al.* 1999]. Therefore, it can be concluded that the van der Waals repulsion has a stabilizing effect on an aqueous film, whereas the polar hydrophobic attraction has a destabilizing effect [Sharma 1993]. The height dependent excess free energy per unit area ΔG can further be represented using S^{LW} and S^P as follows [Sharma 1998]:

$$\Delta G = \frac{S^{LW} \cdot d^2}{h^2} + S^P \cdot e^{\frac{d-h}{l}} , \tag{1.11}$$

where d is a cutoff distance after which Born repulsions dominate, l is a correlation length for the hydrophobic interaction and h is the thickness of the water film. The disjoining pressure ($\Pi = -\partial\Delta G/\partial h$) derived from ΔG plays an important role for thin films, because it can indicate whether dewetting/film rupture is promoted or the film is stabilized [Padmakar *et al.* 1999, Glaeser *et al.* 2016]. If it increases with the film thickness, the film is unstable, ergo $\Phi_h = \partial\Pi/\partial h > 0$.

$$\Phi_h = -\frac{6 \cdot S^{LW} \cdot d^2}{h^4} - \frac{S^P}{l^2} \cdot e^{\frac{d-h}{l}}, \tag{1.12}$$

If Φ_h is plotted qualitatively with $S^{LW} > 0$ and $S^P < 0$, a graph as in Figure 1.6 is obtained [Sharma 1998].

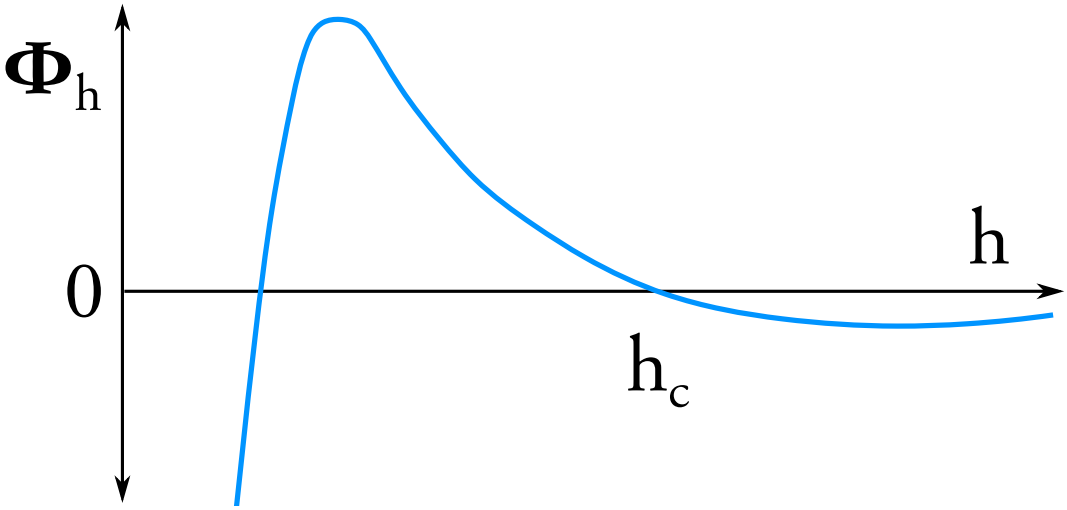

Figure 1.6: Φ_h plotted qualitatively with $S^{LW} > 0$ and $S^P < 0$. Where $\boldsymbol{h_c}$ is the critical film thickness at which the film becomes unstable due to the positive gradient of the disjoining pressure.

Some interesting conclusions can be drawn from this graph. When the film reaches a certain thickness, the long range van der Waals repulsion dominates and the film is perfectly wetting and stable because $\Phi_h < 0$. If the film becomes thinner e.g. by evaporation, as it is the case in the EM grid preparation, a critical film thickness h_c is reached from which the film is unstable. If the film is further thinned, the instability becomes greater and rises very rapidly. This can be seen from the positive peak for heights smaller h_c. At this point holes begin to form in the film. This happens at nucleation points, for instance where the film has a local height minimum. The corresponding rupture height is called h_r. Resulting is a patchwork of drops, which again have a height of more than h_c, with dry regions in between. Interestingly, the

driving force behind the rupture and instability of these thin films is the hydrophobic attraction [Sharma 1998, Padmakar *et al.* 1999]. This is also true for the hypothetical case when the thickness falls below the critical thickness without evaporation [Glaeser *et al.* 2016]. An illustration of a film rupture can be seen in Figure 1.7.

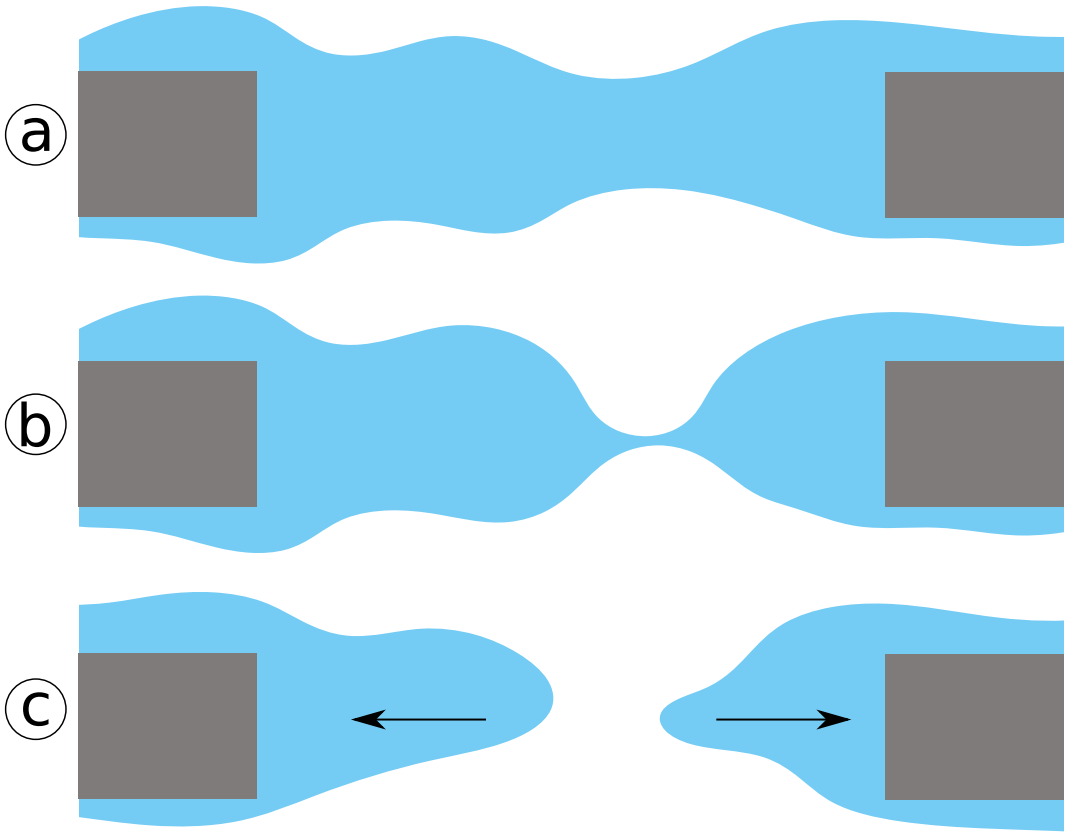

Figure 1.7: A thin film rupture. **(a)** A thin aqueous film spans a hole in a holey carbon layer of an EM grid. Variations in film thickness are schematically exaggerated. **(b)** If the film thickness falls below a critical level h_c, it becomes unstable. As soon as the film thins out further or is locally thinned out by surface fluctuations, the rupture height h_r can be reached and the film breaks. **(c)** In the subsequent dewetting process holes are formed in the previously continuous film which contracts and regains a greater height.

Another exciting finding of [Padmakar *et al.* 1999] is that the thinning rate, e.g. by evaporation, plays a critical role in film rupture. If the rate increases, the average h_r becomes smaller. So films can get thinner before they break. At the same time, the time of rupture will be shorter, and the instability stronger. This means for grid preparation that if a certain amount of evaporation is required, it should happen directly before the grid vitrification and should be as strong and fast as possible. Nevertheless, not too much water should evaporate, as this will change

the buffer conditions, which could affect the macromolecules or lead to more noise in the recorded images. In this context, evaporation is only considered as the rate of film thickness reduction. But evaporation itself also has an influence on the stability. As mentioned above, we have assumed, besides constant temperature and pressure ($dT = 0$, $dP = 0$), that no evaporation of liquid takes place ($dn = 0$). However, this is not the case with all preparation methods known to us today [Cyrklaff *et al.* 1990]. Therefore, the term $\mu_{H_2O} dn_{H_2O}$ becomes negative. Not in equilibrium, which qualitatively means that spreading and thin film formation is promoted. Therefore, the *cryoWriter* system can control the evaporation of the liquid and use it to promote thin films [Arnold *et al.* 2017].

The above theory was established for continuous solid supports. However, it should also apply to holey carbon supports as found on EM grids. If the air is considered as a hydrophobic surface, the wettability would be reduced (decreased S^{LW}), and the hydrophobicity would be increased (more negative S^P). S^{LW} and S^P would actually always be negative, which means that in one hole alone, no stable layer thickness can be achieved, which of course, makes sense. Therefore, the film becomes unstable at the latest from the critical thickness of the water film on continuous carbon. Most likely even before that, since the contact angle of a holey carbon layer should be higher than on a continuous one, which, considering Equation 1.8, leads to a reduced wettability and thus to a corresponding reduction of S^{LW} and S^P and therefore to a higher height h_c from Equation 1.12. Furthermore, the probability of a variation in film thickness is greater, since there are two gas interfaces, which increases the probability of a nucleation point for film rupture.

Problems

The consequence of such inherent instabilities of water films on the grid preparation is that it is challenging to produce homogeneous thin ice layers of the desired thickness. Grids tend to have ice which is either too thick or they dry out. Also, a systematic optimization of the ice thickness, which is only slightly larger than the sample itself, is only possible to a limited extent. Finally, it almost always leads to a trial and error process for finding suitable conditions and preparing a lot of grids before the final data acquisition. Such a procedure is not only time-consuming but, in the case of cryo-EM, also costly and requires access to suitable screening microscopes.

Another problem with thin aqueous films for sample preparation is the air-water interface. When films become thinner, the ratio between the surface area and the bulk volume becomes extremely large. The distance between the sample and the air-water interface becomes smaller and smaller. As a result, biological macromolecules can collide with the air-water interface > 1000 times per second as can be easily estimated with the following formula [Taylor & Glaeser 2008, Glaeser 2018]:

$$t = \frac{2q}{\langle x^2 \rangle \cdot D}\,, \tag{1.13}$$

Where q is the number of dimensions, $\langle x^2 \rangle$ is the mean-squared distance, D the diffusion coefficient and t the time to travel $\langle x^2 \rangle$. For a MDa sized particle with D =10 µm^2 s^{-1} this would be less than one second for a distance of 1 µm and since $t\,\alpha\,\frac{1}{\langle x^2 \rangle}$ already 100 times less at 100 nm [Glaeser 2018]. This is a problem that cannot be solved completely by a very fast grid preparation, although it seems that fast preparation is advantageous for some proteins [Noble *et al.* 2018b]. Every time a collision happens, there is the possibility that macromolecules are adsorbed at the air-water interface. For example, through hydrophobic sites that interact with the air, which is nothing more than a hydrophobic surface. This can lead to preferred orientations, conformational changes or denaturation of the macromolecules. Preferred orientations can make it difficult or even impossible to obtain a high-resolution 3D reconstruction, but this problem can be partly counteracted by taking tilted images. Conformational changes and denaturation on the other hand often make a 3D reconstruction completely unfeasible. In some cases it may be possible to purify *in silico*. However if most of the macromolecules are showing changes or damage, this is not practical. The reason for the preferred orientations is that macromolecules have sites that interact preferentially with the hydrophobic air surface. But if a protein binds to the surface, it cannot just get stuck, it also changes the energy landscape of protein unfolding completely. At the interface the energy landscape is expected to trend monotonically downhill, triggering a rapid unfolding of the protein, which leads to the exposure of previously protected residues inside the protein to the air while hydrophilic residues remain on the aqueous side [Glaeser 2018]. It has been shown that such unfolding can take only a few nanoseconds [Raffaini & Ganazzoli 2010] and that the complete air-water interface can be covered within only one second at a protein concentration of 1 mg mL^{-1} [Yoshimura *et al.* 1994]. This already happens before the thinning, but then this effect is further increased.
In summary, sample preparation for cryo-EM is a relatively complex task, which fortunately could be carried out for a long time using a relatively simple preparation technique that produces surprisingly good results. However, the problems associated with the stability of thin films and the fact that these thin films are a very hostile environment for biological macromolecules is becoming more and more of a problem today. As samples that are increasingly difficult to prepare become the subject of investigation, and the current classical methods often reaches their limits. In the following section, a number of possible solutions are presented to improve sample preparation and make it more efficient.

Solution Strategies

The idea that biological macromolecules like proteins are frozen in time by vitrification and can be studied in their native configuration whilst being randomly distributed in the resulting amorphous ice layers is unfortunately only conditionally true. This becomes obvious when a sample appears perfect before grid preparation. And then the grid preparation itself proves to be impossible or at least very difficult. An illustration of the complications that can occur during the preparation is shown in Figure 1.8a. Proteins can be adsorbed at the air-water interface and take preferred orientations. The particles can also be at different heights if the ice is thicker than the sample itself, leading to difficulties during processing, as the particles have different individual defocus values. Also, the proteins' conformation may change, or the proteins may partially or completely denature. Other proteins could start interacting with these denatured proteins at the surface as indicated by a partially unfolded protein and an adherent protein on the right side of the figure. These problems can be addressed in several ways. (1) Since surface activity often correlates with stability in solution [Razumovsky & Damodaran 1999], one option is to stabilize the macromolecules before preparation, for example, by optimizing the buffer composition, adding stabilizing substances, or by intramolecular crosslinking [Glaeser 2018]. However, this cannot prevent preferred orientations, and denaturation is also not excluded. Besides, not all stabilizing substances are compatible with cryo-EM, as they may cause problems during image acquisition, and intramolecular crosslinking can lead to artifacts in conformations or make certain conformations disappear. (2) As mentioned before, there are also attempts to avoid issues by freezing the samples faster than the problems that can arise. However, current methods are not yet fast enough to avoid all complications completely, as was shown in a large comparison recently [Noble *et al.* 2018a]. Nevertheless, it already has a noticeable positive effect on the difficulties attributed to the air-water interface [Noble *et al.* 2018b]. Another advantage of speeding up the thinning process could be stabilizing thinner films, as discussed earlier. (3) The preferred orientations, conformational changes, and denaturation of proteins, and low film stability could be addressed simultaneously by implementing an electron transparent protective layer at the air-water interface. Interestingly, the layer of denatured proteins that forms extremely quickly at the air-water interface can serve exactly this purpose [Glaeser & Han 2017] and has probably done so frequently in the past, albeit unintentionally. The disadvantage is that this is probably not universally applicable for all proteins. The second layer of proteins that attach themselves to the denatured protein network at the air-water interface can also take on preferred orientations or denature, although probably less because the surface is less hydrophobic. Another improved controllable option is using surfactant monolayers to cover the air-water interface, as illustrated in Figure 1.8b. If these monolayers' surface pressure is high enough, biological macromolecules would no longer come into contact with the air-water interface.

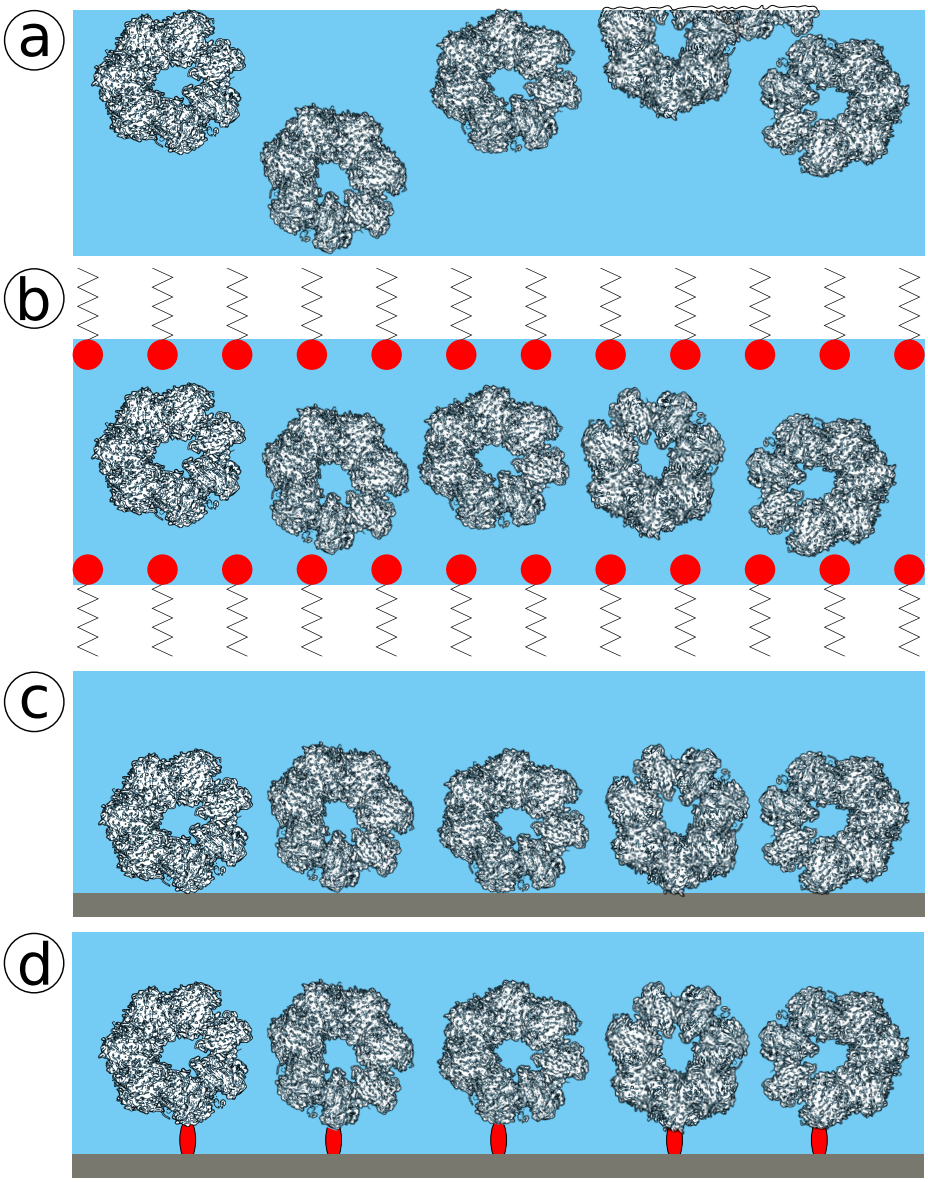

Figure 1.8: Proteins in a vitrified ice layer. **(a)** The classical cryo-EM grid preparation method results in ice layers with two large air-water interfaces on which particles can adsorb. Thereby, they can adopt preferred orientations, change their conformation or denature. Denatured proteins quickly form a surface layer on which proteins from the solution can be adsorbed. This is illustrated in the right part of the picture. **(b)** A layer of surfactants can be used to shield the particles from the surface and stabilize the ice layer. **(c)** Suitable electron transparent layers can be used to adsorb particles to keep them away from the air-water interface and to concentrate them at the same time. **(d)** Support layers as in (c) can be additionally functionalized to bind particles specifically. This can increase the efficiency and allow sample purification directly on the grid.

Still, they could only interact with the surfactants' polar moieties, which is supposed to be relatively weak [MacRitchie & Alexander 1963, Glaeser 2018]. This is not a completely new idea and was suggested some time ago for phospholipids [Frederik *et al.* 1989] and has recently been revisited and also discussed in the context of the stability of thin films [Glaeser 2016]. In addition to the property that surfactants can shield the air-water interface for biological macromolecules, they can also reduce the surface tension of water γ_{lg}. This has two major advantages. First, regarding the Equation 1.1, the contact angle will be smaller (for θ_c <90°) and the spreading coefficient S from Equation 1.8 will approach closer to 0, which corresponds to the total wetting regime. This is already good because the stable height h of Equation 1.3 will decrease. Also S^{LW} will become larger and S^P less negative which results in a smaller critical height h_c from Equation 1.12 and consequently a smaller rupture height h_r. Second, the Marangoni Effect, which describes a flow resulting from surface tension gradients (as known from the 'tears of wine'), can reduce the film's height fluctuations, thus resulting in fewer nucleation points for film dewetting. This occurs because if there is a surface fluctuation in the film, the surface area will increase. This results in a lower concentration of surfactant locally, causing a flux that levels out the fluctuation. We recently developed a system that allows surfactants to be added to the sample via the gas phase during grid preparation. We expect to exploit the positive properties of surfactants by using this well-controlled system and further to incorporate it into our standard sample preparation. More information follows in section 3. (4) Another approach to solving problems with the air-water interface is to prevent the macromolecules from moving freely in solution. Instead, the particles can be bound on a structure-friendly support film [Glaeser 2018]. This has several advantages. The macromolecules are guaranteed never to contact the air as long as the ice is thick enough. The particle density in the final ice layer can increase by concentrating the particles on the film, and they are in one focal plane during image acquisition. Structure-friendly support films are available in two different variations. On the one hand, films that can bind macromolecules non-specifically and are sufficiently electron transparent (Figure 1.8c) and, on the other hand, films that are additionally equipped with special linker molecules that can specifically bind and immobilize macromolecules (Figure 1.8d). Non-specific binding support films usually consist of evaporated carbon, graphene [Russo & Passmore 2014], or graphene oxide [Pantelic *et al.* 2010]. Graphene and graphene oxide generates much less noise in the images than evaporated carbon does. However, they are more complicated and expensive to manufacture and more fragile to use. Such films can be made hydrophilic by plasma treatment. Support films with special linker molecules are referred to as affinity grids, and the composition of these linkers and the type of binding to the target molecules can be diverse [Park *et al.* 2020]. For example, streptavidin monolayers are used that can bind proteins with biotinylated Lysine residues on the surface. This not only immobilizes the particles but can also eliminate a preferred orientation [Han *et al.* 2012]. Streptavidin monolayers can also

be used for biotinylated liposomes in combination with membrane proteins [Wang & Sigworth 2010] or biotinylated DNA, which in turn can bind to DNA binding proteins [Crucifix *et al.* 2004]. Lipid monolayers modified with Ni-NTA can be used to bind proteins with a his-tag. Although this has the disadvantage of producing preferred orientations, it opens up the possibility of protein purification directly on the grid [Kelly *et al.* 2008a], for example, by fishing a target protein from cell lysate [Benjamin *et al.* 2016]. Another possibility to bind proteins selectively on grids is the usage of specific antibodies. These can be immobilized either directly on the carbon [Yu *et al.* 2016] or via a protein A [Kelly *et al.* 2010]. The use of antibodies also enables protein purification directly on the grid. However, if monoclonal antibodies are used, there is a risk of preferred orientations [Glaeser 2018].

All of the above-mentioned solutions have their advantages over the classical sample preparation, where problems with the air-water interface and dewetting are largely ignored. However, until today nothing has been able to establish itself as a new standard procedure. This may be due to concerns that the resolution could be compromised, due to more complicated and expensive preparation procedures or simply due to the lack of suitable equipment. The future will show whether a method will really become generally accepted or whether it has to be looked at on a case-by-case basis. For the time being, cryo-EM grids are still mostly prepared classically first, hoping that the sample will behave well.

1.3. Single and Few Cell Analysis

If biological processes are investigated by bulk analysis of cells, it is assumed that the cells are homogeneous, which cannot be confirmed or falsified by the bulk analysis itself [Slavov 2021]. However, it has already been shown many times that this assumption is usually not true and therefore a bulk analysis can be valuable, but it may also lead to the loss of important information [Altschuler & Wu 2010]. In order to fully understand a cellular system, it is therefore essential to pay attention to the individual cells themselves and to understand their differences in the proteome, metabolome and transcriptome and their effects on the phenotype. Thus the analysis of a few or even of single cells is very important [Wang & Bodovitz 2010].

The *cryoWriter* setup described above for the preparation of negative staining and cryo-EM grids also provides the possibility to observe single cells over an extended period of time and to pick and lyse them. The collected single-cell lysate can then be prepared for TEM examination [Kemmerling *et al.* 2013]. This opens up the possibility of 'Differential Visual Proteomics', where the single molecule resolution of TEM can be exploited to resolve differences in the proteome between individual cells [Syntychaki *et al.* 2019]. Hence, the setup can be used to study the phenotype and the corresponding proteome of single cells. In order to extend its functionality, attempts

were made to combine the setup with new methods that can provide additional information. One method that would be very interesting is mass spectrometry (MS). Its ability to analyze minimal amounts of samples without labeling and to detect various biomolecules such as lipids, peptides, proteins and metabolites in a sensitive and specific way has made MS a very popular method for single cell analysis [Oomen *et al.* 2018]. Today, different variants have been established, which may differ in the way of sample preparation, separation, ionization and detection [Gowda & Djukovic 2014]. Some of them are briefly introduced and explained in the following section. Another interesting technique that could provide additional information is reverse-phase protein arrays (RPPA). In this technique, target proteins are first immobilized on a support and then labeled using antibodies. Thus, proteins can be detected and to a certain extent quantified. This is also discussed in more detail below. Finally the implementation and combination of MS and RPPA with the single-cell lysis module of the setup is discussed.

Single Cell Analysis by Mass Spectrometry

Mass spectrometry has become one of the leading methods for the analysis of single cells. Especially for the study of the proteome as well as the metabolome, it provides valuable insights. In combination with our setup, the possibility to study metabolites is of particular interest, as this is not possible with TEM. Different methods are briefly introduced and explained, which have been developed to investigate single cells or single cell components using mass spectrometry.
Variations of MS used for single-cell analysis differ in the way of sample preparation, separation, ionization, and detection [Gowda & Djukovic 2014]. However, due to the great importance of ionization for MS studies, two reasonable categories can be formed for biological samples. The ambient and non-ambient ionization techniques [Yang *et al.* 2017]. Two prominent examples of the non-ambient ionization category are matrix-assisted laser desorption/ionization (MALDI) and secondary ion mass spectrometry (SIMS). In MALDI, analytes are embedded in organic matrices. The sample is then irradiated with a pulsed laser, triggering desorption/ionization reactions [Lai & Wang 2017]. It is a relatively gentle ionization method with advantages including high tolerance to contaminations, high sensitivity, minimal sample handling, and low sample consumption. One disadvantage is signal suppression by low-mass ions from the matrix, which complicates the measurement of small metabolites [Lai & Wang 2017, Evers *et al.* 2019]. Another circumstance is that experimentation must be carried out in a vacuum, which prevents the examination of living cells [Yang *et al.* 2017]. Since the laser can be accurately focused, MALDI can be used to analyze single cells and subunits of single cells. SIMS shares some similar characteristics to MALDI. The main difference is that the samples are not embedded in a matrix, and a beam of primary ions is used to sputter secondary ions from the sample. Since ion

beams can be easily focused, the lateral resolution is even better than in MALDI. Also, it is very surface sensitive, which can be used to create nanometer-depth profiles [Oomen *et al.* 2018]. Ambient ionization techniques can be further divided into three sub-categories that consider sample preparation, separation, and ionization. That is, (1) methods that aspirate contents from single cells, (2) methods that extract analytes from single cells, and (3) methods utilizing desorption/ionization reactions [Yang *et al.* 2017]. The first type of content aspiration uses capillary tips capable of penetrating cells to collect the sample and then ionize it for MS analysis by nanoelectrospray ionization (nanoESI), a miniaturized and more efficient variant of ESI [Wickremsinhe *et al.* 2006]. There are several approaches to this, which differ mainly in the capillary design and the application of the high voltage. Live single-cell video-MS uses metal-coated capillaries, which can be introduced into cells under the observation of a microscope and subsequently be used for sample ionization [Mizuno *et al.* 2008]. Capillary microsampling ESI-MS uses uncoated capillaries to aspirate samples from cells. The high voltage is then applied via a platinum wire inside the capillary [Zhang *et al.* 2014]. Capillary Pressure Probe ESI-MS uses quartz capillaries, and the voltage can be applied through a wire both externally and internally. The advantage of this method is the possibility to control the aspirated volume by using a piezo-manipulator, which is important for quantification [Nakashima *et al.* 2016]. The second sub-category is analyte extraction. It uses either liquid for extraction and separation of analytes, called liquid-liquid microextraction (LLME), or functionalized metal needles, called solid-liquid microextraction (SLME). LLME includes nanomanipulation-coupled nanospray MS, where the solvent is first injected into the cell by a metal-coated capillary and, after some time, removed again and analyzed by MS [Phelps *et al.* 2014]. LLME also includes single-probe MS, which works similarly in principle. However, the cell is pierced with a separate dual-bore quartz needle connected to a capillary for solvent supply on one side and to an ESI emitter on the other side. This allows analytes to be extracted with a continuous flow of solvent and then analyzed immediately by MS [Pan *et al.* 2014]. SLME comprises probe electrospray ionization MS (PESI-MS) where a solid needle (e.g., tungsten) is inserted directly into the cells to adsorb analytes, which are then ionized and sprayed into the MS by applying a high voltage [Gong *et al.* 2014]. PESI-MS can also be used without an extraction step using an inkjet spotter to apply small drops containing a single cell directly to the high voltage needle [Chen *et al.* 2016]. Another SLME technique is direct sampling probe mass spectrometry (DSP-MS). In this technique, analytes are first concentrated on a tip that can be introduced into the cells and then electrosprayed into the MS with the assistance of solvent addition [Yu *et al.* 2014]. Similar in function is surface-coated probe MS (SCP-MS), where special coatings are used to make the extraction more selective and efficient [Deng *et al.* 2015]. The third sub-category uses desorption/ionization reactions like MALDI and SIMS but does not require a vacuum environment. For example, desorption electrospray ionization MS (DESI-MS) uses charged solvent droplets that are shot at the sample to ablate

and ionize the sample [Ferreira *et al.* 2012]. Easy ambient sonic-spray ionization MS (EASI-MS) works like DESI-MS, but instead of high voltage, compressed nitrogen is used to generate the droplet beam [Liu *et al.* 2014]. Laser ablation electrospray ionization MS (LAESI-MS) [Shrestha & Vertes 2009] and laser desorption/ionization droplet delivery MS (LDIDD-MS) [Lee *et al.* 2016] use lasers to first ablate the sample in combination with electrospray for ionization.
The presented methods all have their advantages and disadvantages regarding sensitivity, selectivity, and resolution. Thus, depending on the biological problem, the right technique has to be chosen. However, all methods have in common, especially the ambient ionization techniques, that the detection sensitivity is a limiting factor due to the small sample quantities and the high complexity of cells [Yang *et al.* 2017]. Also, the throughput is not yet high enough for many biological or medical studies for some methods.

Reverse-Phase Protein Arrays (RPPA)

A reverse-phase protein array (RPPA) is a miniaturized dot blot. Proteins are first immobilized on a carrier, and a specific primary antibody can then bind to these proteins. If the primary antibody is not labeled, a labeled secondary antibody can be used, which binds to the primary antibody. Thus, the labeled proteins become detectable. If data is collected, e.g., if a fluorescent label is used with a fluorescence microscope or fluorescence scanner, proteins can be detected and quantified. The advantages of RPPA include the small amount of sample required, high sensitivity, high throughput, and the ability to quantify proteins to a certain degree. A disadvantage is that a specific antibody is required to detect a protein. However, compared to the forward phase protein array (FPPA), where an antibody is immobilized instead of the protein, it is only one specific antibody and not two. Another difference to FPPA is that, in principle, RPPA is designed for the detection of a single protein in several samples simultaneously and FPPA for the detection of several proteins from a single sample [Boellner & Becker 2015]. However, by using different specific primary antibodies, RPPA can also detect several proteins from multiple samples.

Combination of the *cryoWriter* with Mass Spectrometry and RPPA

The single-cell lysis module of the *cryoWriter* can lyse adherent cells by electroporation and further process the obtained cell lysates. To accomplish this, cells grown on electrically conductive ITO-coated glass slides are first placed in a cell incubator of a fluorescence microscope from where they can be observed and selected. A target cell is subsequently first lysed and collected using a platinum-coated glass capillary. The

cell lysis works via electroporation. Therefore, the coated glass capillary is placed just above the cell, and an alternating voltage is applied between the capillary tip and the grounded ITO slide. Due to the small distance, a relatively large electric field is generated, leading to defects in the cell membranes. Eventually, shear forces acting during aspiration into the capillary cause the cell to lyse completely (Figure 1.9a). The entire cell lysate is then contained in the capillary and can be further processed, for example, for examination by TEM [Kemmerling *et al.* 2013]. For the combination with mass spectrometry and RPPA, other preparation methods were investigated, which allow the transport of cell lysates and their analysis in the different devices.

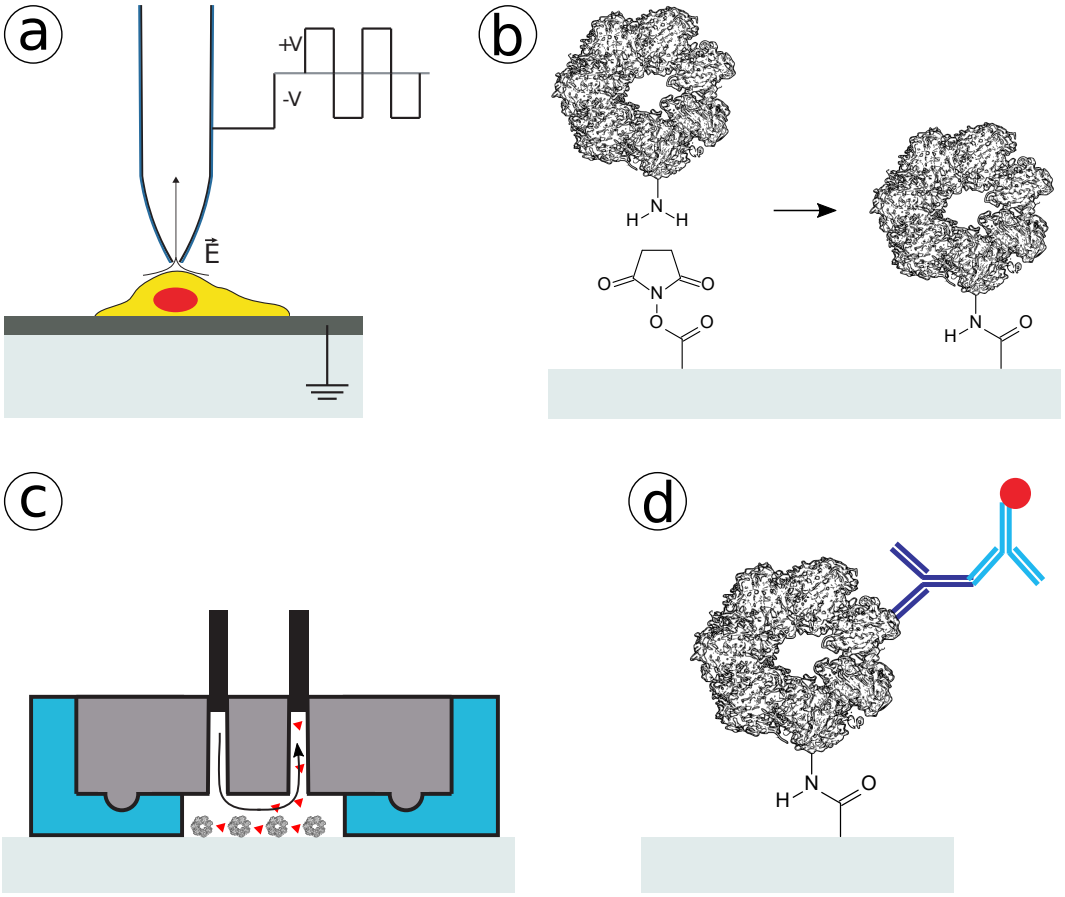

Figure 1.9: Combination of the single cell lysis module with mass spectrometry and RPPA. **(a)** Individual cells are lysed by electroporation and aspirated into the capillary. **(b)** The cell lysate is spotted onto a glass slide functionalized with NHS ester groups. Primary amines of biomolecules such as proteins react with the NHS esters and form amide bonds. This immobilizes them on the glass slide. **(c)** Using a modified TLC-MS interface, weakly or unbound cell lysate components are extracted and transferred to a mass spectrometer. **(d)** Remaining proteins are detected by using a specific primary and labelled secondary antibody.

For this purpose, the cell lysates were spotted onto different transfer substrates. Originally, cyclo-olefin copolymer (COC) microscope slides were used, which allowed a good sample transfer because of their self-sealing properties with the thin-layer chromatography (TLC)-interface of the mass spectrometer, which was used for the extraction of analytes. However, since protein retention was insufficient, making subsequent RPPA analysis impossible, NHS ester-functionalized glass slides were also used to immobilize biomolecules by reaction with primary amines under the formation of amide bonds (Figure 1.9b). Using these slides, it is possible to extract weakly or unbound cell lysate components while leaving stronger bound ones. In Figure 1.9c, the extracted substances are illustrated by red triangles. The blue layer around the TLC interface in the same figure is a modified sealing cap required for working with glass slides. After extraction, the analytes were first separated by high-performance liquid chromatography (HPLC), improving the sensitivity, and then analyzed in a mass spectrometer. The tested mass spectrometers were a triple quadrupole system and a high-resolution Orbitrap, both combined with ESI for sample ionization. Samples prepared on functionalized glass slides still contained proteins after sample extraction for MS measurements, which can then be analyzed by RPPA (Figure 1.9d). This newly developed correlative method for lysing cells under observation in a fluorescence microscope, analyzing cell lysate contents by mass spectrometry, and studying proteins by RPPA differs in several points from the previously presented techniques and offers some advantages and disadvantages. The method could best be classified as LLME of subcategory 2 of the ambient ionization techniques. However, compared to the methods presented there, the analytes are not extracted directly from cells and analyzed by MS but first dried on a handover slide in an intermediate step. The direct analysis would also be possible since the platinum-coated glass capillary for cell lysis is also an ESI emitter. However, it has the disadvantage that the sample cannot be transported well, and no RPPA analysis is possible since the whole sample is consumed in the ionization process. In our case, the ability to transport the samples was required as the cell lysis setup, and the mass spectrometer is located at two different sites. Also, we did not want to lose the possibility of RPPA analysis. This method's disadvantage is that the cell lysate can be damaged during the drying process and transport. Although the work was carried out in an argon atmosphere, losses and artifacts resulting from transport and transfer from one system to another are likely. These losses probably contributed to the fact that the measured signals for single cells were at or even below the detection limit. However, if several cells were deposited at the same location, the measurements were successful. This problem may be solved simply by using more sensitive mass spectrometers. Another problem that has occurred concerns the transport slides and their behavior for RPPA analysis. While RPPA analysis worked very efficiently without previous MS measurements, only traces of proteins with corresponding weak signals could be found after extraction. Although a certain loss of bound biomolecules during extraction is desirable, as it allows the analysis

of bound metabolites, even relatively strongly bound proteins that probably had various amide bonds with the slide are either removed or damaged to such an extent that only few primary antibodies can bind. Nevertheless, this new method provides a new opportunity to study cells by mass spectrometry or RPPA. This technique has proven to be especially useful for the transport between the individual instruments and complements the more established methods presented above. However, the combination of all steps together for a single cell needs further optimization. A more detailed description of this method, together with some results, follows in section 5.

2. Microfluidic Sample Preparation for Transmission Electron Microscopy

An instrument and methods for the preparation of nanoliter-sized sample volumes for transmission electron microscopy is presented. No paper-blotting steps are required, thus avoiding the detrimental consequences this can have for proteins, significantly reducing sample loss and enabling the analysis of single cell lysate for visual proteomics.

My contribution to the following publication was writing the script and the paper, producing the movie, developing the cell and grid preparation protocols, designing and implementing several parts of the setup and performing the systematic ice thickness variation experiment.

The following section has been published in:

Journal of Visualized Experiments
Issue 137, July 2018, Pages 1-12
http://dx.doi.org/doi:10.3791/57310

Miniaturized Sample Preparation for Transmission Electron Microscopy

Luca Rima[*,1], Claudio Schmidli[*,1,2], Stefan. A. Arnold[*,1,2], Thomas Stohler[1]
Anastasia Syntychaki[1] Andrej Bieri[1],Stefan Albiez[1], Kenneth N. Goldie[1],
Mohamed Chami[3], Henning Stahlberg[1] and Thomas Braun[1]

* These authors contributed equally to this work

1 - Center for Cellular Imaging and NanoAnalytics, Biozentrum, University Basel, Switzerland
2 - Swiss Nanoscience Institute, University of Basel, Switzerland
3 - BioEM lab, Biozentrum, University of Basel, Switzerland

Contents

2.1. Introduction **32**
2.2. Protocol **34**
2.3. Representative Results **45**
2.4. Discussion **50**

Abstract

Due to recent technological progress, cryo-electron microscopy (cryo-EM) is rapidly becoming a standard method for the structural analysis of protein complexes to atomic resolution. However, protein isolation techniques and sample preparation methods for EM remain a bottleneck. A relatively small number (100,000 to a few million) of individual protein particles need to be imaged for the high-resolution analysis of proteins by the single particle EM approach, making miniaturized sample handling techniques and microfluidic principles feasible.

A miniaturized, paper-blotting-free EM grid preparation method for sample preconditioning, EM grid priming and post processing that only consumes nanoliter-volumes of sample is presented. The method uses a dispensing system with sub-nanoliter precision to control liquid uptake and EM grid priming, a platform to control the grid temperature thereby determining the relative humidity above the EM grid, and a pick-and-plunge-mechanism for sample vitrification. For cryo-EM, an EM grid is placed on the temperature-controlled stage and the sample is aspirated into a capillary. The capillary tip is positioned in proximity to the grid surface, the grid is loaded with the sample and excess is re-aspirated into the microcapillary. Subsequently, the sample film is stabilized and slightly thinned by controlled water evaporation regulated by the offset of the platform temperature relative to the dew-point. At a given point the pick-and-plunge mechanism is triggered, rapidly transferring the primed EM grid into liquid ethane for sample vitrification. Alternatively, sample-conditioning methods are available to prepare nanoliter-sized sample volumes for negative stain (NS) EM.

The methodologies greatly reduce sample consumption and avoid approaches potentially harmful to proteins, such as the filter paper blotting used in conventional methods. Furthermore, the minuscule amount of sample required allows novel experimental strategies, such as fast sample conditioning, combination with single-cell lysis for "visual proteomics", or "lossless" total sample preparation for quantitative analysis of complex samples.

2.1. Introduction

Hardware and software for the structural analysis of protein complexes by transmission electron microscopy (TEM) has massively advanced during recent years. The improvements made paved the way to a "resolution revolution" [Kuhlbrandt 2014, chen Bai *et al.* 2015] and fundamentally changed structural research. The revolution started with the advent of cryo-electron microscopy (cryo-EM) [Dubochet *et al.* 1988, Lepault *et al.* 1983] allowing the preparation of biological samples under close to physiological

conditions while decreasing radiation sensitivity and preventing sample evaporation in the high vacuum of the transmission electron microscope [Baker & Rubinstein 2010]. In the following years, incremental technological progress gradually increased the resolution achievable. Among these innovations were the application of field-emission guns [Crewe *et al.* 1968, Zemlin 1994], and, more recently, improved data analysis algorithms, such as maximum likelihood methods [Scheres 2012, Grigorieff 2007]. Direct electron detector cameras [Li *et al.* 2013, Milazzo *et al.* 2011, Ruskin *et al.* 2013, Veesler *et al.* 2013], movie-mode imaging and the accompanying software developments [Campbell *et al.* 2012, Ripstein & Rubinstein 2016, Li *et al.* 2013, McLeod *et al.* 2017], provided the final breakthrough required to achieve atomic resolution for biological samples by single particle analysis (for a review see [Cheng *et al.* 2015]). The importance of cryo-EM was recently recognized by the award of the Nobel prize for chemistry to three of the pioneers.

To image a biological sample by TEM, the method used to load the EM grid with sample (subsequently referred to as "grid preparation") must ensure that the resulting sample layer (i) is thin enough $\leq$100 nm to avoid extensive noise by inelastic or multiply scattered electrons; (ii) withstands the high vacuum of the electron microscope, and, (iii) protects the biomolecules from radiation damage. Two main methods are used to fulfill these perquisites: Negative stain (NS) [Brenner & Horne 1959, Carlo & Harris 2011] procedures (Figure 2.1A) adsorb the sample to a thin carbon film, embed the biomolecules in amorphous heavy metal and then allow the assembly to dry in air. This is simple and quick, and the loaded EM grids (subsequently referred to as "sample grids") are easy to store and can be kept for extended periods of time (generally years). In TEM, the preparations exhibit high contrast due to the NS and tolerate higher electron doses than cryo-preparations, but the resolution is limited to approximately 20 Å. Cryo-EM procedures (Figure 2.1B) employ holey carbon supports. A thin film of the sample solution is spanned across the holes and the EM grid is plunged into a cryogen, usually liquefied ethane, to rapidly cool it below $-150\,^{\circ}$C. The result is an amorphous, vitrified, 50 to 100 nm-thick film of the solution in the support holes. This thin, amorphous film withstands the high vacuum in the electron microscope and, in the ideal case, preserves biological structures in their native state. The procedure allows biological samples to be imaged at high-resolution. However, the sample grid must be kept at temperatures below $-150\,^{\circ}$C at all times to avoid devitrification. It can be imaged using relatively high electron doses due to the low temperature, but the contrast and signal-to-noise ratio is nevertheless low. Therefore, averaging techniques are employed to increase contrast and, provided the sample is imaged from different angles, a high-resolution three-dimensional (3D) map can be reconstructed. The most commonly used and highly successful method for 3D reconstruction in our days is the single particle approach. For a recent review see [Cheng *et al.* 2015].

Negative stain TEM (NS-EM) is important for screening and quality control, when

high-contrast is needed or when only limited amounts of sample are available (adsorption to the carbon film generally concentrates the sample). Single particle cryo-EM is the gold-standard method if high-resolution 3D reconstructions of the protein structure are aimed for. Unfortunately, the grid preparation methods used for NS and cryo-EM have not improved significantly since they were invented. Current drawbacks are the high sample consumption (approx. 3 µL of 1 mg protein) and the large amount (>99 %) of sample lost (Figure 2.1A,B). Furthermore, the classical method used to prepare grids for cryo-EM is a harsh procedure for proteins: First, it involves an extensive face-on paper-blotting step (Figure 2.1B, ii), and, second, the protein is exposed to the air-water interface for a significant amount of time [Glaeser 2016]. Here, an alternative method for sample pre-conditioning, sample grid preparation and post-processing (grid drying or vitrification) for NS-EM (Figure 2.1C) or cryo-EM (Figure 2.1D) is presented. The in-house built setup, called "cryoWriter", uses miniaturized sample handling technology and microfluidic principles to aspirate, condition and dispense sample, avoiding paper blotting completely and providing alternative methods to thin samples for cryo-EM. It significantly reduces sample consumption and improves user-control over sample preparation as a whole. Furthermore, the method allows novel experimental applications; such as the preparation of isolated biological components of individual cells in an approach called "single cell visual proteomics" [Engel 2009, Kemmerling *et al.* 2012, Arnold *et al.* 2016, Kemmerling *et al.* 2013].

2.2. Protocol

A "cryoWriter" (Figure 2.2; for details see [Arnold *et al.* 2016, Arnold *et al.* 2017, Ramakrishnan *et al.* 2014]) or equivalent instrumentation is required for the following protocols. A list of suppliers for the main parts and consumables is given in the **Table of Materials**.

1. Negative Stain (NS) Grid Preparation

1.1. Turn on the instrument and start up the software. Initialize all necessary modules (syringe pump controller, motorized stages, surveillance cameras, and dew point stage).

1.2. Cool the sample support and the dew-point stage. If required, make sure that the dew-point stage temperature is regulated 1-2 °C above the dew point.

Note: The stage is cooled by a commercial Peltier device with a PID controller.

1.3. Prepare NS by filling a 100 or 200 µL PCR tube with 100-150 µL of NS (e.g.,

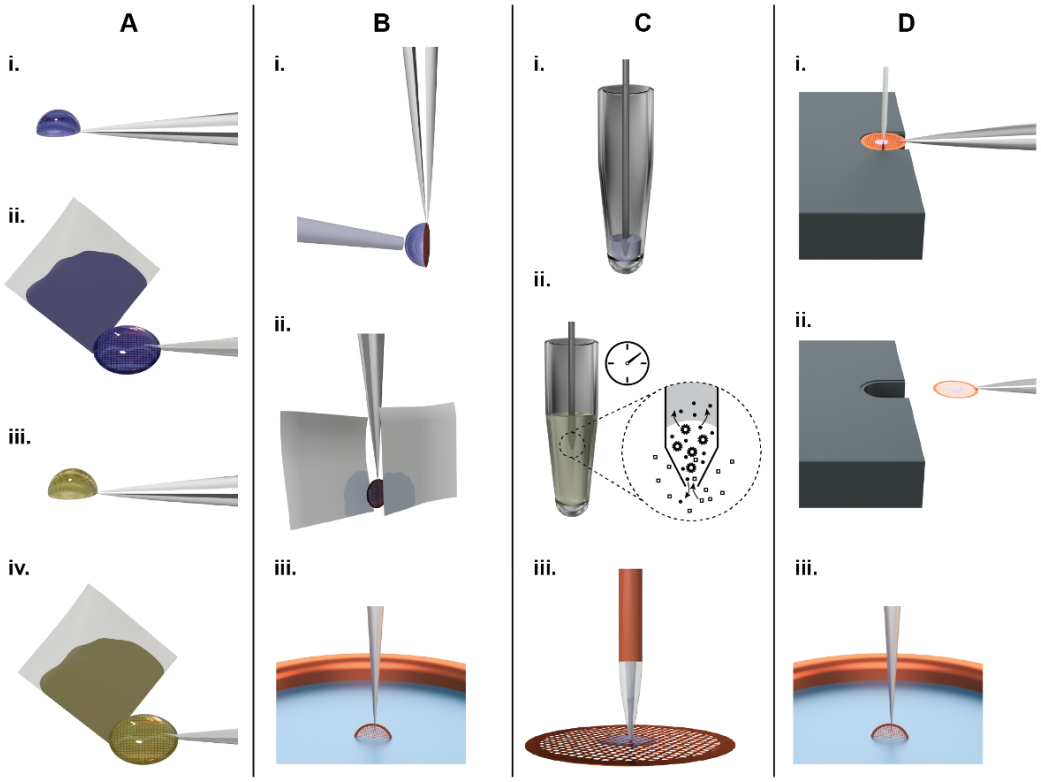

Figure 2.1: Principles of TEM grid preparation and comparison between the classical (panel A, B) and a microfluidic approach (panel C, D). **A)** Classical NS-EM grid preparation: About 3 µL of sample are pipetted by hand onto an EM grid covered with a continuous carbon film (subsequently referred to as an 'NS-EM grid') (i). After incubation for approx. 10 s, filter paper is used to blot away the excess liquid from the side (ii), leaving the adsorbed biomolecules in a thin water film. Subsequently, the protein is incubated in a heavy metal salt solution, e.g., 2 % uranyl acetate, for 20 s (iii), and again the liquid is removed by blotting from the side using filter paper (iv). Finally, the EM-grid is left to dry in air. **B)** Classical cryo-EM grid preparation: About 3 µL of sample are pipetted by a hand onto a holey carbon film. To form a thin sample film, the surplus liquid is removed by paper-blotting face-on from one or both sides (ii). Finally, the grid is rapidly plunged into liquid ethane for vitrification (iii). **C)** NS-EM grid preparation using the cryoWriter setup: A 5 nL volume is aspirated from the sample stock using a microcapillary (i). For sample conditioning, the microcapillary tip is immersed into the conditioning solution, e.g., 2 % ammonium acetate. Ions and small molecules are exchanged by diffusion (ii). Note that the dimensions of the microcapillary ensure that the whole process is diffusion driven. Proteins have much lower diffusion constants than salt ions and are not significantly lost [Arnold *et al.* 2016]. Finally, the sample is dispensed onto the grid and allowed to dry (iii).

(continued)

Figure 2.1: D) Principles of cryo-EM grid preparation using the cryoWriter-based method: An EM grid covered with a holey carbon film is placed on the surface of a temperature-controlled platform and held by tweezers. The temperature of the platform is controlled at an offset from the dew point temperature of the grid environment. The grid is moved relative to the microcapillary containing the sample and the microcapillary is lowered until it is a few micrometers above the grid. Subsequently, a few nanoliters of sample are dispensed from it while the stage is moved in a spiral pattern; excess liquid is re-aspirated (i). After EM grid priming, the microcapillary is withdrawn and the grid remains on the temperature controlled platform (subsequently referred as dew point (DP) stage) for a short time to allow a controlled amount of sample to evaporate. For plunge freezing, the grid is rapidly withdrawn from the stage using the tweezers (ii), flipped by 90° into the vertical position, and plunged into a cryogen bath (iii) (subsequently referred to as 'pick-and-plunge' mechanism).

2 % methylamine tungstate). Place the tube on the cooled sample support of the instrument.

1.4. Position the sample

1.4.1. Put the sample 0.5-1 µM into a 100 or 200 µL PCR tube. If less than 50 µL of sample is available, cut off the bottom of a PCR tube with a razor blade and use it as a sample well. This will ensure that the microcapillary can easily reach the sample.

Note: It is easiest to aspirate samples from 100 or 200 µL PCR tubes, because the microcapillary used later to aspirate the sample is slightly tilted and the travel-height z-axis direction is limited.

1.4.2. Place the PCR tube/container on the cooled sample support in the instrument to prevent evaporation. Alternatively, samples can be aspirated from well plates in the microscope stage top incubator at room temperature; cooling is not implemented for well plates.

1.5. Define positions. Use the cryoWriter joystick that controls the motorized xy-stage and software control buttons for the linear x-, y-, and z-axis stages to position the microcapillary. Use the camera to check the position of the capillary.

1.5.1. Move the microcapillary to the sample reservoir. Immerse the tip into the sample liquid and save this position as "sample".

1.5.2. Move the microcapillary to the NS PCR tube, immerse the tip into the NS solution and save this position as "stain".

1.5.3. Place the microcapillary roughly 100 µm above the center of the slot where

the EM grid will be positioned and save this position as "grid_save".

1.6. Aspirate sample and condition it for NS-EM.

1.6.1. If not already installed, mount a 10 µL syringe (0.46 mm inner diameter) on a precision syringe pump.

1.6.2. Glue one end of a 30 cm long fused silica microcapillary (outer diameter 360 µm, inner diameter 150 µm) to the syringe outlet.

1.6.3. Connect the other end of the microcapillary to a short (5 cm) long tapered microcapillary via press fit connector. The tapered tip of the short microcapillary forms the dispensing tip.

1.6.4. Fill the syringe with degassed double-distilled water (ddH_2O; system liquid) and avoid the formation of air bubbles.

1.6.5. Dispense a few tens of nanoliters of system liquid and remove any drops from the microcapillary with a lint-free tissue.

1.6.6. Double-click on the saved sample position. This positions the microcapillary in the sample well. While the capillary is moving, dispense 3 x 0.5 nL of system liquid just before the microcapillary tip is immersed into the sample to prevent air bubble from being trapped there (see note 2 below).

IMPORTANT NOTE: (1) When switching from aspiration to dispensing mode or vice versa, there is a small loss in piston stroke due to backlash in the gears of the syringe pump. According to the manufacturer, the backlash of a new unit lies between 7 and 12 µm. For our syringe with a barrel diameter of 0.46 mm, this translates to 1-2 nL. Therefore, 1-2 nL can be "dispensed", before sample is actually dispensed. Usually, a tiny droplet starts to exit the microcapillary tip after the third 0.5 nL dispense step. (2) An air bubble trapped above/below the sample would make dispensing less accurate and prevent sample conditioning by diffusion.

1.6.7. Leave the microcapillary immersed for 3-12 min, depending on the sample buffer and nozzle geometry.

Note: The higher the salt and/or phosphate concentration in the buffer, the longer the required immersion time. NS (relatively quick) diffuses into the sample plug while buffer salts (relatively fast) and protein (much slower) diffuse out. This lowers the concentration of buffer salts in the sample preventing them from crystallizing when the loaded grid dries.

Further, phosphate tends to form a precipitate in combination with NS.

1.7. Prepare a grid and deposit a spot of the conditioned sample.

1.7.1. While the sample is being conditioned, take a piece of adhesive tape and a PDMS block and clean the top side of the PDMS by applying and removing the adhesive tape to ensure that there is no dust. Put the PDMS block in a Petri dish.

Note: New PDMS blocks are taken from the clean room.

1.7.2. Carefully pick up a grid (e.g., Cu, 200 or 400 mesh coated with Parlodion/C film). Make sure to touch only the edge of the grid with the tweezers. Place it on the clean PDMS block with the carbon film facing upwards.

1.7.3. Place the PDMS block with the grid in an air glow-discharge unit and glow discharge it for 20 s with 100 W power at 0.4 mbar. Store the grid in a closed Petri dish. Longer glow discharge times generally lead to a larger spreading of the deposited sample volume on the grid. As a result, the stain layer becomes thinner (weaker stain).

1.7.4. 1 min before the immersion time is up, grasp the glow-discharged grid with the cryoWriter tweezers. Make sure the electromagnet is turned ON; otherwise turn it on in the software. Mount the tweezers on the electromagnet and use the manual micromanipulator screw to align the grid flat on the dew-point stage, carbon film side up. Make sure that the dew-point stage temperature is regulated 1-2 °C above the dew point to reduce the rate of evaporation after sample is loaded.

1.7.5. When the immersion time is up, double-click on "grid_save". The microcapillary tip will be placed safely above the grid surface. Manually bring the microcapillary tip into contact with the grid. Lift the nozzle by 10 µm and position it above the center.

CAUTION: Some samples containing detergents tend to move up along the outer surface of the microcapillary when liquid is dispensed due to the lower surface tension. It is important to be very close to the grid surface to prevent such losses.

1.7.6. Dispense 5 nL of sample onto the grid. On a dry day, when rapid evaporation takes place at the microcapillary tip, one can also slowly dispense until the sample is at the very tip, and then quickly dispense 5 nL.

1.7.7. Withdraw the microcapillary and let the conditioned sample dry slowly on the dew point stage (DP-stage).

1.7.8. Once the sample spot has dried, remove the grid and store it at room temperature in a grid box or Petri dish.

1.7.9. Dispense 500 nL of system liquid from the microcapillary and remove it with a lint-free tissue. Flush the capillary 5 times with either ethanol, detergent or 1 M NaOH. This cleans the microcapillary allowing it to be used with a different sample.

2. Cryo Grid Preparation

2.1. To prepare the instrument and sample, follow steps 1.1 to 1.5 described above. If NS is not required omit steps 1.3 and 1.5.2. To exchange the sample buffer or condition the sample for cryo-EM by dialysis, e.g., to reduce the concentration of buffer salts or to introduce additives (e.g., trehalose, detergents) use the desired buffer instead of NS in steps 1.3 and 1.5.2.

2.2. Prepare liquid ethane in a standard cryo container.

2.2.1. Assemble the ethane cup, cryo box holder, and spider and fill the cryogen container to the brim with liquid nitrogen; usually requires about 200 mL. Wait a few minutes until the ethane cup has cooled down and is free of liquid nitrogen.

2.2.2. Open the ethane gas bottle and slowly let the gas stream into the ethane cup. Let it fill with liquid ethane until the level is 2-3 mm below the top; this takes a few minutes and requires about 5 mL of liquid ethane.

2.2.3. Take a cryo box and place it in a free slot in the cryogen container.

2.2.4. Remove the spider, place the polystyrol lid on top, and place the cryogen container on the mounting in the cryoWriter.

2.3. Glow discharge an EM grid.

2.3.1. Take a piece of adhesive tape and a polydimethylsiloxane (PDMS) block and clean the top side PDMS by applying and removing the adhesive tape (removes any dust). Put the PDMS block in a Petri dish.

2.3.2. Carefully pick a grid from the grid box. Make sure to touch only the edge of the grid with the tweezers. Place it on a clean PDMS block with the holey carbon film facing upwards.

2.3.3. Place the PDMS block with the grid in a plasma cleaner and plasma-

clean the grid surface (e.g. use 75 % Ar/25 % H_2, power 50 W, pressure 25 mTorr). Place the PDMS block with the glow-discharged grid in a Petri dish.

2.4. Position the grid in the instrument

2.4.1. Grasp the glow-discharged grid with the cryoWriter tweezers. Make sure the electromagnet is turned ON; otherwise turn it on in the software. Mount the tweezers on the electromagnet and use the manual micromanipulator screw to align the grid flat on the stage, carbon film side up.

2.4.2. Double-click on "grid_save". Adjust the microcapillary position so that the tip is approx. 10 µm above the grid surface. Make sure that the microcapillary can move freely across the grid without touching it anywhere, if necessary withdraw the microcapillary a few micrometers.

2.4.3. Go back to the center of the grid and save the new position as "grid".

CAUTION: Correct naming is mandatory for the macro script to work.

2.5. Write sample and plunge-freeze grid.

2.5.1. Initialize the transistor to transistor logic (TTL) module in the control program, which is required to trigger the plunge mechanism.

2.5.2. Flush the microcapillary with a few tens of nanoliters of system liquid and remove any drops from the microcapillary with a lint-free tissue.

2.5.3. Start macro script. The macro will perform the following steps:

2.5.3.1. Dispense 5 nL (to remove any air bubbles at the tip) and go to sample position.

2.5.3.2. Aspirate 65 nL of sample. Infuse 5 nL back into the sample tube. This accounts for system backlash and allow synchronized writing, i.e., to ensure that dispensing and stage movement start at the same time.

2.5.3.3. Move to "grid" position.

2.5.3.4. Initiate 'writing pattern', which will cause the microcapillary to move across the grid, simultaneously dispensing 45 nL of sample.

2.5.3.5. Afterwards, move the microcapillary back to the center of the grid,

lower it another 10 µL, and withdraw excess sample liquid.

2.5.3.6. Withdraw the microcapillary and turn off the electromagnet. This releases the tweezers and initiates plunge freezing.

2.6. Grip the tweezers and carefully release the magnetic adapter from the plunger. Quickly transfer the grid from the ethane cup into the cryogen container containing the cryo box and place the grid in a free slot.

3. Single-cell Lysate Preparation

3.1. Prepare the microcapillaries for electroporation.

Note: The tapered (laser-pulled and inspected) fused silica microcapillaries have a protecting polyimide coating on the outside, except for the tip, where the coating is burnt off during the tapering process.

3.1.1. To coat the microcapillaries with a conductive layer, mount them at an angle of 45° on a metal rail, with the tips pointing upwards. Use an aluminum foil to shield the lower end (2 cm) of the tips, as uncoated polyimide forms the best seal with the press-fit connectors employed later.

3.1.2. Sputter deposit a sticky layer of 20 nm Ti/W, and then a 200 nm-thick layer of Pt.

3.2. Make the microcapillary tip hydrophobic.

3.2.1. Prepare a 1 M solution of 1-dodecanethiol in EtOH.

3.2.2. Glow-discharge the microcapillary in air for 1 min with 100 W power at 0.4 mbar.

3.2.3. Immerse the tip of the microcapillary in the 1 M solution of 1-dodecanethiol for a few hours (ideally overnight). It is best to prepare tips freshly one day before use.

3.3. Install a new microcapillary.

3.3.1. Remove the microcapillary from the 1-dodecanethiol solution, rinse the outside with ethanol and flush the inside with ethanol using a syringe.

Note: If no functionalized microcapillaries are available, quickly glow discharge the tip of a microcapillary and dip it in a drop of commercial car window treatment, which is a mixture of PDMS and sulphuric acid. The resulting hydrophobic functionalization is not as good as with

1-dodecanethiol, but generally sufficient.

3.3.2. Cleave its uncoated end with a capillary cutter.

Note: A clean cut is important for a good seal with the press-fit connector.

3.3.3. Use a toothpick to apply silver paste to the sharp boarder formed between glass and the polyimide coating when the polyimide coating was burnt off by the laser during capillary pulling.

Note: This reinforcement is necessary as the Pt coating is very weak in this region, and electrical conduction can easily break down.

3.3.4. Wash the polyimide end of the microcapillary with acetone. Leave a small drop of acetone at the end and insert it into the orifice of the press-fit connector. Apply light pressure to form a good seal.

3.4. Calibrate the microcapillary position.

3.4.1. Turn on the instrument and start the software as described in step 1.1. Additionally, initialize the microscope camera and the function generator.

3.4.2. Place a glass microscope slide into the slide holder on the microscope.

3.4.3. Lower the microcapillary close to the glass slide and center it over the microscope objective until it appears in the microscope camera view. Use the x- and y- axis linear stages to position the tip of the microcapillary at the center of the image. Then slowly lower the tip until it slightly touches the glass slide.

CAUTION: Choose very small steps (5 µm) towards the final approach. Otherwise, the tip can be damaged.

3.4.4. Press the "Calibrate Nozzle" button. This retracts the microcapillary 40 mm, and sets this position as home position.

3.5. Preparation of stamped PDMS pieces and ITO slides.

3.5.1. Mix PDMS and crosslinker in 10:1 ratio, pour into a large Petri dish to a depth of about 2-3 mm. Bake at 60 °C for a few hours in a hybridization incubator or similar device.

3.5.2. With a hammer and a stamp (12 mm diameter), cut holes in the PDMS layer. Afterwards, use a scalpel to cut out 2 cm long squares or rectangles

including the holes to obtain stamped pieces that fit on a microscope slide. Usually, two stamped pieces are mounted on one microscope slide.

3.5.3. Wash the PDMS pieces and the ITO slides first with detergent and then with 70 % ethanol. Place them, wet, in a Petri dish and let the ethanol fully evaporate in an oven at 60 °C.

3.5.4. Glow-discharge the ITO slides for 1 min with 100 W power at 0.4 mbar and then apply 1 mL of coating solution (e.g., poly-L-lysine (PLL)). Incubate for 5 min, remove the solution with a pipette, and apply 1 mL of ddH_2O. Slightly agitate for 1 min, and then remove the ddH_2O using a pipette. Let the slides dry at 60 °C.

3.6. Prepare the cell culture. Follow standard adherent-cell culturing protocol (e.g., [Arnold *et al.* 2016, Kemmerling *et al.* 2013]). Seed cells on ITO during normal splitting/passaging runs.

3.6.1. Take a freshly PLL-coated ITO slide and add a PDMS piece. Apply some pressure to form a watertight seal. This produces small wells with the slide as their base.

3.6.2. Add about 300 µL of cells suspended in fresh medium to the PDMS wells. The seeding density should be around 75,000 cells per well.

3.6.3. Incubate the ITO slides for 1-2 d days under standard conditions.

3.7. Prepare for cell lysis experiment:

3.7.1. Pre-warm a few milliliters of the electroporation buffer (e.g., phosphate buffered saline (PBS)).

3.7.2. Set up the instrument according to steps 1.1-1.5 (for NS) or step 2.1 (for cryo).

3.7.3. Load the standard lysis parameters, e.g., the lysis voltage.

3.7.4. This is a good moment to prepare the cryogen for cryo (steps 2.2).

3.7.5. Take the ITO slide from the incubator, and mount it on the microscope insert. Use two screws to fix the slide on the aluminum insert and to ensure electrical contact between the ITO coating of the slide and the electrically grounded aluminum frame.

3.7.6. Remove the cell culture medium and wash twice with 300 µL of electroporation buffer. Keep the cells in electroporation buffer.

3.7.7. Place the aluminum insert holding the ITO slide in the live-cell incubator stage on the setup.

3.7.8. Locate the cell culture in the microscope view and choose an area with no cells. Approach the tip to the ITO surface and gently touch it, then withdraw the tip 100 µm and save the position as "cells".

3.7.9. Quickly leave the cell culture and flush the microcapillary tip with a few tens of nanoliters of system liquid then put it into the cell culture again. Dispense a few nanoliters during immersion into the PDMS well to ensure that no air bubbles are trapped at the tip.

3.7.10. Gently approach the ITO surface (initially, you must be at position "cells", i.e., 100 µm above the surface). Upon contact, retract the tip 10 µm.

3.7.11. Select a nearby cell for lysis. Place the tip of the microcapillary above the targeted cell.

3.8. Start the macro script for single-cell lysis.

3.8.1. Name the position the microcapillary should be moved to after a cell has been successfully lysed. This will be the NS reservoir (NS-EM), a desalting buffer (cryo-EM) or the EM grid (cryo-EM). Avoid spelling errors and press "ok".

3.8.2. The macro proceeds without user intervention:

(i) The microscope stage and cell culture 100 µm are moved to the left, a snapshot of the targeted cell is taken, and 50 nL of ddH_2O system liquid are dispensed from the microcapillary. This displaces and dilutes the high salt buffer and applies osmotic pressure to the cell.

(ii) The stage is moved back to position the tip above the targeted cell again. The predefined voltage burst is applied, and after 500 ms the pump system starts to aspirate 3 nL of sample at a flow rate of 2 µL min^{-1}.

(iii) The stage is moved to the left again, allowing the cell to be inspected. A window appears, asking for user input.

3.8.3. Say whether the lysis step was successful or not.

3.8.3.1. If the answer is no, take over, flush the microcapillary and target a new cell.

3.8.3.2. If the answer is yes, a snapshot of the removed (lysed) cell is taken, and afterwards the microcapillary is moved to the location specified in 3.8.1. If this is NS or a buffer reservoir, use the standard user interface to dispense 3 x 0.5 nL of liquid while the microcapillary is moving to ensure that there are no air bubbles. The tip is immersed in the reservoir liquid by the macro.

3.9. Continue to condition the sample and/or prepare grids as explained in sections 1.6.9 1.7.9 for NS-EM or section 2.2 2.6 for cryo-EM.

2.3. Representative Results

The "cryoWriter" setup was developed (depicted in Figure 2.2) in order to test the miniaturized EM grid preparation procedures proposed in Figure 2.1C,D. Figure 2.2A shows an overview of the various components mounted to an inverse fluorescence microscope. A cell-culturing module is installed on the left side of the microscope; a module for EM grid preparation is located on the right. The cell-culturing module (Figure 2.2B) allows the growth of adherent eukaryotic cells and live-cell imaging of the cell culture by the light microscope. Individual cells are lysed by the combined action of osmotic shock, electroporation and aspiration of the cell content into a microcapillary (Figure 2.2B, Figure 2.6A) [Arnold *et al.* 2016, Kemmerling *et al.* 2013]. The aspirated lysate sample can then be used to prepare grids for NS- or cryo-EM. Alternatively, a stock protein solution in a PCR tube can be the sample source. The microcapillary (Figure 2.2B) employed is connected to a high-precision pump system allowing sample volumes to be aspirated and dispensed with sub-nL precision. As detailed in the protocols, all sample processing is performed within this microcapillary or on the EM grid itself without significant sample transport. For example, the same microcapillary is used to lyse individual eukaryotic cells, aspirate the lysate, condition it, and finally dispense aliquots onto EM grids. The grid preparation module consists of a movable DP-stage that allows the temperature of the EM grid placed on it to be precisely controlled (Figure 2.2C). For NS-TEM, the prepared sample grid can then simply be removed from the cold stage and allowed to dry in air at room temperature. However, the so-called coffee-ring effects that can then result need to be avoided for quantitative TEM where protein 'particles' are counted. To do so, grids are dried slowly on the DP-stage using a gradually increasing temperature gradient to slow down liquid evaporation. For cryo-EM, the temperature of the grid is kept close to the dew point; a positive offset of approx. 8 °C is chosen, allowing the controlled evaporation of sample liquid for thin film stabilization and thinning, which can be monitored by a sensor if necessary [Arnold *et al.* 2017]. After the selected thinning time, a pick-and-plunge mechanism is activated and the sample is vitrified (Figure 2.2C). Note that this plunging mechanism is not needed for NS-EM

grids, which are stored at room temperature. Figure 2.3 shows representative results obtained for NS-EM grids prepared using the cryoWriter setup. The tip of the microcapillary was loaded with 5 nL of sample from a stock solution and dipped into a reservoir of NS solution (2 % methylamine tungstate) for several minutes to allow diffusive exchange of NS and salt ions (for a theoretical discussion see [Arnold *et al.* 2016]). Afterwards, the conditioned sample was dispensed onto the thin carbon film of a NS-EM grid and dried. Figure 2.3A shows the use of a slot grid in the same way to visualize the complete droplet, as required for quantitative TEM. In order to avoid the coffee ring effect, the freshly glow-discharged grid was initially held at the dew-point temperature (no water evaporation) and then slowly warmed up on the DP-stage. Note, that for most applications (e.g., quality control of the sample or structural analysis) this slow-drying process is not needed. High-quality NS-preparations are obtained without it, as shown in Figure 2.3B,C. Conditioning times for phosphate-free low salt buffers are around 3 min, e.g., with low-salt Tris-buffer (20 mM Tris-HCl pH 7.4 with 50 mM NaCl), as shown in Figure 2.3B using tobacco mosaic virus (TMV) as sample. Figure 2.3C presents a worst-case scenario as the TMV was in PBS buffer (2.7 mM KCl, 1.5 mM KH_2PO_4, 136.9 mM NaCl, 8.9 mM $Na_2HPO_4 \cdot 7\,H_2O$, pH 7.4). Phosphate ions form transient crystals with the heavy-metal ions of NS (see Figure 2.5C), lengthening the conditioning time required (7 min). Other heavy metal salts can also be used with the grid preparation module, e.g., 2 % methylamine vanadate or ammonium molybdate (see also [Arnold *et al.* 2016]). However, uranyl acetate is not suitable; the crosslinking effect of this stain leads to aggregates if the protein sample is conditioned in solution, before adsorption to a carbon film (see Figure 2.5E) [Kemmerling *et al.* 2012]. Typical results obtained for cryo-EM grids prepared using the cryoWriter setup are depicted in Figure 2.4. Panel 4A shows a grid atlas of the area covered by vitrified sample. Panel 4B shows the homogeneity of the vitreous ice in a selected grid slot. In both cases, the sample was in 25 mM HEPES-KOH pH 7.5, 50 mM NaCl buffer containing 0.05 % Fos 14 detergent. Many samples and buffers were tested and a comparable high quality vitreous ice was obtained, but the conditions required are buffer dependent (see also discussion of Figure 2.5). Panel 4C shows apoferritin particles and a bacteriophage in Tris-HCl buffer (20 mM Tris-HCl, 50 mM NaCl; pH 7.4) imaged at high defocus to increase contrast. Panel 4D shows a 200 kDa membrane protein stabilized by amphipoles. The cryoWriter setup allows systematic screening for optimal EM-grid preparation conditions; an example is shown in Figure 2.5A (apoferritin in 25 mM HEPES-KOH pH 7.5, 50 mM NaCl, 0.05 % Fos 14). In this experiment, the vitreous ice "thinning" temperature was varied, but the thinning time (i.e., the time gap between sample application and plunge freezing) remained constant (1 s). At low offset temperatures (e.g., 8 K), the sample layer was too thick. At higher offset temperatures, the vitreous ice in the holes was thinner (10 K, 12 K), until at some stage (above 18 K) the grid became completely dry (not shown). In the results presented here, an offset of 12 K lead to a large homogeneous area of vitreous ice as indicated by the black arrows.

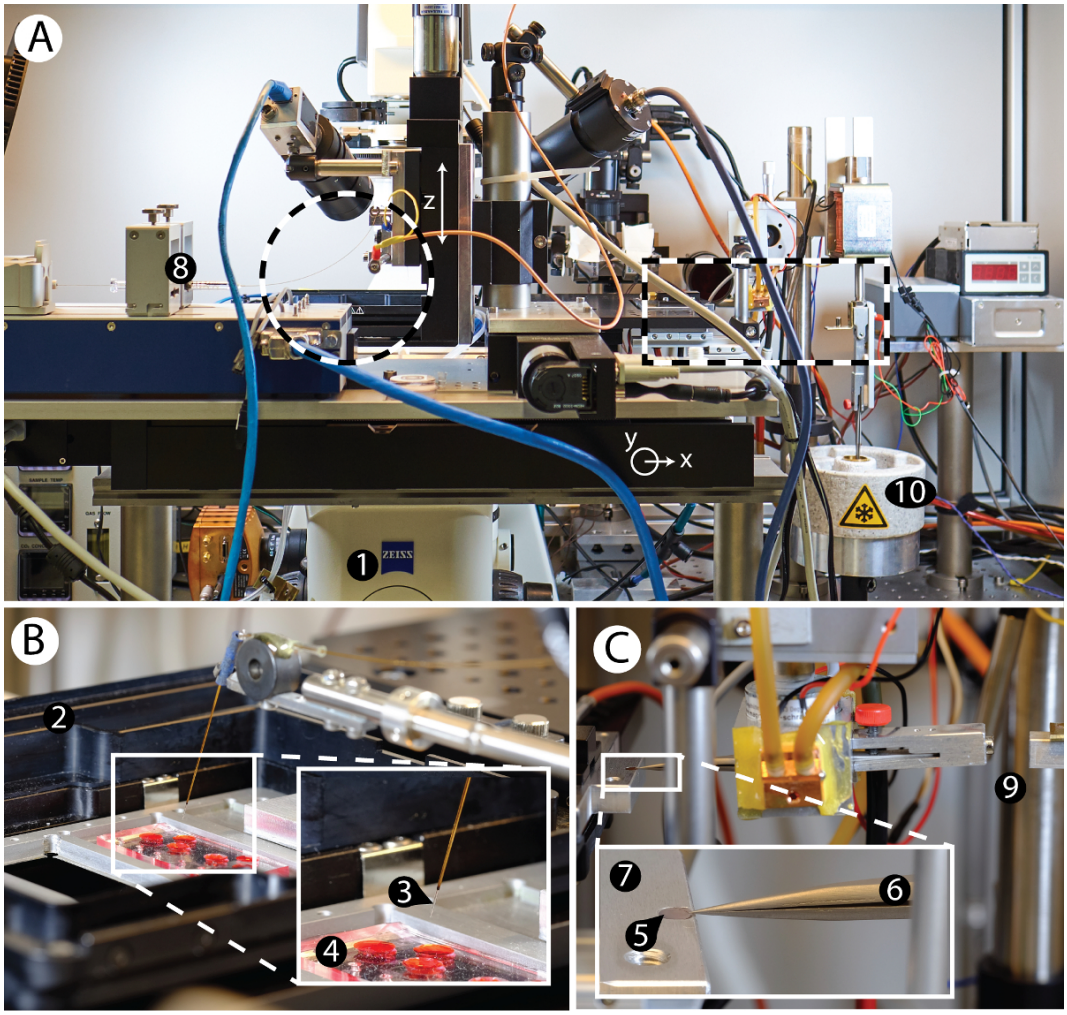

Figure 2.2: Overview of the cryoWriter setup. **A)** Overview of the cryoWriter setup mounted on an inverse light-microscope (1). **B)** Inset of area indicated on the left side in panel A. Cell culturing compartment (2), with a microcapillary (3) for sample manipulation and cell lysis positioned above a miniaturized PDMS-based cell culture plate (4). **C)** Inset of area indicated on the right side in panel A. 'Pick-and-plunge' mechanism. A holey carbon film EM grid (5) is mounted between the tips of tweezers (6) and positioned horizontally in direct contact with the temperature-controlled stage (7), referred as the dew-point stage (DP-stage) in the main text. The stage temperature is tightly controlled via a PID controller and a water-cooled Peltier element, keeping it at or close to the dew point temperature, depending on the ambient environment. The DP-stage (7) is mounted on a motorized xy axis to move the grid relative to the microcapillary. The microcapillary itself is mounted on a z-stage, and can be lowered until it is very close to the surface of the EM grid and used to dispense nanoliter-sized volumes onto the sample support covering it (a continuous thin carbon layer for NS-EM or a holey carbon film for cryo-EM). Note, liquid uptake and dispensing is performed using a high-precision pump system (8). The dispensed liquid can be distributed by moving the grid relative to the microcapillary in a spiral pattern. For cryo-EM preparation, the pick-and-plunge freezing mechanism (9) rapidly transfers the sample-loaded grid into liquid ethane (10) for rapid cooling and sample vitrification.

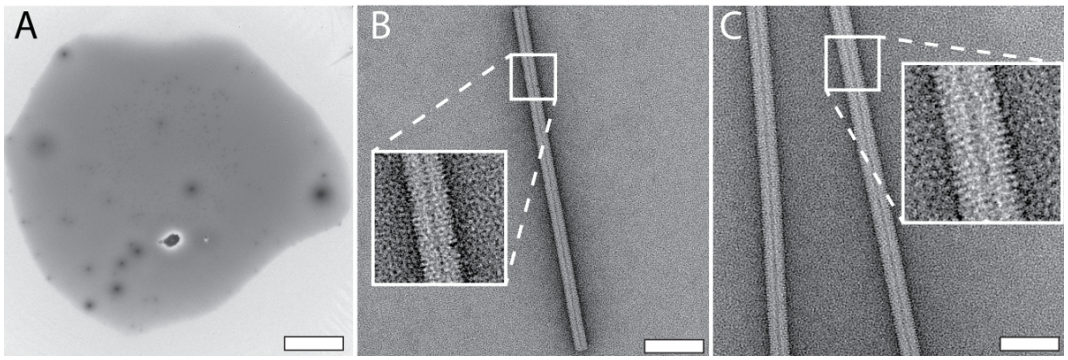

Figure 2.3: Typical results for NS grids prepared using the cryoWriter setup as indicated in Figure 2.1C. **A)** Overview image of a 3 nL droplet dispensed on a slot grid after conditioning with 2 % methylamine tungstate. **B)** TMV in 20 mM TRIS buffer. The inset shows a 3x enlargement of the indicated region. Adapted from [Arnold *et al.* 2016] (further permissions related to the material excerpted should be directed to the ACS). **C)** Tobacco mosaic virus (TMV) in PBS buffer. The inset shows a 3x enlargement of the indicated region. Adapted from [Arnold *et al.* 2016] (further permissions related to the material excerpted should be directed to the ACS). Scale bars: A, 100 µm; B, 50 nm; C, 80 nm.

Such optimization experiments can be performed with the buffer of the target sample using "test" proteins (such as apoferritin). The best conditions found are then applied to the target sample. Furthermore, grids with parameters far from the optimum can often be recognized during the preparation procedure and do not need to be screened in the electron microscope, saving significant time. Figure 2.5 also shows a gallery of typical cryo-EM (Panel B) and NS-EM (Panels C to E) artifacts specific to the cryoWriter setup. The cryo-EM grid shown in Panel 5B with TMV in PBS containing 0.1 % decyl-β-D-maltopyranoside (2.7 mM KCl, 1.5 mM KH_2PO_4, 136.9 mM NaCl, 8.9 mM $Na_2HPO_4 \cdot 7\,H_2O$, pH 7.4, 0.1 %) was excessively thinned. The background of the image is grainy because the salt concentration became too high. In general, the visual appearance of a sample does not seem to be a linear function of the salt concentration; grains suddenly become prominent when a threshold concentration is reached during the thinning process. Note, that unwanted substances can be removed by a conditioning step prior to grid preparation, as described for NS-EM in protocol section 1.6. NS can cause other artifacts. In the example shown in Panel 5C, PBS buffer (2.7 mM KCl, 1.5 mM KH_2PO_4, 136.9 mM NaCl, 8.9 mM $Na_2HPO_4 \cdot 7\,H_2O$, pH 7.4) without sample was conditioned in 2 % methylamine tungstate for 3 min. Precipitates and crystals are evident and exert extensive forces on the carbon surface leading to cracks. The precipitates only form in a certain PBS and NS concentration range and can be avoided by conditioning the sample for longer (compare Figure 2.3C). Panel 5D shows the periphery of a dispensed NS sample droplet exhibiting a "coffee ring". This would disturb quantitative, total sample analysis and can be avoided by slowing down the drying process, i.e., by keeping the

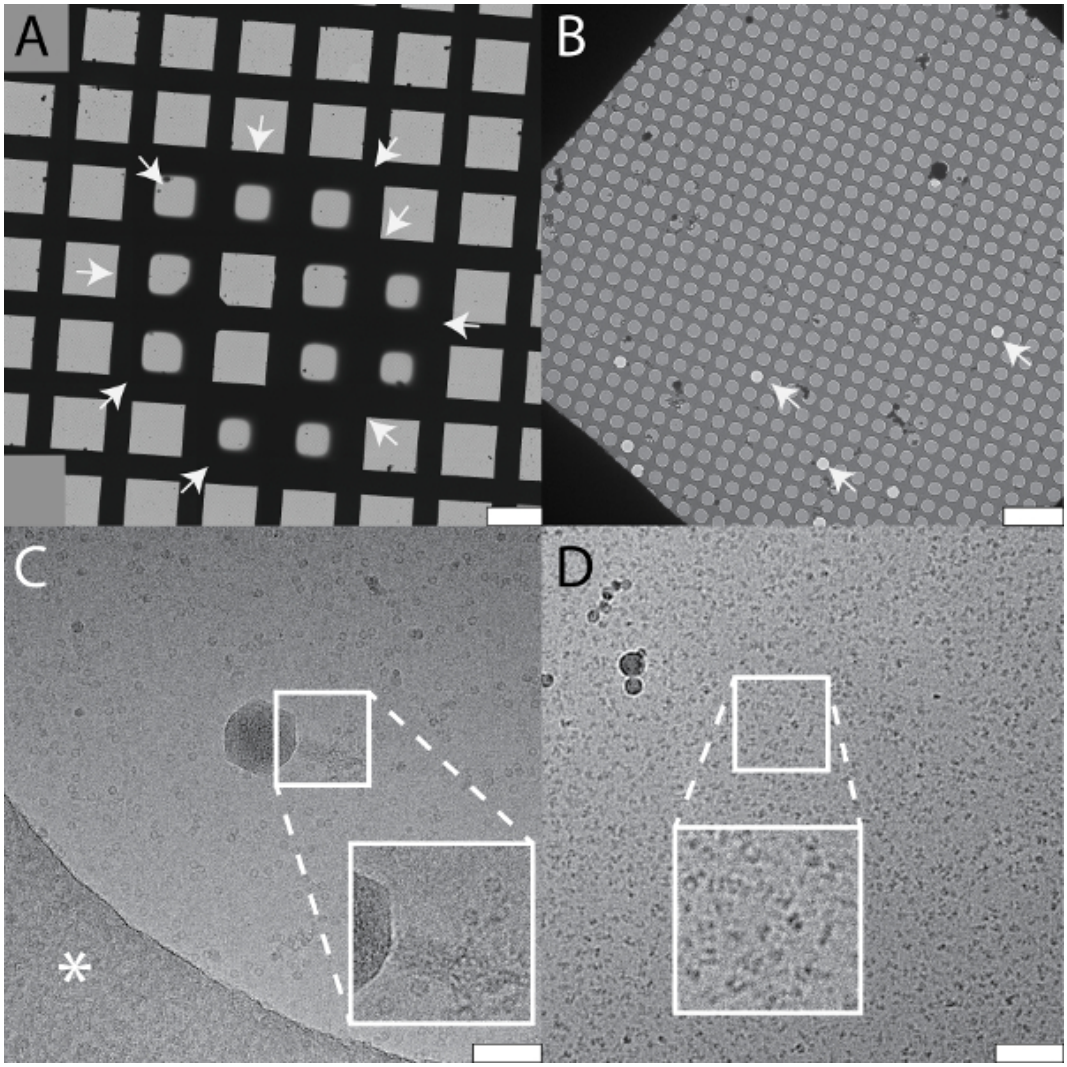

Figure 2.4: Typical results for cryo-EM grids prepared using the cryoWriter setup as indicated in Figure 2.1D. The samples and the buffers vary in the examples shown. All samples were loaded on holey carbon films. **A)** Collage of overview images ("grid atlas") of a sample containing a 150 kDa membrane protein, the periphery of the vitreous ice is indicated by white arrows. **B)** Enlarged grid slot from a grid prepared with the same buffer, showing the holey carbon film with vitreous ice. Some holes are not filled with sample buffer as indicated by white arrows. **C)** Carbon hole with vitrified sample containing apoferritin protein complexes and bacteriophages. Inset: twofold enlargement showing the tail of a bacteriophage. The white asterisk indicates the carbon film. Note that the image was recorded with high defocus to increase contrast. **D)** A 200 kDa membrane protein reconstituted in amphipols. Inset: a 2x enlargement of the indicated region shown with increased contrast. Scale bars: A, 100 µm; B, 10 µm; C and D, 80 nm.

EM grid at the dew point temperature during sample application, and then gradually increasing the temperature to dry it (see Figure 2.3A). Panel 5E (apoferritin in 20 mM HEPES, pH 7.0, conditioned 3 min) shows the crosslinking activity of 2 % uranyl acetate stain, which cannot be used to condition protein samples before they are adsorbed to carbon film supports. The small amount and volume required for EM grid preparation using the cryoWriter setup enables new types of experiments. For example, the total contents of a single cell can be collected and prepared for NS- and cryo-EM. The procedure is indicated in Figure 6A. An adherent, eukaryotic cell (HEK 293) is lysed by simultaneous electroporation and sample aspiration (Panel 6A) [Kemmerling *et al.* 2013]. A total volume of 3 nL is aspirated, which contains the cell lysate, and is retained in the microcapillary for further processing. For the NS-EM shown in Panel 6B, the cell-culturing medium was exchanged with PBS buffer (2.7 mM KCl, 1.5 mM KH_2PO_4, 136.9 mM NaCl, 8.9 mM $Na_2HPO_4 \cdot 7\,H_2O$, pH 7.4) prior to cell lysis. The cell contents were aspirated in 3 nL of buffer and conditioned in a reservoir of NS as indicated in Figure 2.1C for 10 min. Afterwards, a 5 nL volume was dispensed onto the continuous carbon film of a NS-EM grid. Individual proteins, e.g., filamentous actin, and membrane patches with attached proteins can be recognized in the image. For the cryo-EM, shown in Figure 2.6C, a volume of 3 nL was dispensed on a holey carbon EM grid without re-aspiration to remove liquid. The relatively thick film of sample formed was extensively thinned before vitrification. To do this, the DP-stage temperature was gradually increased, starting at the dew-point temperature. The thinning process was monitored by a real-time sensor-system until a pre-specified threshold was reached triggering the 'pick-and-plunge' mechanism and sample vitrification (for details see [Arnold *et al.* 2017]). Membrane structures and proteins can be recognized in the image.

2.4. Discussion

The 'cryoWriter' instrument and the protocols required to prepare sample grids for NS- and cryo-EM from nL sized total sample volumes and completely avoid the classical paper-blotting step are presented. Microfluidic principles and a micromechanical system are combined in the cryoWriter to make this possible.

Our experience shows that when the miniaturized methods presented in this manuscript are used the parameter space for EM-grid preparation is larger than for classical methods, and under tighter user control. Importantly, the increased reproducibility achieved makes it possible to pre-screen with sample buffer system, complemented with a readily available test protein, to determine the optimum parameters before the actual experiment is performed. This keeps consumption of the sample of interest to the absolute minimum and is highly recommended. Critical steps for both NS- and cryo-EM grid preparation are: (i) Priming of the pump system; for sub-nanoliter

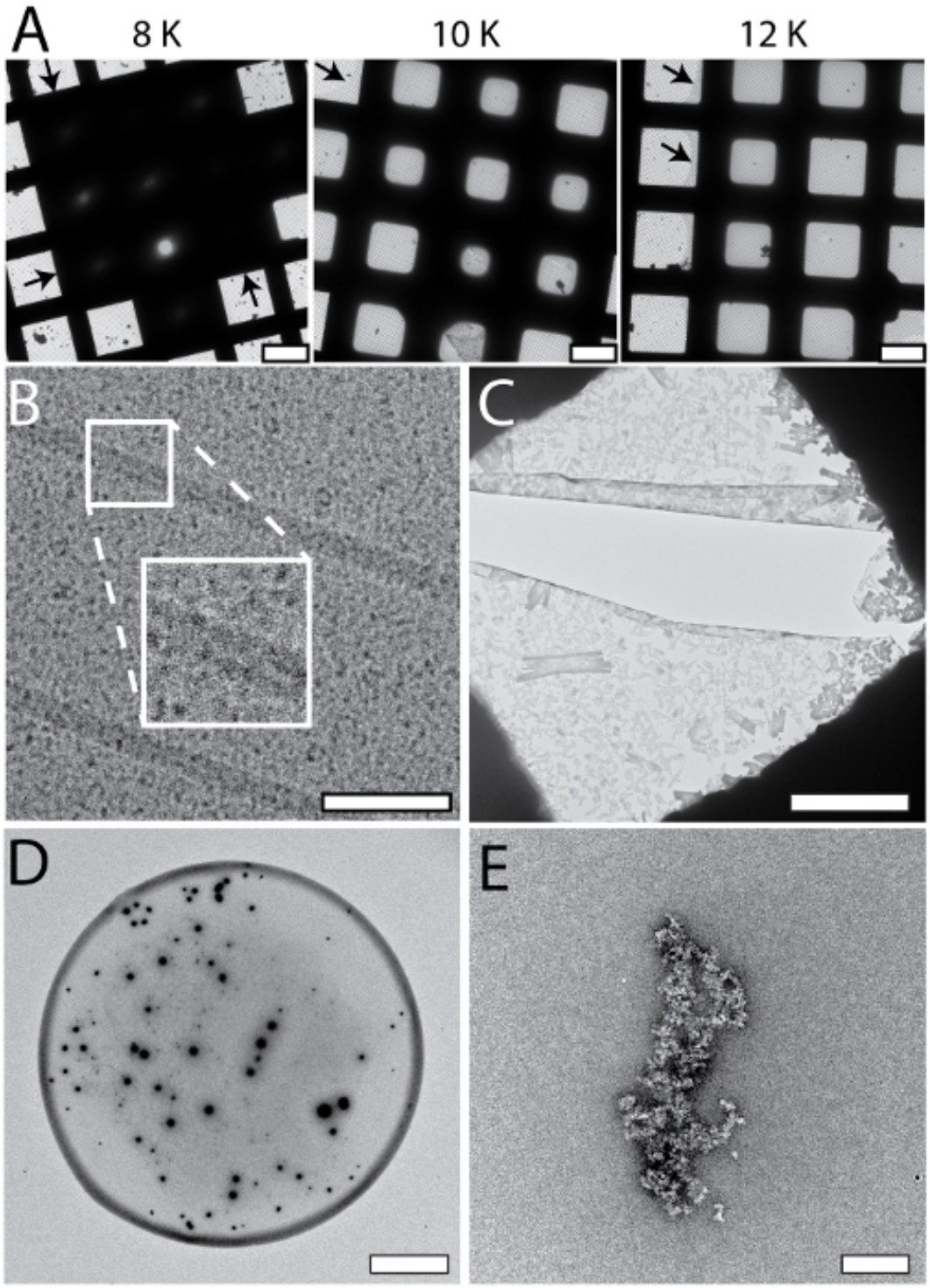

Figure 2.5: Systematic changes and artifacts observed when the cryoWriter set-up was used to prepare grids for NS- and cryo-EM.

(continued)

Figure 2.5: A) Systematic vitreous ice thickness variation; optimization of grid preparation for cryo-EM. The offset temperature of the DP-stage was varied (8 K to 12 K) keeping the thinning time constant (1 s). The arrows indicate the periphery of the sample layer. **B)** Salt effects; too highly concentrated, i.e., the thinning step was too long. The inset depicts a 2x enlargement of the indicated region. **C)** Salt precipitates formed by PBS buffer in the presence of heavy metal salts. Samples containing PBS buffer must be conditioned longer than samples in other buffers. Here, PBS buffer without sample was conditioned in 2 % methylamine tungstate for 3 min, a typical time for other sample buffers. Note the crack in the carbon film most probably due to the strong forces from the precipitates acting on the thin support during the drying process. **D)** 'Coffee ring' effect. **E)** Apoferritin conditioned in 2 % uranyl acetate for 3 min. Uranyl ions exhibit significant crosslinking activity and the apoferritin clusters form large aggregates. Scale bars: A, 80 µm; B, 80 nm C, 12 nm; D, 80 µm; E, 200 nm.

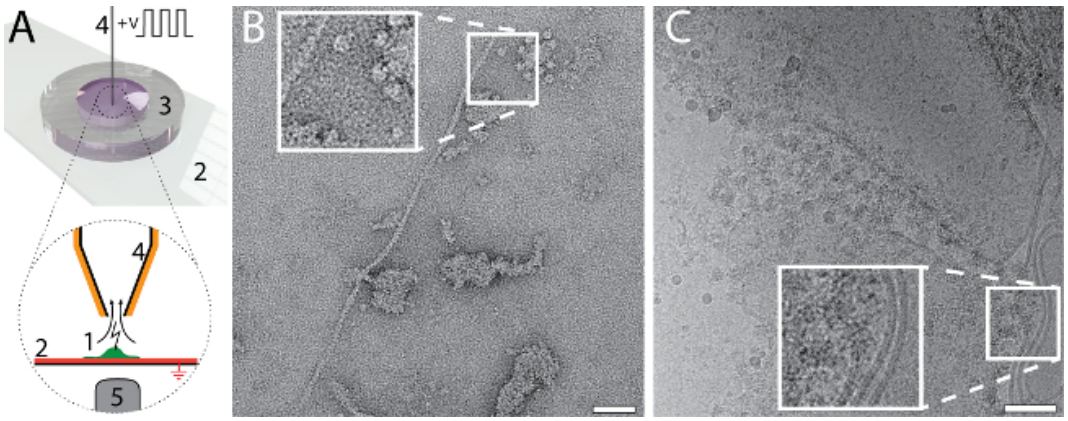

Figure 2.6: Single cell visual proteomics using the cryoWriter set-up. **A)** Lysis of a single adherent eukaryotic cell. The cell is grown (1, green) on an functionalized, ITO coated (red) glass-slide (2) in a miniaturized petri-dish (3) [Kemmerling *et al.* 2013]. The ITO layer is electrically grounded. The cell is approached by the microcapillary (4), which is coated with platinum. An initial osmotic shock (not indicated) is given to facilitate lysis, which is performed by a series of electric pulses and by the shear forces exerted during the aspiration of the cell lysate. The process can be monitored by light microscopy; the objective lens of the microscope is indicated (5). For details, see our previous work [Arnold *et al.* 2016, Kemmerling *et al.* 2013]. **B)** NS-EM image of lysate from an individual HEK 293 cell. Filamentous actin and membrane patches with attached proteins are visible. Panel adapted from [Arnold *et al.* 2016] (further permissions related to the material excerpted should be directed to the ACS). **C)** Cryo-EM image of lysate from an individual HEK 293 cell. The inset shows a 2x enlargement of the indicated region where typical membrane structures with associated proteins are visible. Panel C adapted from [Arnold *et al.* 2017]. Scale bars: B, 50 nm; C, 80 nm.

volume dispensing, the system liquid (water) must be degassed and bubble free. (ii) Precise control of the glow discharge or plasma cleaning step; the surface characteristics of the EM grid are crucial for reproducible results. (iii) Sample conditioning; the time required for conditioning, e.g., with NS, depends on the buffer type, salt content and concentration (Figure 2.3), as well as on the nozzle geometry of the microcapillary [Arnold *et al.* 2016]. (iv) Evaporation rates for NS-EM preparations for quantitative EM; the coffee-ring effect can prohibit the quantitative analysis of NS-EM preparations, and must be suppressed by slow evaporation rates controlled by the DP-stage.

Different aspects of the presented grid preparation methods can be freely combined allowing the development of versatile protocols for specific samples. Typical examples would be the removal of a substance that prevents high-resolution EM, e.g., glycerol, by a conditioning step prior to grid preparation for cryo-EM; the introduction of mediator molecules, such as ligands, by conditioning before the grids are prepared; or the examination of single cell lysate by NS- or cryo-EM (Figure 2.6).

The use of microfluidics and minimal sample amounts in the presented methods completely removes the need for paper-blotting steps. This is a great advantage, because paper blotting is a harsh treatment for proteins, potentially contaminating the sample with unwanted ions and inherently leading to massive sample loss. On the other hand, effects potentially caused by the air-water interface of the thin sample film formed when cryo-EM samples are prepared in the classical manner, are not avoided when the cryoWriter is used. Grids suitable for cryo-EM can be prepared with less than 0.2 s wait time between sample application and vitrification (data not shown). However, as proteins travel a few tenths of a nanometer in a few nanoseconds by diffusion, there is still enough time for them to collide with the air-water interface of a 100 nm thick sample film several times. However, the amount of proteins sticking to the air-water interface might be significantly reduced by these short time gaps and might prevent protein denaturation or restricted particle orientation. Another promising approach that might protect sensitive proteins from the air-water interface is to cover the sample film by low molecular weight surface-active substances. These compounds could be rapidly introduced by a conditioning step in the cryoWriter before grid preparation. The high surface-to-volume ratio of microfluidic systems is a further limitation of the cryoWriter, as sample can potentially be lost by unspecific adsorption to the microcapillary surface and disturb quantitative analysis by particle counting. The problem is addressed in two ways: First, the sample does not travel long distances within the microcapillary. Indeed, the nanoliter sample volume remains at the capillary tip throughout the processing. Second, the surface to volume ratio is further reduced by using microcapillaries with relatively large inner diameters, e.g., 180 µm. Third, the surfaces of the microcapillaries can be easily passivated if necessary, e.g., by treating them with commercially available polylysine ethanol glycols (PLL-PEG).

The high-resolution analysis of proteins by the single particle approach used in EM only requires 100,000 to a few million images of individual protein particles. This means that microfluidic techniques can provide enough protein complexes for the structural investigation. A miniaturized immuno-precipitation method for the fast isolation of protein-complexes (around 1 hour) from minimal cell amounts (approx. 40,000 cells) was developed earlier [Giss *et al.* 2014]. This method will now be directly linked to the miniaturized sample preparation stage of the cryoWriter. The final goal is to develop an integrated microfluidic pipeline for ultra-fast protein isolation and cryo-EM grid preparation that requires less than two hours in all. Furthermore, as demonstrated by Figure 2.6, the minute amount and volume of material needed for sample preparation and the almost lossless conditioning and grid preparation procedure achieved using the cryoWriter, make it possible to study the protein complexes of individual cells. Together, the miniaturized immuno-precipitation method and the cryoWriter lay the foundation of a new proteomics method called "single cell visual proteomics", as we recently demonstrated for heat-shock experiments [Giss *et al.* 2014]. Data analysis algorithms geared to the analysis of "visual proteomics" images are currently being tested.

Acknowledgments

The authors would like to thank the workshop of the Biozentrum of the University Basel for their support, S. A. Müller for critical discussions and for carefully reading the manuscript, A. Fecteau-LeFebvre for technical assistance with EM, Ricardo Adaixo, Frank Lehmann for membrane protein test samples (all from the C-CINA, Biozentrum, University of Basel) and A. Engel, emeritus University Basel for his inspiring conversations. Test samples were kindly provided by P. Ringler, M.-A. Mahi, and T. Schwede (Biozentrum, University of Basel), P. Leiman (Laboratory of Structural Biology and Biophysics, EPFL) and R. Diaz- Avalos (New York Structural Biology Center, USA). The project was supported by the Swiss Nanoscience Institute (SNI, project P1401, ARGOVIA project MiPIS) and the Swiss National Science Foundation (SNF, project 200021_162521).

Disclosures

The authors Stefan A. Arnold, Henning Stahlberg and Thomas Braun declare the following competing financial interest: The cryoWriter concept is part of patent application PCT/ EP2015/065398 and EP16194230.

3. The *climateJet* - A New Tool for Grid Preparation for High-Resolution Cryogenic Electron Microscopy

This section presents the *climateJet*, a new addition to the *cryoWriter* setup. It allows the control of the microclimate around the grid and offers the possibility to add additives during sample preparation, thus manipulating the sample and the air-water interface before freezing. The latter aims at preserving the proteins by covering the sample surface with injected surfactants.

My contribution was the development, implementation and testing of the software and the hardware. Execution of all shown experiments. Acquisition and processing of the data. Writing the manuscript and creating the figures.

The following section is planned for submission

The *climateJet* - A New Tool for Grid Preparation for High-Resolution Cryogenic Electron Microscopy

Luca Rima[1], Paolo Oliva[1,2], Ricardo Righetto[1], Henning Stahlberg[1] and Thomas Braun[1]

1 - Center for Cellular Imaging and NanoAnalytics, Biozentrum, University Basel, Switzerland
2 - Swiss Nanoscience Institute, University of Basel, Switzerland

Contents

3.1. Introduction **56**
3.2. Experimental Section **57**
3.3. Results **59**
3.4. Discussion **65**
3.5. Conclusion **65**

Abstract

In recent years, technological progress has made cryogenic electron microscopy (cryo-EM) one of the leading methods for solving protein structures. However, sample preparation has remained virtually unchanged over the last decades. Therefore, sample preparation remained a bottleneck in the cryo-EM workflow. The main problem for the classical cryo-EM sample preparations is the harsh preparation methods using paper blotting and exposing the sample for a long time to the harmful air-water interface. Furthermore, the procedure is wasteful, and 99.99 % of the sample is lost. We recently presented a microfluidic method for cryo-EM grid preparation, which eliminates the paper blotting, and only needs some few nL of the sample in total. Here we present a new addition to the cryoWriter method: a climate jet, which allows (i) the control of the temperature during sample preparation, (ii) the reduction of oxygen from the sample's environment, (iii) the injection of modulators in the gas-stream. Therefore, the *climateJet* creates a microclimate around the grid and enables the modulation of the air-water interface. The latter allows us to tune the air-water interface to protect the proteins from this harsh environment and optimize the particle orientation for the single-particle analysis approach.

3.1. Introduction

The structural characterization of biological macromolecules is crucial for comprehending their function, understanding complex biological processes, and is important for drug development. One prevalent technique currently in use to solve the structure of proteins is cryogenic electron microscopy (cryo-EM). Since the beginning of its development in the 1970s and 1980s [Taylor & Glaeser 1974, Lepault *et al.* 1983, Dubochet *et al.* 1988], the technology has made enormous progress regarding electron microscopes, image acquisition, and processing [Lyumkis 2019]. Today, some structures were determined with resolutions better than 1.5 Å by the single-particle analysis approach, providing "true" atomic resolution [Nakane *et al.* 2020, Yip *et al.* 2020].

Unfortunately, cryo-EM sample preparation has remained virtually unchanged over the last thirty years and is currently considered the workflow's bottleneck. For specimen preparation, a thin sample-film is constituted in a holey carbon layer for subsequent rapid vitrification by plunging the specimen into a cryogen, such as liquefied ethane. The classical preparation approach has several drawbacks: First, about 3 µL of the sample with a protein concentration of $>1\,\mathrm{mg\,mL^{-1}}$ is required. Second, more than 99.99 % of the sample is lost during the extensive and harsh paper blotting step used to create a thin-film in the carbon layers' holes. Third, the whole process from paper-blotting to the vitrification is slow (≈2.5 s). During this time, the proteins often denature at the harmful air-water interface. Taken together, the

classical procedure is not only wasteful but also very harsh for the proteins [Glaeser *et al.* 2016]. Therefore, extensive research was performed during recent years to improve sample preparation. Among others, sample preparation was amended for high-throughput applications [Jain *et al.* 2012], to minimize sample consumption [Jain *et al.* 2012, Dandey *et al.* 2018, Ashtiani *et al.* 2018, Ravelli *et al.* 2020], or to allow time-resolved microscopy [Berriman & Unwin 1994, White *et al.* 2003, Lu *et al.* 2009, Lu *et al.* 2014, Chen *et al.* 2015, Feng *et al.* 2017, Kontziampasis *et al.* 2019].

We developed a microfluidic sample preparation method for, (i) minimizing the sample consumption to a few nL, (ii) entirely avoiding the harmful paper-blotting step, and, (iii) using less than 700 ms preparation time [Arnold *et al.* 2016, Arnold *et al.* 2017, Rima *et al.* 2018]. The volume of a 100 nm thin film on a 3 mm wide grid is only ∼700 pL. This allows the combination of the *cryo Writer* method with other microfluidic modules, such a single-cell picker [Kemmerling *et al.* 2013], or a microfluidic platform for protein isolation [Schmidli *et al.* 2019]. Despite these advantages, this method is not yet perfect. The *cryo Writer* lacks a precise control of the grid environment, making it susceptible to variations in temperature and relative humidity of the room in which the instrument is located. Furthermore, the exposure of the proteins to the air-water interface is minimized, but not avoided. A new module called the *climateJet* was added to the existing setup to address these two problems. It enables creating a microclimate around the grid and offers the possibility to add additives during the grid preparation process. This new extension now allows much better control of the preparation process itself and opens new ways in grid preparation by adding substances that cover the air-water interface or react with a target protein in the short moment before vitrification.

3.2. Experimental Section

ClimateJet

The *climateJet* is a new module of the *cryo Writer* setup. It allows the creation of a microclimate around the grid and the injection of additives during grid preparation. A module overview can be seen in Figure 3.1a. The desired microclimate is created by mixing a dry gas stream with a humid gas stream using two mass flow controllers (GSC-B9SA-FF23, Vögtlin Instruments, Switzerland). For these experiments, dry nitrogen from our in house network was used. The gas was humidified using a tube humidifier (MH-110-24S-2, Perma Pure, USA) to a relative humidity (RH) close to 100 %. The humidifier's temperature was kept constant using a resistor wire (RD 100/0,3, Block, Germany) in combination with a Labview controlled power supply unit (320-KA3005P, RND, Switzerland). The temperature of the stream is adjusted using a Peltier controller (TC2812, Cooltronic, Switzerland) connected to a Peltier

element (TSP-CP14-127-045L, Laird, USA) in contact with a heat sink (ICK PGA 20 X 20, Fischer Elektronik, Germany), which is placed inside the stream of gas. This configuration allows a temperature change of about 10 °C. To achieve even lower or higher temperatures, more temperature control units can be installed in series. An outlet 3D printed in PETG (Prusament, Prusa Research, Czech Republic) directs the stream towards the grid, as shown in Figure 3.1b. A small wedge was milled into the stage so that gas flows around the grid from both sides. A temperature (DM-507, Farnell, UK) and a humidity (HIH-4000, Honeywell, USA) sensor inside the outlet monitor the gas stream. A capillary (TSP-250350, BGB Analytik, Switzerland) is placed at the outlet's constriction side to inject additives into the stream from where they travel as an aerosol towards the grid. The additives are pumped by a high-precision syringe pump (Nemesys, Cetoni, Germany). For testing and benchmarking, an octyl glucoside (OG) solution at its critical micelle concentration (CMC) was injected. A complete list of the parts and the main control graphical user interface (GUI) are shown in Supplementary Information A and Supplementary Information C. The whole *cryoWriter* setup is controlled and monitored using LabView 2017.

Grid and Sample Preparation

The grids (R 2/2, Quantifoil, Germany) were glow discharged (Air, 45 s, 100 W, 0.4 mbar) and prepared in the *cryoWriter* setup as previously described [Rima *et al.* 2018]. The exact openBEB macro for these experiments can be found in the Supplementary Information D. The injection of OG into the stream of gas starts simultaneously with the excess sample's withdrawal and takes 0.6 s. The amount of the injected material was altered for different grids. The grid temperature was held constant at 26.5 °C. The flow of nitrogen was optimized for rapid plunge freezing and had a flow rate of $6\,\mathrm{L\,min^{-1}}$, a relative humidity of 30 %, and a temperature of ~20 °C. Under these conditions, the time from thinning the sample until vitrification is ~700 ms. The grids from the FEI Vitrobot Mark IV were prepared at a set relative humidity of 100 % with a blotting time of 2.5 s and a blotting force of 1. The sample (Chaperonin 60 from *E. coli*, Sigma, Switzerland) had a concentration of $0.4\,\mathrm{mg\,mL^{-1}}$ in Tris buffer (35 mM Tris, 7 mM KCl, 7 mM $MgCl_2$, pH 7.5).

Data Acquisition and Processing

Data was acquired on a FEI Talos (200 kV, FEG, Ceta CMOS) using SerialEM (v3.8.0 beta) with a pixel size of 2.03 Å, a dose-rate of $\sim 25\,\mathrm{e^-\,Å^{-2}\,s^{-1}}$ and an image acquisition time of 2 s. Particle picking and 3D reconstruction were done with cryoSPARC (v2.15.0) using a customized workflow with as little manual interaction as possible to generate unbiased data. The output files from cryoSPARC were converted

into star-files using UCSF pyem (v0.3) [Asarnow *et al.* 2019]. The evaluation of the data was performed in cryoEF (v1.1.0) [Naydenova & Russo 2017], which provides a single metric to assess the particle distribution of a dataset called the efficiency score. This efficiency score is 1.0 for a dataset with a perfect particle orientation distribution, which translates into a perfectly round point spread function (PSF) and decreases as datasets exhibit missing angles or preferred orientations. More details about data acquisition and processing are given in the Supplementary Information B.

3.3. Results

Implementation of the climateJet

The *climateJet* for the *cryoWriter* setup allows controlling the environment's temperature and relative humidity above and below the EM-grid. Furthermore, a small nozzle entry allows the vaporization of surface modulators into the gas-stream. The *climateJet* consists of two main parts: The first part is the stream-conditioner, creating a well-defined gas stream controlling the stream's parameters: the velocity, the relative humidity, and the temperature (Figure 3.1 i-iv). The second part is the outlet focusing the gas-stream towards the EM-grid (Figure 3.1 v) and enabling the vaporization of modulators.

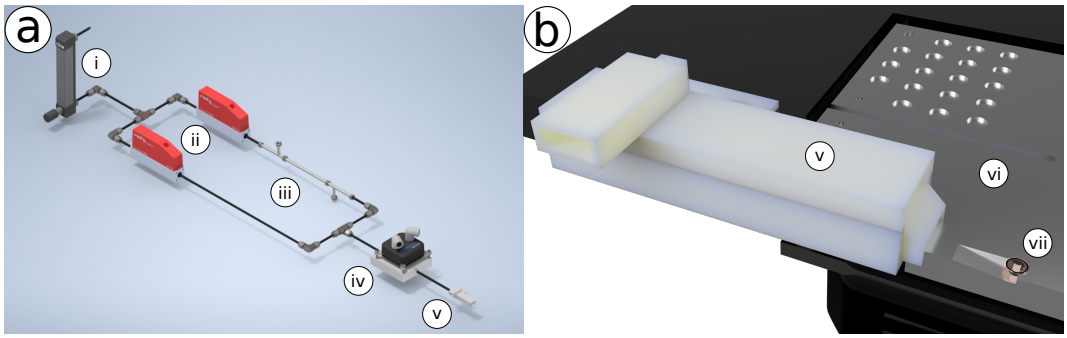

Figure 3.1: (a) Schematic overview of the *climateJet* module. Gas enters the system through a regulator with an attached filter **(i)**. Two mass flow controllers **(ii)** regulate the two gas flows. A humidifier tube **(iii)** humidifies one part of the gas stream. Humidified gas streams through a temperature control unit **(iv)**. An outlet **(v)** shapes the beam of gas and directs it towards the grid position. **(b)** Magnigication of the outlet. In the setup the outlet is placed next to the temperature controlled stage and is pointing towards the grid position. **(v)** Outlet, **(vi)** Temperature controlled stage, **(vii)** Grid position. Note that the grid makes contact with the temperature controlled stage and is positioned on top of the milled wedge.

The stream-conditioner mixes a dry and humidified gas-stream to achieve a desired relative humidity in the outlet. The temperature-control unit consists of a water-cooled Peltier element, and a heat exchange block for efficient temperature control of the gas-stream (Figure 3.1 iv). The sensors for the humidity and temperature control are placed in the entrance chamber of the outlet (Figure 3.2a). A microcapillary allows the injection of modulaters at a restriction site into the gas-flow. This enables an effective dispersion of the additives and a homogeneous mixing in the second chamber. Simulations of the streamline and velocity cross-section confirm the mixing in the outlet, and also show, that the gas-stream flows on both sides of the EM-grid (Figure 3.2a). The latter is corroborated by a simple experiment: if the stage exhibits a temperature below the dew-point, moisture from the environment condensates on the stage-surface. However, using a dry gas-stream from the *climateJet*, keeps the area of the grid free from condensation droplets (Figure 3.2b). Note that the gas mixer and the temperature controller are PID-regulated and that a control software was developed in the openBEB framework [Ramakrishnan *et al.* 2014], allowing the control of the *climateJet* by macros or a graphical user interface (see Figure S1 & Supplementary Information D).

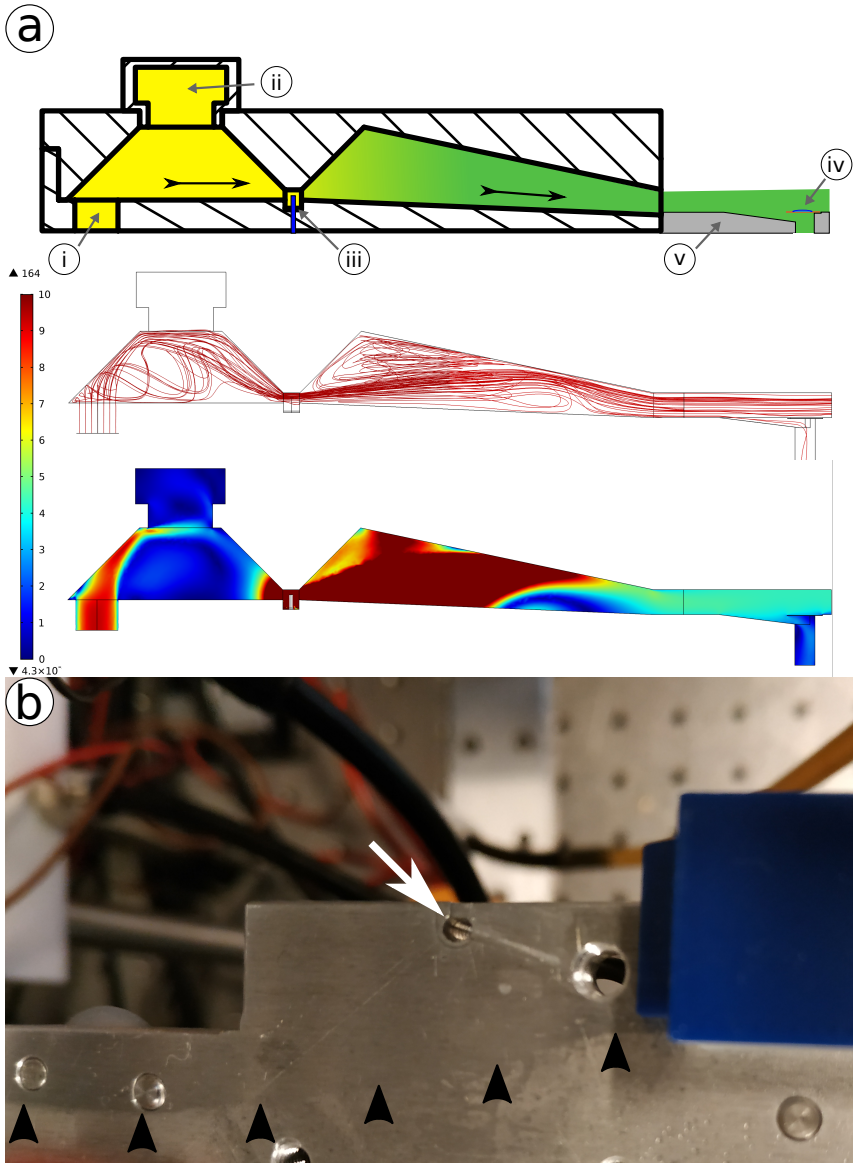

Figure 3.2: Gas flow characteristics of the outlet **(a)** Schematic, streamline and velocity cross section of the outlet. The simulation was performed in COMSOL Multiphysics (v.5.4). **(i)** Gas inlet, **(ii)** Sensor position, **(iii)** Constriction with the capillary (blue) for injection, **(iv)** Grid position, **(v)** Temperature controlled stage. Streamlines for 35 different nitrogen molecules are shown in red. Note that the stream of gas is almost laminar in the region of the grid and is passing it on both sides. The velocity is given in $\mathrm{m\,s^{-1}}$. It is moderate around the grid and high at the point of injection to enable effective dispersion of the additives. **(b)** The sphere of action of the *climateJet* made visible by blowing dry nitrogen over a foggy stage. Black arrows mark the border of the stream of gas. The white arrow indicates the position of the grid. Note that it is completely within the microclimate area. The outlet (blue) can partly be seen on the right side of the image.

Injection

For initial tests of the modulator injection in the gas-stream of the *climateJet*, we used aqueous solutions of octyl glucoside (OG). During the experiment, pure water was vitrified with and without any injection. While it is quite difficult to get thin films of vitreous pure water, it was present on a few squares of some grids (Figure 3.3a). While injecting OG, more ice was found on the grids, and the ice started to exhibit impurities, which presumably are OG micelles (Figure 3.3b). The size characterization of those impurities cannot prove that they are OG micelles due to their small size of ~1 nm-2 nm.

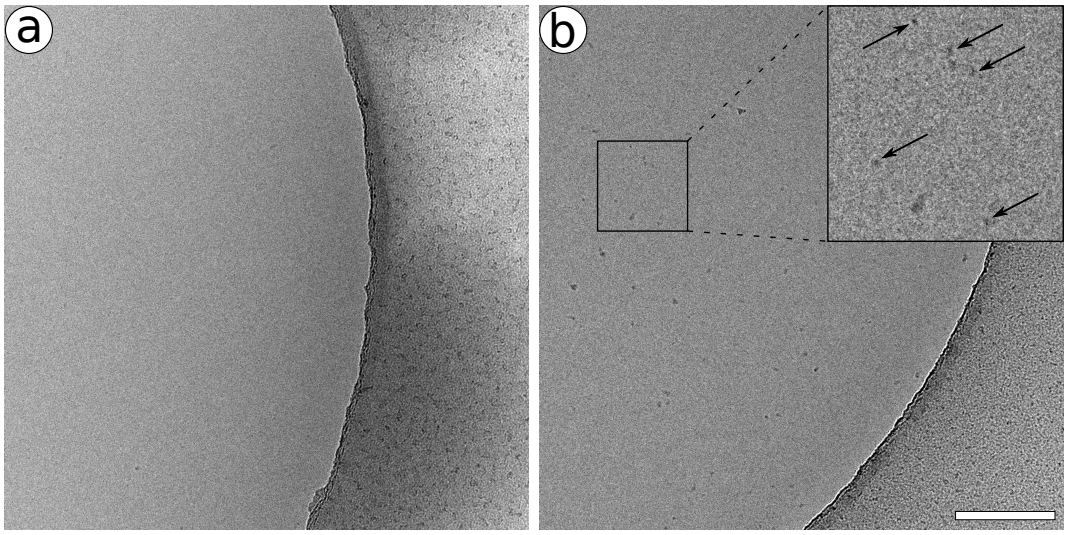

Figure 3.3: Comparison of vitreous ice with and without injection of OG by the *climateJet*. **(a)** Pure vitrified water without injection of OG. **(b)** Pure vitrified water with 150 nL OG injected during the thinning process. Note the presumable OG micelles in the ice. The inset shows an enlarged view of the indicated area with arrows pointing some micelles. Scale bar: 200 nm.

Particle Orientation Analysis

In order to benchmark the *cryoWriter* setup and the *climateJet*, grids with an injection of OG as well as grids without injection were produced and analyzed. For a comparison with classical grid preparation, the same sample was also prepared using an FEI Vitrobot. Another sample to compare classical grid preparation with the *cryoWriter* setup was a Type I ABC transporter (unpublished) from an ongoing project in our lab, which exhibits strong preferred orientation. The data collection of this sample in an FEI Polara (300 kV, FEG, Gatan K2) and the processing in

cryoSPARC was done independently from the other sample.

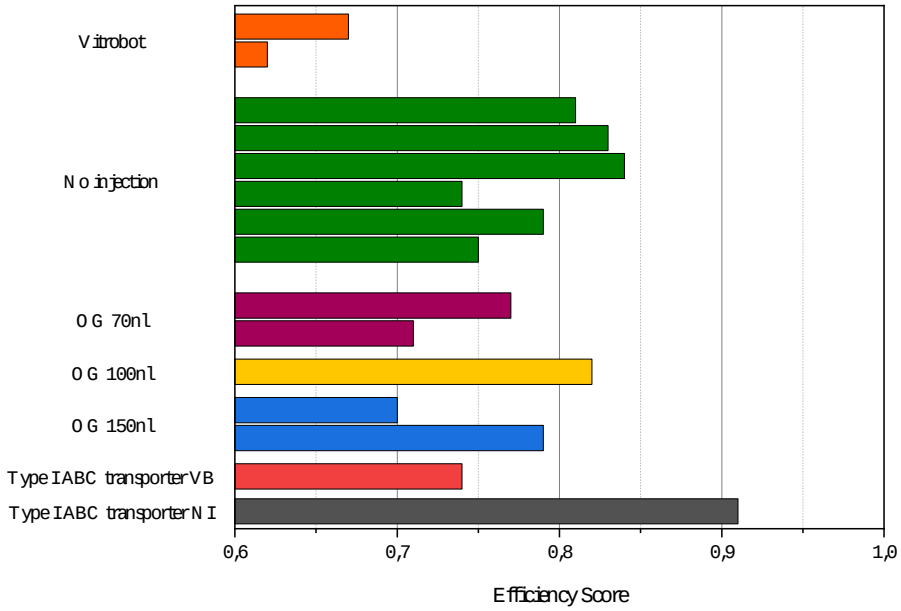

Efficiency Scores	
Vitrobot #1	0.62
Vitrobot #2	0.67
No injection #1	0.75
No injection #2	0.79
No injection #3	0.74
No injection #4	0.84
No injection #5	0.83
No injection #6	0.81
OG 75 nL #1	0.71
OG 75 nL #2	0.77
OG 100 nL #1	0.82
OG 150 nL #1	0.79
OG 150 nL #2	0.7
Type I ABC transporter - Vitrobot	0.74
Type I ABC transporter - No Injection	0.91

Figure 3.4: Efficiency scores of different grid preparations. Grids with the Chaperonin 60 sample were produced using the Vitrobot (VB) as well as the *cryoWriter* setup. For the grids with OG injection the amount of injected OG is given in nanoliter. No injection refers to grids from the *climateJet* using only nitrogen gas without any additives. Two more grids using a Type I ABC transporter sample to compare the two systems are given as well.

From the efficiency scores acquired for the different grid preparations, two observations can be made. First, *cryoWriter* grids have a constantly higher efficiency than grids prepared with the Vitrobot. Second, OG injection has no noticeable effect on the orientation distribution. The much better efficiency score from the *cryoWriter* setup compared to the Vitrobot is present for both samples. The best efficiency score from a Vitrobot grid with the Chaperonin 60 sample is still worse than the lowest one from the *cryoWriter* setup. On the other hand, with an average efficiency score of 0.79 compared to 0.76, there is no significant difference between grids with and without injection of OG. An effect of the OG injection can be observed for the ice formation. As in the first experiment with pure water, there tended to be more ice using OG. For the Chaperonin 60 sample, there is also a difference in the ice's quality, as can be seen in Figure 3.5 a & b. The ice appears less noisy when OG is injected during the thinning process. This is possibly related to film stabilization and reduced evaporation. Comparing grids from the *cryoWriter* setup with grids from the Vitrobot, it is obvious that they exhibit a much higher particle density. This coincides with experiences from other experiments. The higher density is probably due to the fact that the *cryoWriter* setup has no filter blotting step like the Vitrobot. This filter blotting has long been suspected of removing not only more than 99.99 % of the sample volume, but even more protein due to additional adsorption on the filter paper. The argument that the higher density is due to higher evaporation is unlikely, at least for the OG grids, since this would also lead to higher salt concentrations and correspondingly more background noise in the images, but this can not be observed.

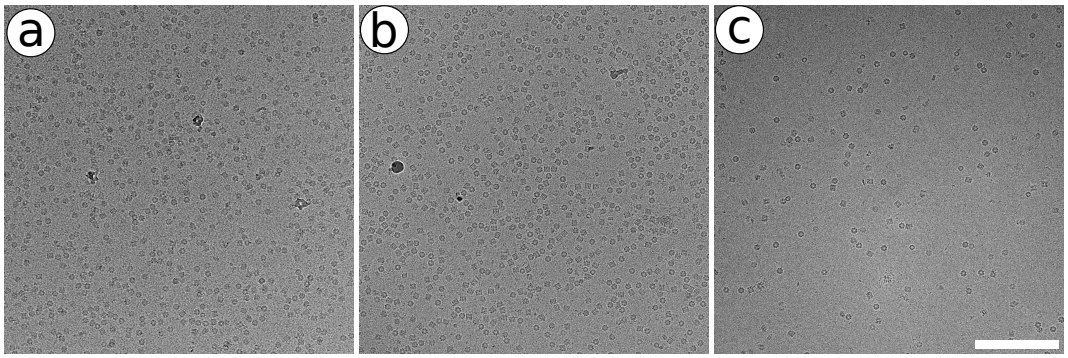

Figure 3.5: Comparison of the ice and the particle density from three different grid preparations. **(a)** *cryoWriter* setup without injection, **(b)** *cryoWriter* setup with 150 nL OG injected during thinning, **(c)** Vitrobot. Scale bar: 200 nm.

3.4. Discussion

The function of the *climateJet* to generate a microclimate around the grid preparation area and the possibility to transfer surfactants to the grid using the stream of gas has been successfully demonstrated. This opens up many new possibilities for optimizing and modifying the grid preparation for high-resolution cryo-EM. For instance, such surfactants could be used to cover the air-water interface and thus protect the proteins from it. Their properties may also be useful to improve the spreading of the sample and to stabilize thin aqueous films by reducing thickness fluctuations. The next logical steps in the evaluation of this system will be to systematically check new additives, e.g., by using a series of amphiphilic compounds which have the same hydrophilic group but differ in the lipophilic part or vice versa, to use different gases, e.g., argon and to inject other compounds, like protein-ligands, a short moment before vitrification. This may lead to new sample preparation methods and allow a variety of novel experiments to be performed. The versatile possibilities of this new system are, at the same time, its greatest weakness. To check if a new approach has the desired effect, samples always have to be checked in an electron microscope. While the grid preparation is quite fast and rather cheap, microscopy is not. The screening time on a microscope is the bottleneck in the proper evaluation of the system. Therefore it might be more promising in the short term to prepare a single but important and difficult protein to demonstrate the benefits of the new system. In this way, the protection of the protein from the air-water interface and the improvement of the particle orientation distribution could be demonstrated within a short time but still with a high impact on the whole field. Such a success would give the whole project an extreme boost for the future and motivate more people to use this system's new possibilities for themselves.

3.5. Conclusion

The *cryoWriter* setup together with its new addition the *climateJet* is a powerful tool for sample preparation for high-resolution electron microscopy. The unique combination of low sample consumption, filter blotting free preparation, fast processing, integrated sample purification, cell lysis ability and the possibility to add additives during grid preparation opens up many new opportunities and, therefore, may develop into a new standard for cryo-EM.

Acknowledgements

Thanks to the workshop of the Biozentrum of the University of Basel for the production of several parts, to M. Chami, K. Goldie and L. Kovacik for technical assistance,

to I. Mohammed for processing assistance and to D. Ni for processing assistance and providing his datasets for analysis. **Funding:** SNF 200021_162521 & 200020_192190 **Author contributions:** L. R. developed, implemented and tested the hardware, executed all experiments, acquired the data and did the processing. L. R. and P. O. programmed the software. L. R. and R. R. developed the processing workflow. H. S. provided knowledge and support in electron microscopy. T. B. planned and devised the project. L. R. has written the manuscript, with backing from T. B. **Competing interests:** The *cryoWriter* belongs to the patent application PCT/EP2015/065398.

Supplementary Information

A. Materials list

Table S1: Materials list of the *climateJet*.

Part Name	**Part Number**	**Distributor**
Water pump	2449120	Digitec Galaxus AG
Tubing	1025U06	Parker Hannifin
Fittings	3106 06 00	Bachofen AG
Fittings	3104 06 00	Bachofen AG
Syringe pump controller	A3921000093	Cetoni
Syringe pump dosing unit	A3921000095	Cetoni
Syringe	1705 LT	BGB Analytik AG
Liquid handling nozzle	FS360-150-30-N-5-C12	MS Wil GmbH
PressFit connector	2525LD	BGB Analytik AG
Heatsink	ICK PGA 20 X 20	Distrelec
Temperature control unit Teflon	Custom	Workshop Biozentrum
Humidity sensor	HIH-4000-002	Distrelec
Temperature sensor	DM-507	Farnell
Humidifier	MH-110-24S-2	Müller AG
Mass flow controller	GSC-B9SA-FF23	Contrec AG
Regulator	SRH3000-01	SMC Pneumatics
Power supply unit	RND 320-KA3005P	Distrelec
Resistor wire	RD 100/0,3	Distrelec
Microcapillary	TSP-250350	BGB Analytik
Peltier element	TSP-CP14,127,045L	Distrelec
Peltier controller	TC2812 RS232	Distrelec
Printing filament	PRM-PETG-1000	Prusa Research

B. Data Collection and Image Processing Parameters

Data collection parameters are given in Table S2, the cryoSPARC workflow and the most important parameters are presented in Table S3 and Table S4. The input parameters for cryoEF are provided in Table S5.

Table S2: Data collection parameters.

Data collection	
Voltage	200 kV
Physical pixel size	2.03 Å
Defocus range	−3.5 µm to −4.5 µm
CETA operating mode	4K
Total dose	50 e^{-} $Å^{-2}$
Number of micrographs	101 – 340

Table S3: Image processing workflow in cryoSPARC. If no values are given, the default values were used. To pick as many particles as possible for a reliable assessment of the orientation distribution later on, an extreme overpicking was performed, followed by one single round of 2D classification where only obvious junk was sorted out. To avoid biasing the data by several rounds of 2D classification, the particles for the final reconstruction were selected by two rounds of ab-initio reconstructions. Like this the program is filtering the particles. The choice of the best class after an ab-initio reconstruction is easy for the operator and therefore unbiased. This protocol could be applied to all datasets without any further changes which allows a fair comparison.

cryoSPARC workflow	
1) CTFFIND4	
2) Template Picker	Particle diameter: 160 Å
3) Inspect Picks	NCC score > 0.400
4) Extract from Micrographs	
5) 2D Classification	
6) Select 2D classes	Keep everything except obvious junk
7) Ab-Initio Reconstruction #1	Number of Ab-Initio classes: 5
	Maximum resolution: 10 Å
	Class similarity: 0
	Keep best class
8) Ab-Initio Reconstruction #2	Number of Ab-Initio classes: 2
	Maximum resolution: 10 Å
	Keep better class
9) Ab-Initio Reconstruction #3	Maximum resolution: 10 Å
10) Homogeneous Refinement (new)	

Table S4: Other processing parameters and values.

Image processing	
Micrographs	101 – 340
Box size	256 pixel
Particles for 3D refinement	10,816 – 64,273
Symmetry	C1
GSFSC Resolution (auto tightening)	8.18 Å – 12.58 Å

Table S5: Input parameters for cryoEF used to calculate the efficiency score.

Input parameters for cryoEF	
Box size	400 pixel
Symmetry	C1
Diameter	160 Å
Subset size	4000

C. Graphical User Interface

The main GUI of the *climateJet* module concentrates the most important readings and controls and allows easy handling during the experiment. More advanced settings are available and can be accessed by the different tabs in the GUI.

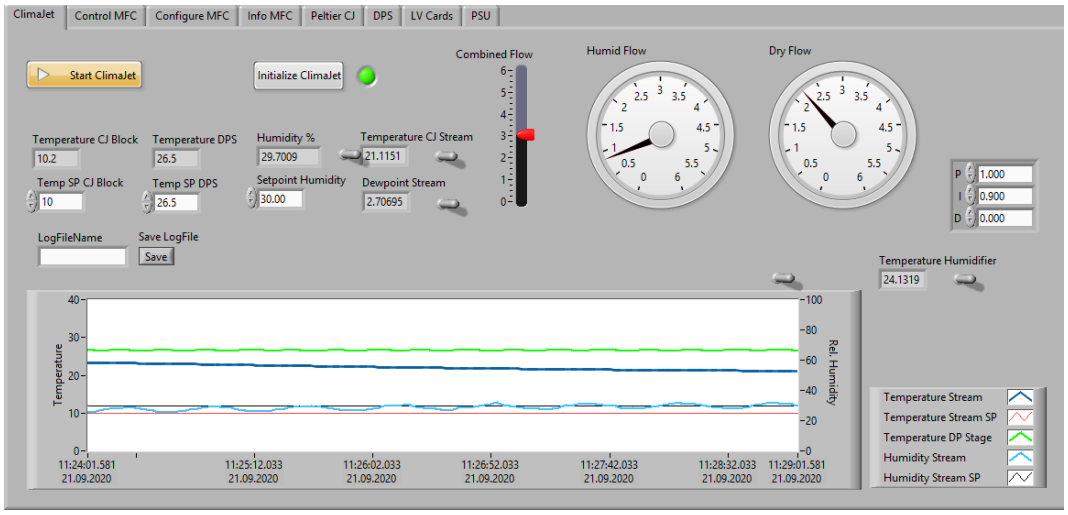

Figure S1: The main GUI of the *climateJet* module allows controlling and monitoring of the stream of gas which generates the microclimate around the grid.

D. Macro

The macro for the grid preparation in the *cryoWriter* setup can be seen below. It is an extended, improved and optimized version of a macro from Dr. Stefan Arnold. For more information about the openBEB language and the sub-macros used in this macro see [Ramakrishnan *et al.* 2014] and [Arnold 2017].

```
1  #Ask user if ready to start; Deactivate timeout for zero delay plunge freezing
2  !ask::"Grid" and "Sample" positions defined?::Yes, proceed::No, cancel::Answer
3  !if::Answer::=::Yes, proceed
4  .!tellmodule::scl.ttl
5  ..ChangeTimeout::-1
6  #Pick up sample
7  .!include::Nemesys::unit=1::flowrate=1::volume=0.005::direction=0::NemesysPause=100
8  .!include::Stage2::position=Sample
9  .!include::Nemesys::unit=1::flowrate=1::volume=0.045::direction=1::NemesysPause=100
10 .!include::Nemesys::unit=1::flowrate=1::volume=0.005::direction=0::NemesysPause=100
11 #Go to EM grid, deposit 20 nl, make spiral pattern
12 .!include::Stage2::position=Grid
13 .!tellmodule::SCL.nemesys
14 ..MacroDosing::1::0.4::0.02::0 #DosingUnit::FlowRate::TargetVolume::Infuse(0) or Withdraw(1)
15 .!include::PatternNew::steps=3::xrange=175::yrange=175::patternspeed=SMS 100::pattern=spiral
16 .!include::StageLow::position=Grid::travelheight=mr0
17 .!include::MercRel::distance=-10
18 #Infuse additives into climateJet while re-aspirating excess sample
19 .!tellmodule::SCL.nemesys
20 ..MacroDosing::2::15::0.15::0 #DosingUnit::FlowRate::TargetVolume::Infuse(0) or Withdraw(1)
21 .!include::Nemesys::unit=1::flowrate=4.5::volume=0.045::direction=1::NemesysPause=0
22 #Switch off magnet to initiate plunge freezing
23 .!tellmodule::scl.ttl
24 ..Magnet::macro::OFF::360 #Magnet::macro::ONorOFF::delay(ms)
25 #Reset system and ask user if log data should be saved
26 .!tellmodule::SCL.Stage
27 ..MercGoHomeZ
28 ..getStatus
29 .!tellmodule::SCL.CJandDPS
30 ..SaveData
31 .!tellmodule::SCL.Stage
32 ..GoHomeSecY
33 ..GetStatusY
34 .!tellmodule::SCL.Stage
35 ..MercGoHomeX
36 ..getStatus2
37 ..!waitmodule
38 .!tellmodule::scl.ttl
39 ..ChangeTimeout::200
40 ..Magnet::macro::ON::0 #Magnet::macro::ONorOFF::delay(ms)
41 !ask::Do you want to save the log file?::Yes::No::LogAnswer
42 !if::LogAnswer::=::Yes
43 .!input::Filename::logfilename
44 .!tellmodule::SCL.CJandDPS
45 ..WriteDataToFile::macro::logfilename
```

Macro S1.: Macro for grid preparation in the *cryoWriter* setup. Functions are explained after the number signs. For the preparation of grids without injection of additives lines 19 & 20 are not executed.

4. Microfluidic Sample Purification for Transmission Electron Microscopy Using Magnetic Microspheres

In the following section the magnetic trap, a new module of the *cryoWriter* setup, is introduced. This new addition enables the isolation of proteins from minute starting volumes using magnetic particles. The proteins can subsequently be prepared for TEM analysis.

My contribution to the following publication was implementing the magnetic trap and new linear stages into the existing *cryoWriter* setup, contributing some programming and introducing C. S. operating the setup.

The following section has been published in:

PNAS
Volume 116, Issue 30, July 2019, Pages 15007-15012
https://doi.org/10.1073/pnas.1907214116

Microfluidic protein isolation and sample preparation for high-resolution cryo-EM

Claudio Schmidli[1,2], Stefan Albiez[1], Luca Rima[1], Ricardo Righetto[1], Inayatulla Mohammed[1], Paolo Oliva[1,2], Lubomir Kovacik[1], Henning Stahlberg[1] and Thomas Braun[1]

1 - Center for Cellular Imaging and NanoAnalytics, Biozentrum, University Basel, Switzerland
2 - Swiss Nanoscience Institute, University of Basel, Switzerland

Contents

4.1. Significance Statement **72**
4.2. Introduction **72**
4.3. Results **73**
4.4. Conclusion **78**
4.5. Material and Methods **80**

Abstract

High-resolution structural information is essential to understand protein function. Protein-structure determination needs a considerable amount of protein, which can be challenging to produce, often involving harsh and lengthy procedures. In contrast, the several thousands to a few million protein particles required for structure-determination by cryogenic electron microscopy (cryo-EM) can be provided by miniaturized systems. Here, we present a microfluidic method for the rapid isolation of a target protein and its direct preparation for cryo-EM. Less than 1 µL of cell lysate is required as starting material to solve the atomic structure of the untagged, endogenous *human* 20S proteasome. Our work paves the way for high-throughput structure determination of proteins from minimal amounts of cell lysate and opens new opportunities for the isolation of sensitive, endogenous protein complexes.

4.1. Significance Statement

The recent improvements in cryogenic electron microscopy (cryo-EM) caused a revolution in structural biology. However, (i) protein isolation and (ii) sample preparation methods lag behind, and cryo-EM is performed at far from full efficiency. Here, we present a microfluidic method for the rapid isolation of a target protein from minimal amounts of cell lysate and for its direct preparation for high-resolution cryo-EM.

Our technology opens new avenues for structural biology: high-throughput structure determination of proteins in a multitude of conditions, ultrafast isolation and structure determination of sensitive proteins, and the analysis of proteins that cannot be produced in sufficient amounts using conventional approaches.

4.2. Introduction

Knowledge of a protein's architecture at high resolution is vital to understand its mechanics and chemistry. In recent years, cryogenic electron microscopy (cryo-EM) [Dubochet *et al.* 1988] has matured into a powerful method that can determine the architecture of biological macromolecules at the resolutions required to interpret the atomic fold of proteins [Kuhlbrandt 2014, Cheng 2018]. In the single-particle cryo-EM approach [Frank 1975, Heel & Frank 1981], an unsupported, thin layer of isolated protein complexes in amorphous (vitrified) ice is visualized at close to physiological conditions. Only several thousand to a few million imaged particles are needed to calculate a high-resolution, three-dimensional (3D) structure. Nevertheless, protein production, purification, and sample preparation for cryo-EM are nowadays considered the bottleneck for structure determination [Glaeser 2016, Thompson *et al.* 2016, Stark

& Chari 2015]. We have identified two dominating reasons for this: Firstly, significant amounts of protein must be produced. Conventional sample preparation for cryo-EM requires several microliters of a purified protein solution at a concentration of approx. $1\,\mathrm{mg\,mL^{-1}}$ per grid, from which extensive filter-paper blotting later removes the vast majority of protein particles [Taylor & Glaeser 1976, Dubochet *et al.* 1988, Kemmerling *et al.* 2012, Arnold *et al.* 2018]. Secondly, both, protein purification and cryo-EM sample preparation are lengthy and harsh procedures. Mostly, high-yield expression systems are employed, and one or two chromatographic steps are needed to purify the protein particles. In addition, the classical cryo-EM sample preparation process that follows is a rough procedure [Glaeser *et al.* 2016], primarily because of the blotting step, and many proteins denature.

We recently developed a microfluidic cryo-EM grid preparation system termed *cryo Writer*, allowing the preparation of cryo-EM specimens from nanoliters of sample-solution [Arnold *et al.* 2016, Arnold *et al.* 2017, Rima *et al.* 2018]. Since the *cryo Writer* does not use paper blotting, it ensures that grid preparation is gentle and virtually lossless. Here, we report the combination of sample grid preparation using the *cryo Writer* with microfluidic protein purification [Giss *et al.* 2014], to determine the 3.5 Å cryo-EM structure of the untagged *human* 20S proteasome complex, which is the 'catalytic core' of the ubiquitin-proteasome system involved in 80 % of protein degradation [Bhardwaj *et al.* 2009] and an important drug target [Cromm & Crews 2017].

4.3. Results

The microfluidic toolchain developed (Figure 1a) consists of a module for affinity-isolation of the untagged protein from small quantities of cell lysate, followed by modules to write the purified protein onto a cryo-EM grid and vitrify the sample [Giss *et al.* 2014, Arnold *et al.* 2017, Rima *et al.* 2018]. Briefly, antibody 'fragment antigen binders' (Fabs) are used to recognize and extract untagged target proteins from cell lysate. These Fabs are biotinylated with a photo-cleavable cross-linker, which binds with high affinity to the streptavidin functionalization of super-paramagnetic beads (Figure 1b). First, the cell lysate is incubated with Fabs and super-paramagnetic beads. A <1 µL volume of this solution is then aspirated into the microcapillary of the *cryo Writer* system (Figure 1c). The super-paramagnetic particles are immobilized in a 'magnetic trap,' (see Figure S1) isolating bound Fabs and their target proteins, while other cellular components are washed out. Ultra-violet (UV) light is used to break the photo-cleavable biotin cross-linker and the target proteins with the bound Fabs are eluted [Giss *et al.* 2014]. This procedure results in a 25 nL eluate, which is directly used to prepare one or more cryo-EM grids, while the magnetic particles are retained in the microcapillary.

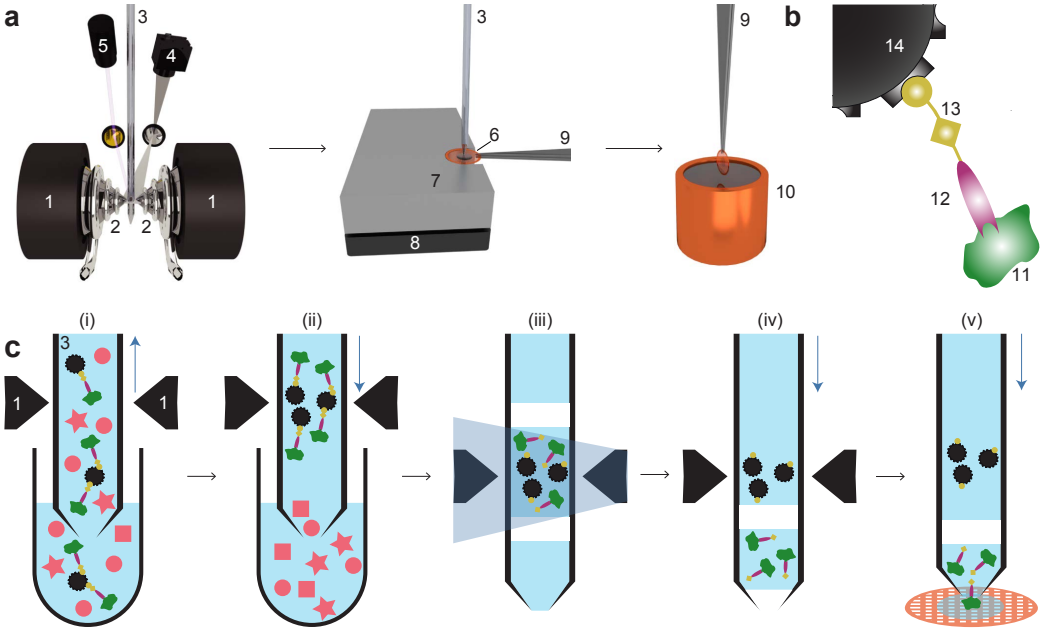

Figure 1: Schematic work-flow for microfluidic protein isolation and cryo-EM grid preparation. **(a)** Hardware for protein-isolation and cryo-EM grid preparation. The electromagnetic trap consists of two electromagnets (1) that produce a strong magnetic field gradient via their water-cooled iron tips (2). Sample processing in the capillary (3) is monitored by a camera (4), and a UV LED (5) allows photo-cleavage (see panel b) of the sample, both via mirrors. After protein isolation, the capillary nozzle is moved above a cryo-EM grid covered with a holey carbon film (6). The cryo-EM grid is positioned on a stage (7) that is temperature controlled by a Peltier element (8) and held with a Peltier-cooled tweezer (9). The isolated protein is directly written onto the grid and plunge-frozen in liquid ethane (10). **(b)** Composite material for 'protein fishing.' The target protein (11) is recognized by a Fab (12) that is covalently modified by a photo-cleavable cross-linker (13). The linker molecule ends with a biotin moiety, which strongly binds to the streptavidin coated bead (14). **(c)** Protein isolation work-flow. (i) Magnetic beads are incubated with biotinylated Fabs and cell lysate to capture the target structures (green). Less than 900 nL of sample is aspirated into the microcapillary for the protein isolation. (ii) The magnetic beads are immobilized in the magnetic trap (1). Non-bound lysate components (red) are flushed out. (iii) Illumination with UV light breaks the cross-linker. Before photoelution, two air bubbles are introduced and serve as boundaries to avoid dilution of the released proteins by diffusion (see Supplementary Figures S1 & S3 for details). (iv) Separation of the capturing magnetic beads and the eluted proteins. (v) The isolated target proteins are directly deposited on a cryo-EM grid for vitrification. The blue vertical arrows indicate the pump direction.

We used Fabs instead of full-length antibodies to avoid the cross-linking and aggregation that occurs when target proteins display more than one epitope. A linear cross-linker with three functional groups is used to connect the Fab to the super-paramagnetic beads. One end of the linker covalently attaches to the Fab while the biotin at the other end binds to the streptavidin-coated bead. A nitrobenzene moiety in between allows photo-cleavage of the linker upon illumination with UV light at 365 nm (Figure 1b). Preparation of Fab fragments from antibodies and biotinylation with the cross-linker took ≈7 h; the biotintilated Fabs could be stored in the dark for several weeks at 4 °C.

The cell lysate was incubated with the Fabs and beads outside of the microcapillary in a 5 µL well. The cytosol/Fab mixture was incubated for 5 h, and then for an additional 1 h together with the super-paramagnetic beads. The use of miniaturized sample wells rather than the microcapillary, allowed several of these time consuming incubations to be carried out in parallel.

After incubation, a volume of 900 nL was aspirated from the well into the microcapillary, which was precisely positioned between the iron tips of the particle trap system. In this setup, the trap is formed by electromagnets with water-cooled (4 °C) iron tips that concentrate the magnetic flux between the opposite poles and generate the field gradients required to trap the super-paramagnetic particles (see also Figure S1). The cooling system prevents heating and denaturation of the sample. A camera and magnifying lens system allow the procedure to be monitored. The 1 µm super-paramagnetic beads employed, can be easily immobilized in the magnetic trap and only marginally scatter photons with 365 nm wavelength, allowing efficient photoelution in 15 min [Giss *et al.* 2014]. Photoelution releases less non-specifically bound protein than the competitive elution typically used in other methods, because it does not change the buffer composition [Giss *et al.* 2013]. Just before elution, the beads were enclosed by two 6 nL air bubbles in a 25 nL buffer-plug, to prevent diffusion and Taylor dispersion [Squires & Quake 2005]. After photoelution, the eluate was separated from the immobilized beads by the pump system and moved towards the apex of the microcapillary.

For cryo-EM specimen preparation, a sample carrier (grid) covered by a holey carbon film was placed on a temperature-controlled stage regulated to a temperature 7 °C above the environmental dew-point. This temperature offset builds a micro-environment on the grid surface, allowing controlled evaporation of the sample liquid. In a first step, 20 nL of the eluate containing the purified protein was written onto the grid, covering an area of ≈0.75 mm^2. Excess sample was re-aspirated into the microcapillary, leaving a thin layer of the protein on the holey carbon film. This

layer was left to settle for ≈50 ms with the grid still on the dew-point stage. The gentle evaporation that occurs during this time stabilizes [Padmakar *et al.* 1999] and thins the sample film. Finally, the written grid was rapidly removed from the stage and plunge-frozen, resulting in a vitrified ice layer [Arnold *et al.* 2017, Rima *et al.* 2018]. In principle, several cryo-EM grids can be written with one 25 nL eluate. Interestingly, when this was done the first cryo-EM grid contained more protein particles than later grids. For the analysis presented here, we only used one cryo-EM grid, and this was the first grid prepared from the eluate. The whole *cryoWriter* process starting from protein isolation and ending with cryo-EM grid preparation could be performed in less than 1 h.

We employed the *cryoWriter* toolchain to isolate endogenous and untagged *human* 20S proteasome from commercially obtained HeLa cell lysate using Fabs generated from an antibody against the α4 subunit of the protein complex. As a positive control for the cryo-EM grid preparation, tobacco mosaic virus (TMV) particles were added to the elution buffer. The cryo-EM grid showed homogeneous ice layers (Figure 2a,b) with the protein embedded in thin, vitreous ice. TMV particles and randomly oriented 20S proteasomes are visible, as well as smaller protein particles that are most probably unbound Fabs.

From only one grid, 523 dose-fractionated image stacks (movies) were recorded, yielding a total of 55 135 particles, which were processed with cryoSPARC v2 (Structura Biotechnology Inc.) [Punjani *et al.* 2017] and RELION 3 [Zivanov *et al.* 2018] for structure determination. Figure 2c shows typical projection class averages obtained from the 20S proteasome. A seven-fold pseudo symmetry is observed in the top view, with weakly visible Fab fragments attached to the two α4 subunits. The side-view exhibits the distinctive stack of α-β-β-α rings. Figure 2d shows a projection class average of TMV. The secondary structure was visible in all projection-averages, demonstrating the excellent quality of the cryo-EM grid.

The 3D reconstruction of the human 20S proteasome shown in Figure 3 has a resolution of 3.5 Å (for details see Figure S4). The structure exhibits the typical dimeric, C2-symmetric arrangement of an α-β and a β-α ring-pair, each ring with a pseudo-7-fold arrangement of the respective subunits. We refined the X-ray structure [Schrader *et al.* 2016] into our density map. The two Fabs against the α4-subunits aided the assignment of the individual components. Figure 3b shows the α and β rings with all 14 models fitting the experimental densities in good agreement (see also Figure 3c,d, and Table S5). The densities of subunits β4, β5 and β6, are less well resolved (see also Figure S5), which can be attributed to their catalytic activity [da Fonseca & Morris 2015]; we assume that the lower resolution reflects the greater flexibility they require to perform their biological function.

The reconstruction of the added TMV particles has a resolution of 1.9 Å (see Fig-

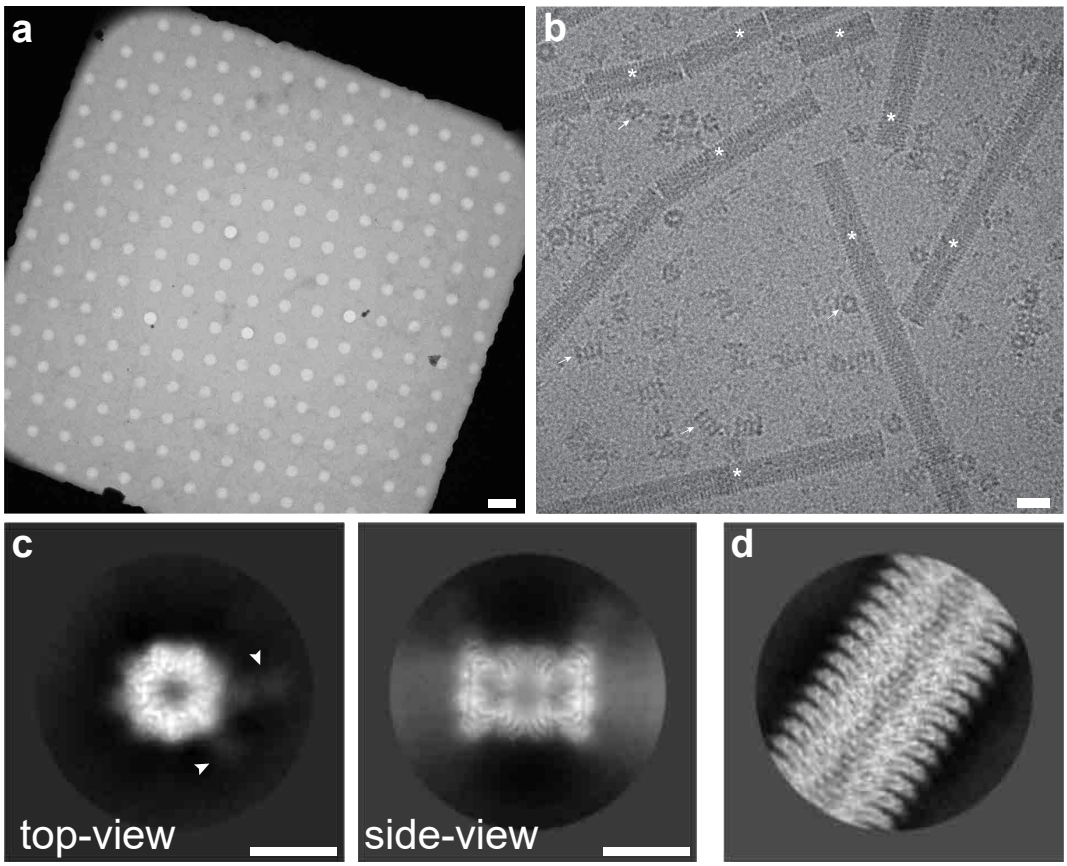

Figure 2: Sample quality and data-collection. **(a)** Overview image of a grid square and the holey carbon film, showing a thin film of vitreous ice. Scale bar: 4 µm. **(b)** High magnification image of the isolated 20S proteasome sample. Arrows indicate 20S proteasome as top and side views; asterisks denote TMV. Furthermore, small particles are visible in the background, most probably unbound Fabs. (Scale bar: 20 nm.) TMV was added to the elution buffer as positive control for the cryo-EM grid quality (see Figure S4). The contrast of the image was increased using a Gaussian blur and subsequent histogram adjustment. **(c)** Selected projection averages of the 20S proteasome. Arrows indicate two bound Fabs recognizing the α4 subunit. (Scale bar: 10 nm.) **(d)** Typical projection average of TMV from the same cryo-EM grid as the 20S proteasome. (Scale bar: 10 nm.)

ures S4 & S7), indicating that the microfluidic sample preparation did not limit the resolution of the *human* 20S proteasome. Unlike the archaeal T20S proteasome, which is often used as a cryo-EM test-sample thanks to its 14-fold D7 symmetry, the *human* 20S proteasome is only two-fold symmetric. The lower symmetry reduces the internal averaging by a factor of 7. Moreover, the similar subunits around the 'pseudo-sevenfold' axis can lead to misalignments of the particle projections. Together, these factors explain why existing cryo-EM maps are at the lower resolution

of 3.5 Å [da Fonseca & Morris 2015, Morris & da Fonseca 2017].

4.4. Conclusion

Several methods have been presented to improve sample preparation for cryo-EM, all having their own specific purpose. Examples include high-throughput grid preparation [Dandey *et al.* 2018, Razinkov *et al.* 2016, Noble *et al.* 2018b], time-resolved EM [Feng *et al.* 2017], and single-cell visual proteomics [Arnold *et al.* 2017, Arnold *et al.* 2016]. Furthermore, antibody-functionalized EM-grids were proposed to 'fish' target proteins [Derrick 1973, Yu *et al.* 2016], and affinity grids designed to capture proteins with engineered his-tags [Kelly *et al.* 2008b]. In both cases, the vitrified protein is supported by a continuous carbon film, which can limit the resolution obtained. Here, we combined microfluidics for protein isolation and purification with cryo-EM grid preparation, resulting in free-standing layers of vitrified protein samples that allow high-resolution cryo-EM.

Microfluidic methods could potentially overcome the current bottleneck in cryo-EM, resulting from the large amount of protein used for sample preparation and the long and harsh conditions used for protein purification. We demonstrated that microfluidics (i) can deliver cryo-EM grids of high quality allowing <2 Å resolution from 20 nL of a sample and (ii) allows the isolation of endogenous proteins from less than 1 µL cell-lysate with subsequent structure determination at 3.5 Å. In addition, the method presented here significantly reduces both the amount of starting material and the time needed for the structural analysis of proteins, avoids harsh protein purification conditions, and eliminates the stringent and wasteful blotting steps otherwise employed on cryo-EM grid preparation.

The high efficiency of cryo-EM combined with the microfluidic approach will allow the structure of proteins that cannot be produced in large quantities to be studied. Up to now, structural studies were only possible if the protein could be over-expressed or produced in a large numbers of cells. The small sample volumes used during the microfluidic purification process allow a high protein concentration to be maintained, which is helpful if protein complexes fall apart upon dilution. Furthermore, the small sample volume also allows for 'buffer conditioning' [Arnold *et al.* 2016], e.g., for the introduction of small ligands before sample vitrification. In addition, further optimization of the purification step and use of the *cryoWriter*, will almost certainly make it possible to perform the whole preparation in less than 1 h, facilitating the investigation of sensitive proteins targets. Finally, the toolchain presented here can also be combined with *in vitro* translation systems, which would enable high-throughput structure determination, or with a single cell lysis device [Kemmerling *et al.* 2013, Arnold *et al.* 2016, Arnold *et al.* 2017], which would bring the structural analysis of proteins originating from a single cell within reach.

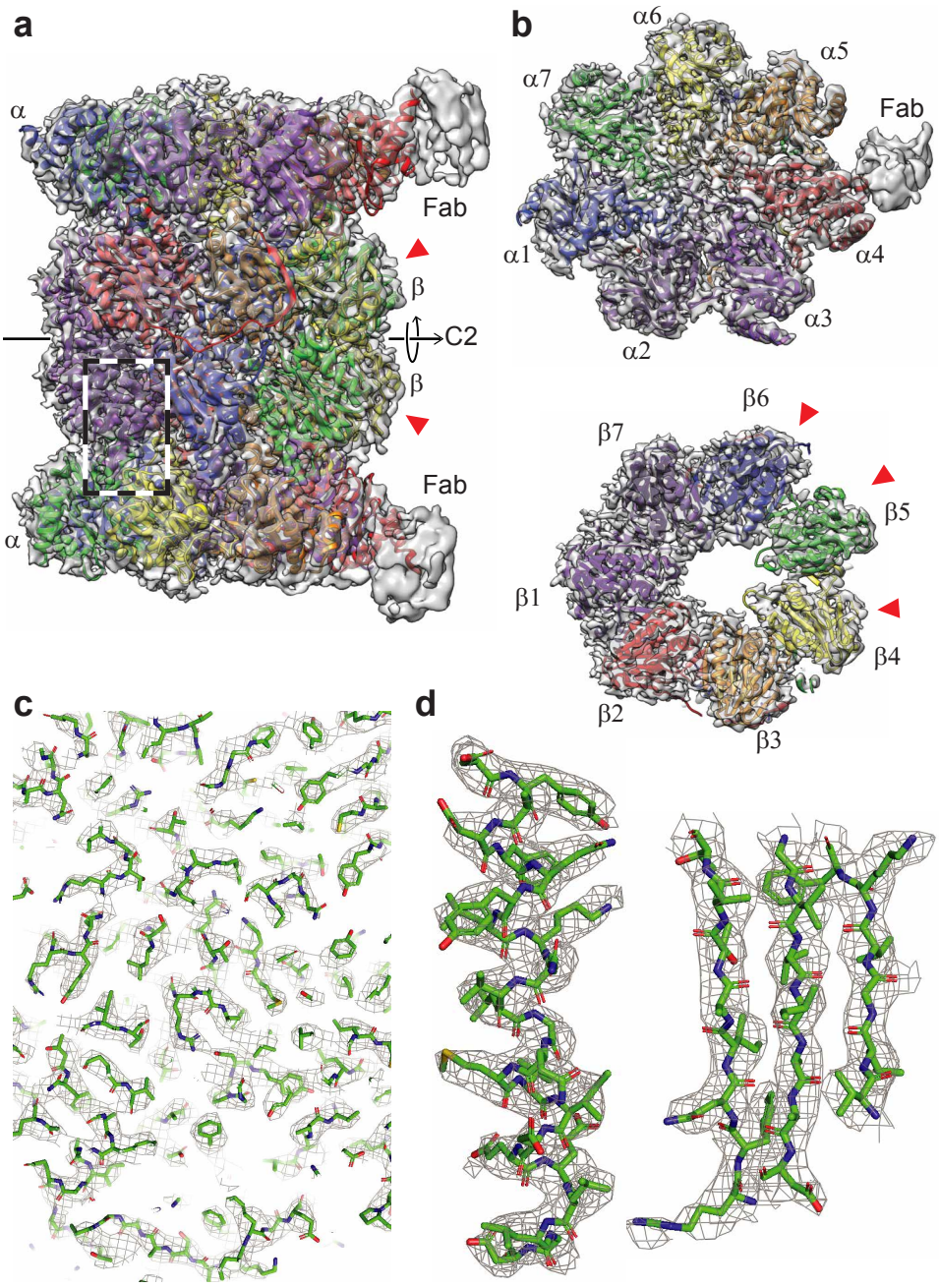

Figure 3: 3D reconstruction of the human 20S proteasome. The red arrowheads indicate the catalytically active subunits. **(a)** Side view showing the two α and two β rings, all 14 subunits are fit into the mass-densities. Parts of the two bound Fabs are visible at lower resolution, due to the high flexibility of the attached Fabs. The C2 symmetry-axis is indicated. **(b)** Top view of an α and a β ring, both have a pseudo 7-fold symmetry. Different subunits are indicated by different colors. **(c)** A zoom into the side-view region indicated by the dashed box in panel a, documenting the quality of the data and model fitting. An enlarged view of one α helix and three strands of a β-sheet are shown in **(d)** as an example.

4.5. Material and Methods

Generation of Fabs

Fabs were generated from an antibody against the α4-subunit of the human 20S proteasome (Enzo Life Sciences, BML-PW8120, Switzerland), using a commercial kit (Thermo Fisher Scientific Inc., # 44685, Switzerland) and following the provided protocol. After generation of Fabs, the buffer was changed to phosphate-buffered saline (PBS, pH 7.4, 150 mM NaCl, 1.5 mM KH_2PO_4, 8.1 mM Na_2HPO_4, 2.6 mM KCl; Sigma, # D8537, Switzerland), and the Fabs were concentrated to a concentration of 0.28 mg mL^{-1} using a centrifugal filter unit (Sigma, # UFC501024, Switzerland).

Biotinylation of Fabs

To biotinylatilate the Fabs, a six-fold molar excess of photo-cleavable NHS-biotin cross-linker (Fisher Scientific, # NC1042-383, USA) was added to the Fabs (0.28 mg mL^{-1}, 5.6 mM) and incubated at room temperature for 1 h. Excess, unbound cross-linker was removed using a spin desalting-column (Thermo Fisher Inc., # 87764, Switzerland) following the instructions from the kit-protocol.

Binding of the 20S Proteasome to Magnetic Particles

To 'fish' the human 20S proteasome, HeLa cell lysate (human origin, Enzo Life Sciences, BML-SW8750, Switzerland) was incubated in the presence of 0.7 mM of biotinylated Fabs at 4 °C for 5 h. Subsequently, super-paramagnetic Dynabeads^{TM} (Thermo Fisher Scientific Inc., # 65602, Switzerland) were added to achieve a final concentration of 5 pM and incubated additionally for 1 h at 4 °C. Glycerol and ATP which maintain proteasome stability were intentionally not added to the buffers to ensure that the regulatory complexes dissociated from the 20S proteasome core complex [Leggett *et al.* 2005].

Extraction and Vitrification of 20S Proteasome

After the incubation step, a 0.3 µL volume of the cell lysate/Fabs/super-paramagnetic beads mixture was aspirated into the microcapillary of the *cryoWriter* setup at a flow rate of 0.4 µL min^{-1}, and passed through the electromagnetic trap (see Supplementary Information A). The beads were retained by the magnetic field gradient to form a bead plug. Subsequently, the flow direction was inverted and the particle plug was

washed with 4 µL washing buffer (25 mM HEPES−KOH, pH 7.5, 5 mM $MgCl_2$) at a flow-rate of 3 µL min^{-1}. The aspiration-wash cycle was repeated twice. In all, a total of 0.9 µL cell lysate was loaded into the microcapillary. At the end, the capillary was washed further with 45 µL of washing buffer at a flow-rate of 3 µL min^{-1}.

Before UV cleavage, the sample plug was enclosed between two 6 nL air bubbles that were introduced from the nozzle tip, and were separated by a volume of 25 nL washing buffer containing 1 mg mL^{-1} of tobacco mosaic virus (TMV). See also Supplementary Information B for more details. TMV was kindly supplied by Ruben Diaz-Avalos, Howard Hughes Medical Institute, USA. The hydrophilicity of the inner surface of the microfluidic capillary retains a thin hydration layer, which allows magnetic beads with loaded samples to remain within the aqueous phase while the air bubbles are introduced. The sample plug was then exposed for 15 min to UV light emitted at a wavelength of 365 nm by a 190 mW UV LED (Thorlabs, # M365L2, Switzerland).

After photo-cleavage, 20 nL of the 25 nL eluate containing the purified protein was primed on a 400-mesh copper grid covered with a holey carbon film (R1.2/1.3, Quantifoil, Germany) that was glow discharged for 45 s in air plasma immediately before use. The cryo-EM grids were prepared as described [Arnold *et al.* 2017], applying *protocol 1*. However, we adjusted the parameters for the sample: the stage temperature was 7 °C above the dew point temperature of the environment, *i.e.*, 10 °C on most days, and the settling time was 50 ms.

Data Acquisition

Cryo-EM image data were collected on a FEI Titan Krios (ThermoFisher Scientific) transmission electron microscope, operated at 300 kV and equipped with a Gatan Quantum-LS imaging energy filter (GIF, 20 eV zero loss energy window; Gatan Inc.). Micrographs were acquired using a K2 Summit direct electron detector (Gatan Inc.) operated in dose fractionation mode (super-resolution 8k, 30 frames, 0.2 s/frames, 6 s total exposure) and controlled by the SerialEM [Mastronarde 2005] software. The physical pixel size was 0.812 Å and the total electron dose was 72 e^- $Å^{-2}$ per recorded image stack (movie). Micrographs were drift-corrected, dose-weighted, and Fourier-cropped to 4k, using MotionCor2 [Zheng *et al.* 2017] via the FOCUS interface [Biyani *et al.* 2017]. Additional data collection parameters are listed in Supplementary Information C.

Image Processing

An initial model for subsequent processing with RELION3 [Zivanov *et al.* 2018] was generated using cryoSPARC v2 (Structura Biotechnology Inc.) [Punjani *et al.* 2017]. Particles were picked in cryoSPARC v2, and then 2D classified. An *ab-initio* model was generated using ≈19 000 particles selected from the best 2D classes, and subsequently refined to 4.1 Å resolution with C2 symmetry imposed.

For RELION3 processing, 55 135 particles were picked with Gautomatch (K. Zhang, www.mrc-lmb.cam.ac.uk/kzhang/) using templates projected from the map obtained using cryoSPARC v2, and low-pass filtered to 20 Å resolution. After 2D classification, 38 848 particles were 3D classified into 4 classes. The best class, containing 16 015 particles was selected for 3D refinement. A generous mask derived from the refined map low-pass filtered to 15 Å and with a soft-edge of 6 voxels was used for postprocessing, yielding a resolution of 4.3 Å. Afterwards, rounds of CTF refinement including defocus refinement per-particle, astigmatism refinement per-micrograph, and beam-tilt refinement per-dataset were iterated with rounds of Bayesian polishing and 3D refinement. A final 3D refinement, using a soft-mask that excluded the flexible Fabs and employed solvent-flattened FSC curves to filter the 3D reference at every iteration, resulted in a map with a final global resolution of 3.5 Å after postprocessing. Image processing parameters are listed in Supplementary Information C. For more details on resolution estimation please see Supplementary Information D.

Helical processing of TMV was performed with RELION3 [Zivanov *et al.* 2018] from 481 micrographs of the same data set that contained 20S proteasome, following standard helical refinement and reconstruction procedures [He & Scheres 2017]. The final resolution of the TMV map was 1.9 Å (Supplementary Information D).

Model Building

The model for the native human 20S proteasome was built based on the X-ray structure from Schrader et al. (PDB ID: 5LE5) [Schrader *et al.* 2016]. Chimera [Pettersen *et al.* 2004] was used for the initial rigid-body fitting. The bound Fabs helped to identify the different subunits in the electron density map. For further processing, all heteroatoms were removed. Real space refinement with PHENIX [Adams *et al.* 2010] and manual adjustments in Coot [Emsley *et al.* 2010] were done iteratively to obtain the final model, ending with a cycle of PHENIX real-space refinement. The graphics were generated using Chimera [Pettersen *et al.* 2004] and PyMOL [Schrödinger, LLC 2015].

Acknowledgments

We thank the workshop of the Biozentrum of the University Basel for technical support, A. Fecteau-LeFebvre, D. Caujolle-Bert and K. Goldie for technical assistance, and A. Engel for discussions (all C-CINA, University of Basel). RELION 3 processing was performed at sciCORE (http://scicore.unibas.ch/) scientific computing center at University of Basel. TMV was kindly provided by R. Diaz-Avalos (now at NanoImaging Services). We thank our former coworker Shirley Müller for critically reading the manuscript. **Funding:** We acknowledge support by the Swiss Nanoscience Institute (project P1401 & ARGOVIA MiPIS) and the Swiss National Science Foundation (projects 200021_162521 and 205320_166164), and the Swiss CTI (project 18272.1). **Author contributions:** C. S. performed microfluidic purification and grid preparation. S. A. and R. R. determined the cryo-EM structures. C. S. integrated the trap setup into the CryoWriter platform with the support of L. R. and P. O.. L. K. assisted with Titan Krios data collection. R. R. and I. M. helped C. S. with model building. H. S. provided support and expertise in cryo-EM. T. B. conceived and coordinated the project. C. S., S. A., H. S., and T. B. wrote the manuscript, with backing from all authors. **Competing interests:** T. B. and H. S. declare the following competing financial interest: The cryoWriter concept is part of patent application PCT/EP2015/065398. **Data and material availability:** Image data are available at the EMPIAR database under EMPIAR-10251. The reconstructed volumes are available at the EMDB under EMDB-4738 (20S proteasome) and EMD-4628 (TMV). The atomic coordinates are available at the PDB under PDB-6R70 (20S proteasome) and PDB-6R7M (TMV).

Supplementary Information

A. Characteristics of the Magnetic Trap

The magnetic particle trap consists of two electromagnets arranged with opposite poles facing one another (Figure S1). Attached iron tips extend the magnet cores.

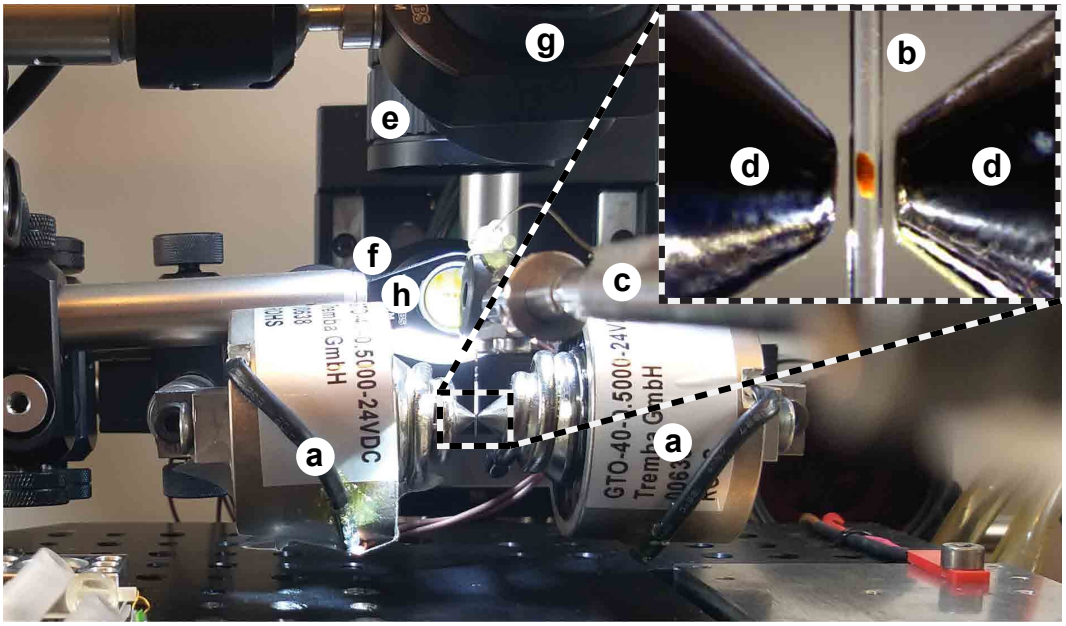

Figure S1: Image of the magnetic trap set-up. The opposite poles of two 4.8 W electromagnets **(a)** are facing one another. A microcapillary **(b)**, held with the manipulator arm **(c)**, is placed between the two iron tips **(d)** of the electromagnets. The trapped magnetic plug can be observed with a camera **(e)** via a mirror **(f)**. The photo-cleavable cross-linker can be exposed to UV light using a LED **(g)** emitting light at 365 nm that is deflected by a mirror **(h)**.

This concentrates the magnetic flux to a small area and forms a strong field gradient between the two tips (see Figure S2). For magnetic particle trapping, the front part of the microcapillary segment just above the nozzle was placed in this region using a motorized XYZ linear translation stage, and the sample was aspirated. The magnetic force acting on the super-paramagnetic particles immobilized the beads. In experiments, super-paramagnetic beads with sizes from 15 nm to 1000 nm can be trapped and experience a magnetic force F_m acting on a saturated particle according to:

$$F_m = V \cdot M_S \cdot \mu_0 \cdot \nabla H \tag{4.1}$$

where V is the volume of the magnetic particles, M_S the saturation magnetization, μ_0 the magnetic constant, and H the magnetic field strength. The current controls the field applied by the electromagnets. Due to the dependence on the volume (V), higher currents are needed in order to trap smaller particles. When the electromagnets are operated at maximum power, the core and the tips significantly heat up. For this reason, a cooling water system was implemented allowing the tips to be cooled to 4 °C by pumping water through a copper tubing twisted around them. Both, the copper tubing and the iron tips were coated with nickel to reduce corrosion. The magnetic trap is mounted on a motorized stage, allowing it to be moved in the vertical direction, independent of the microcapillary manipulator arm. For sample uptake, the magnetic trap and microcapillary were simultaneously moved down to insert the nozzle tip of the capillary into the sample well.

The parts used to build the magnetic trap are summarized in Table S1. Connecting parts were manufactured by the workshop of the Biozentrum, University of Basel, Switzerland. Plans are available upon request. Further cryoWriter parts used for grid preparation are described in [Rima *et al.* 2018]. Figure S2 shows a finite element

Table S1: Parts list of the magnetic trap setup.

Part Name	**Part Number**	**Distributor**
Electromagnet	GTO-40-0.5000-24VDC	Conrad Electronic AG
Iron magnet tips	-	In-house production
Cooling pump	2449120	Digitec Galaxus AG
Tubing for cooling system	1025U04	Parker Hannifin
Tubing for cooling system	1025U06	Parker Hannifin
Motorized trap stage	M-126.PD2	Dyneos AG
Connector plate (trap-stage)	-	In-house production
Camera (Magnetic Trap)	NetFOculusFO124TC	NET GmbH
Optics (trap camera)	MLM3X-MP	FRAMOS GmbH
Mirror (trap camera)	PF07-03-P01	Thorlabs
UV LED	M365LP1c	Thorlabs
Dielectric Mirror	BB0511-E01	Thorlabs
Syringe pump controller	A3921000093	Cetoni
Syringe pump dosing unit	A3921000095	Cetoni
Liquid handling syringe	HA-80901	BGB Analytik AG
Microcapillary tubing	TSP-150375-D-10	BGB Analytik AG
Liquid handling nozzle	FS360-150-30-N-5-C12	MS Wil GmbH
PressFit Connector	2525LD	BGB Analytik AG

simulation of the magnetic flux density within the magnetic trap system, which was caluclated with COMSOL Multiphysics. Soft-iron material properties were applied to the magnet cores and tips using a non-linear B-H curve that includes saturation effects. The windings were modelled with coil features.

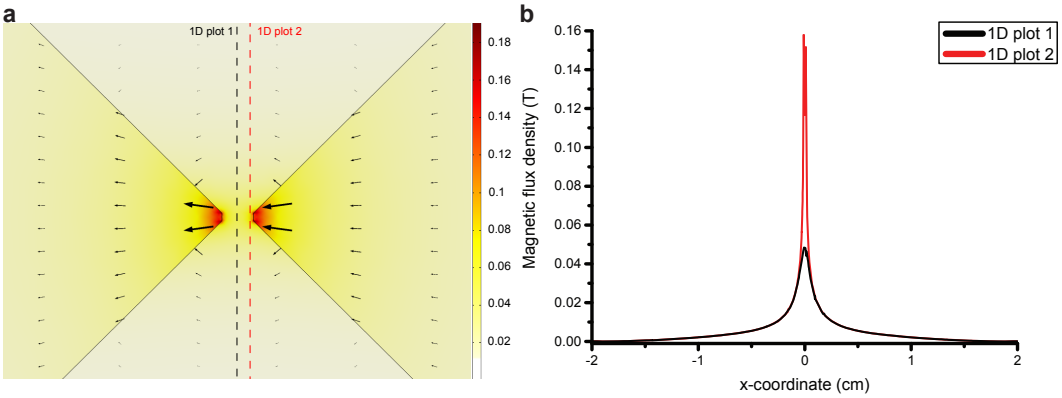

Figure S2: Finite element simulation of the magnetic field generated by the electromagnetic trap system. **(a)** 2D plot of the magnetic flux density around the iron tips (black solid lines). The direction of the magnetic fields is shown with black arrows. The size of the arrows is proportional to the field strength. The values in the color scale are given in Tesla (T). **(b)** Extracted 1D plots of the magnetic flux density from the 2D plot in (a) at the positions indicated with dashed lines. The figure shows that between the tips (x=0) the highest field gradients are observed. This leads to a magnetic force F_m pushing magnetic particles towards this region.

B. Enclosure of Sample Between Air Bubbles

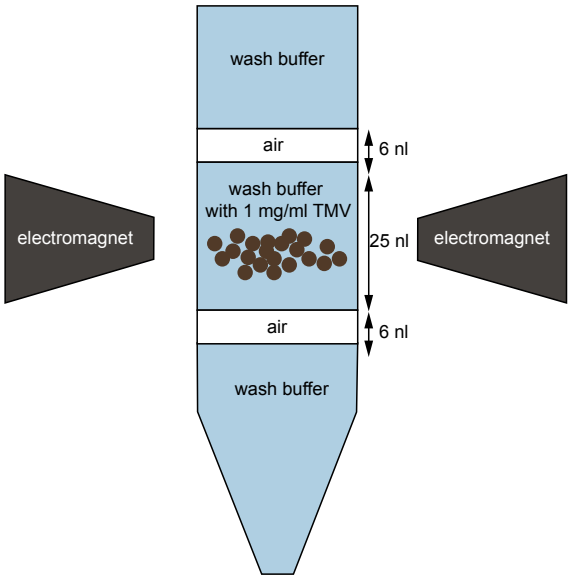

Figure S3: Illustration of the magnetic particle-plug enclosed between two 6 nL air bubbles for UV exposure and elution. The air bubbles act as barriers preventing diffusion and Taylor dispersion to keep the protein concentration as high as possible.

C. Data Collection and Image Processing Parameters

The data collection parameters are provided in Table S2, and the main image processing parameters used for the 20S proteasome and TMV are given in Tables S3 & S4.

Table S2: Data collection parameters.

Data collection	
Voltage	300 kV
Physical pixel size	0.812 Å
Super-resolution pixel size	0.406 Å
GIF zero loss energy window	20 eV
Defocus range	−1.0 µm to −2.2 µm
K2 operating mode	8k super-resolution
Number of frames	30
Second per frame	0.2
Total dose	72 e^{-} $Å^{-2}$
Number of micrographs	523

Table S3: Image processing parameters used for 20S proteasome structure determination with RELION3.

Image processing 20S proteasome	
Micrographs	523
Box size	480 pixel
Box size (after down-sampling)	384 pixel
Pixel size (after down-sampling)	1.015 Å
Gautomatch picked particles	55,135
Particles after 2D classification	38,848
Particles for 3D refinement	16,015
Symmetry	C2
Final resolution	3.5 Å
Estimated map sharpening B-factor	−39.2 $Å^{2}$

D. Fourier Shell Correlation and Local Resolution Histograms

We used the Fourier shell correlation method [Harauz & van Heel 1986] between two independently refined half-maps ('gold standard') [Scheres & Chen 2012] to estimate the resolution of our 3D reconstructions (Figure S4a). A threshold of 0.143 on the FSC curve was adopted to define the resolution limit of the reconstruction [Rosenthal &

Table S4: Image processing parameters used for helical structure determination of TMV with RELION3.

Image processing TMV	
Micrographs	481
Box size	420 pixel
Number of asymetric units	31
Picked end-to-end coordinated	2,676
Extracted particles	52,806
Initial helical rise	22.03°
Particles after 2D classification	52,806
Particles after 3D refinement	52,776
Symmetry	C1
Final resolution	1.9 Å
Estimated map sharpening B-factor	$-38.9\,\text{Å}^2$

Henderson 2003]. The FSC curves were corrected for artificial correlations introduced by masking [Chen *et al.* 2013]. We found a global resolution of 3.5 Å for the 20S proteasome and of 1.9 Å for the TMV. These estimates correlate well with the features observed in the maps (see Figure 3 of the main text for the 20S proteasome and chapter G for the TMV). The estimated resolution is further corroborated by the local resolution histograms shown in Figure S4b, which display the normalized counts of voxels at each resolution. The resolution for the proteasome varies significantly; for more details, see chapter E. The local resolution was assessed based on the half-maps using the method described in [Cardone *et al.* 2013], as implemented in RELION3, with a map sampling of 25 Å (Figure S4b).

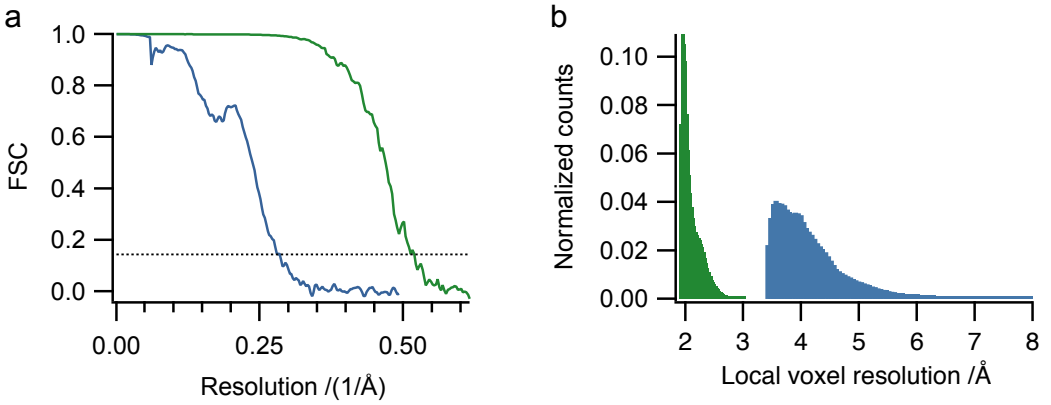

Figure S4: Resolution estimation for the 20S proteasome (blue) and TMV (green). (**a**) Fourier shell correlation from the RELION3 refinement. (**b**) Histograms depicting the normalized voxel counts per resolution range.

E. Local Resolution Map of the 20S Proteasome

Figure S5 shows the local resolution calculated for the 20S proteasome using RELION3. Note that the active domains (indicated by red arrowheads in Figure S5 are less well resolved than the other domains, and are associated with the catalytic subunits of the β-ring. Interestingly, the resolution of the α-ring around the pseudo-seven-fold axis is quite heterogeneous, whereas the β-ring exhibits lower resolution around subunits $\beta 4$ and $\beta 5$. Since subunits $\beta 4$, $\beta 5$ and $\beta 6$ are the catalytically active elements [da Fonseca & Morris 2015], the lower resolution of subunits $\beta 4$ and $\beta 5$ suggests that these are trapped in various conformations during cryo-EM grid preparation.

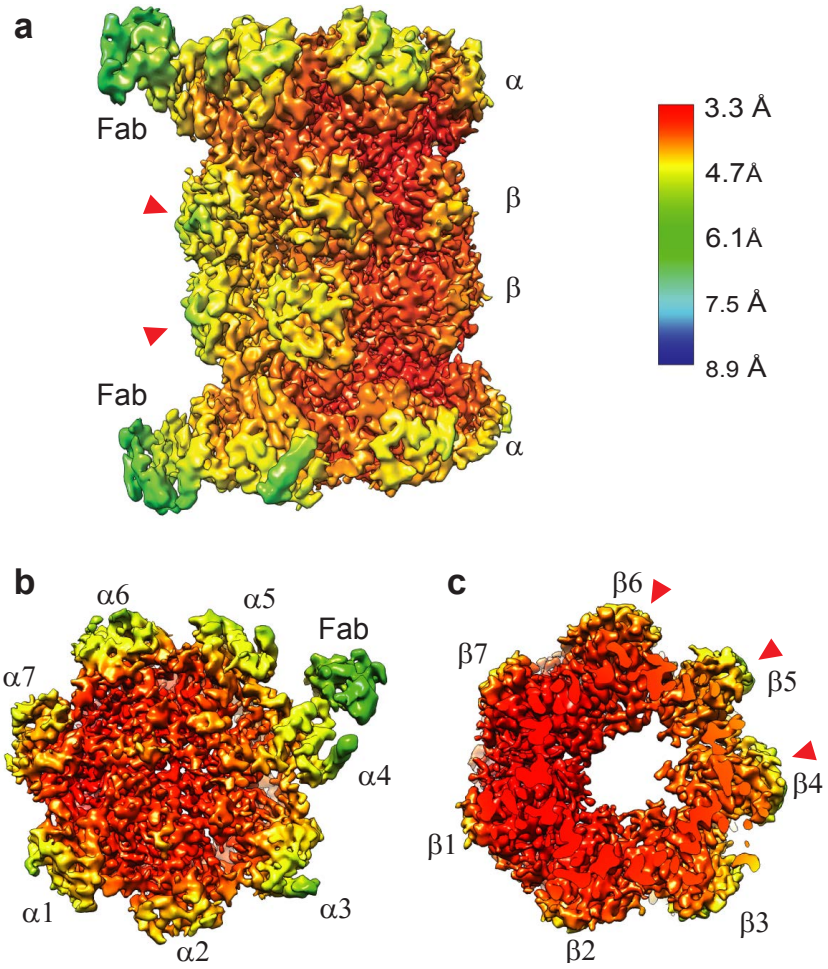

Figure S5: Local resolution map for the human 20S proteasome at a global resolution of 3.5 Å. (**a**) Side view with annotated Fabs. (**b**) Local resolution of the α-subunits. (**c**) Local resolution of the β-subunits. The red arrowheads indicate the catalytically active subunits.

F. Model Building Results

After initial rigid body fitting, the 20S proteasome and TMV models were refined using PHENIX. The models were assessed by the fit to the experimental density and validated with clashscore, Ramachandran statistics, and good bond/angle lengths as shown in Tables S5 & S6. Additionally, a random shift (mean 0.3 Å) was introduced to the final models and each model was refined with the same settings against one unfiltered half map (half-map 1). The FSC curves of the models against half-map 1 and the other half map (half-map 2) was then calculated (Figures S6 & S7). The fact the both curves look very similar indicates that no overfitting took place.

Table S5: 20S proteasome model validation statistics.

Phenix Real-Space Refinement	
Map CC (around atoms)	0.80

MolProbity[**Leaver-Fay *et al.* 2007**]	
All-atom clashscore	4.79
Ramachandran favored	96 %
Ramachandran allowed	2.43 %
Ramachandran outliers	0.26 %
Rotamer outliers	0.52 %
Cb deviations	0
RMSD (bonds)	0.008
RMSD (angles)	1.044

Table S6: TMV model validation statistics.

Phenix Real-Space Refinement	
Map CC (around atoms)	0.87

MolProbity[**Leaver-Fay *et al.* 2007**]	
All-atom clashscore	0.84
Ramachandran favored	97.35 %
Ramachandran allowed	2.65 %
Ramachandran outliers	0 %
Rotamer outliers	0 %
Cb deviations	0
RMSD (bonds)	0.006
RMSD (angles)	0.932

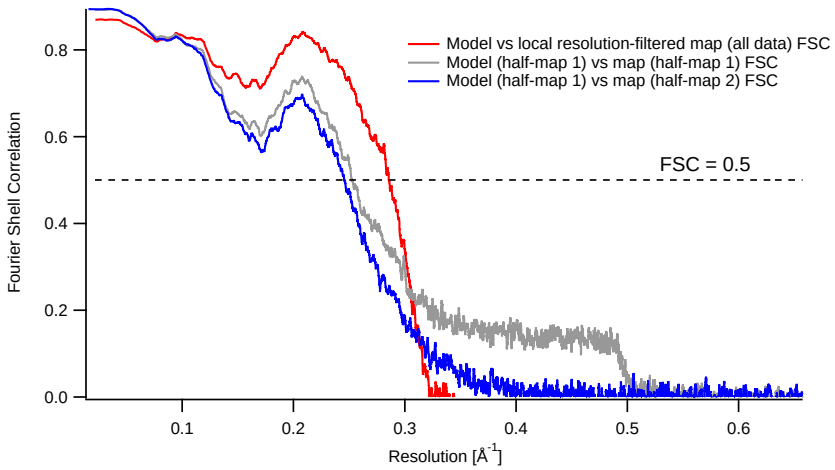

Figure S6: FSC curve of the final 20S proteasome model versus the full map (all data), against which the model was refined (red). The full map used to calculate the FSC was resolution filtered. FSC curve of the final 20S proteasome model with randomized coordinates shifts (mean shifts of 0.3 Å) versus the first unfiltered half-map (half-map 1) against which it was refined (grey) and versus the second half-map (half-map 2) against which it was not refined (blue).

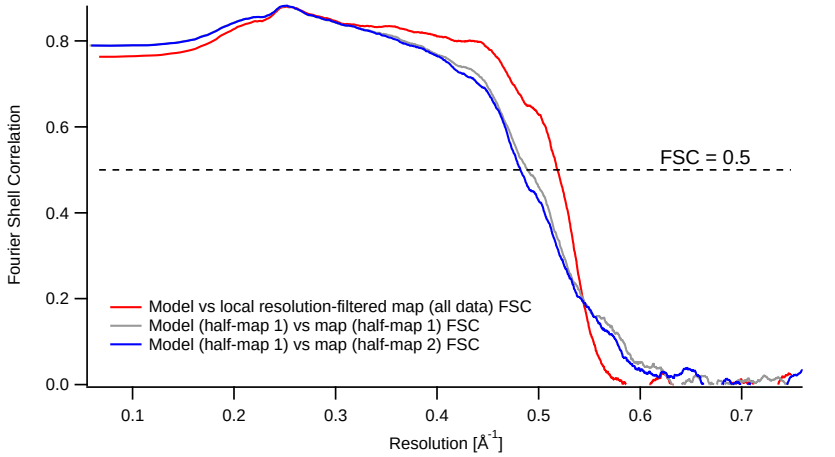

Figure S7: FSC curve of the final TMV model versus the full map (all data), against which the model was refined (red). The full map used to calculate the FSC was resolution filtered. FSC curve of the final TMV model with randomized coordinates shifts (mean shifts of 0.3 Å) versus the first unfiltered half-map (half-map 1) against which it was refined (grey) and versus the second half-map (half-map 2) against which it was not refined (blue).

G. Three-Dimensional Map of TMV

Fig. S8 demonstrates the high quality of the microfluidic grid preparation. We report here the map of TMV at a global resolution of 1.9 Å. Compared to the 20S proteasome, this map has both higher global resolution (see FSC curve in D, Fig. S4a) and less variable local resolution (Fig. S4b) due to the higher rigidity of the structure and the helical symmetry averaging imposed on the reconstruction.

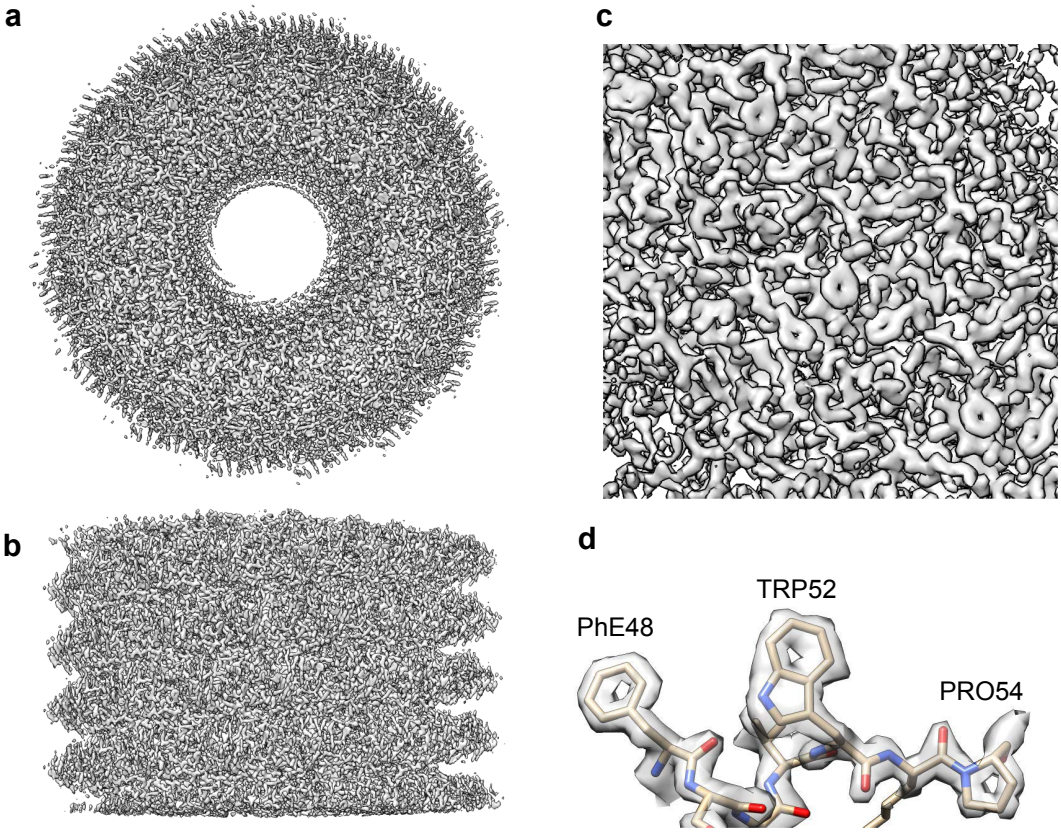

Figure S8: 3D reconstruction of TMV at a global resolution of 1.9 Å showing the top view ((**a**) and the side view (**b**) of the electron density map. The zoom-in (**c**) demonstrates the high resolution features of the map. At this resolution it is possible to see the holes of the aromatic rings (**d**).

5. Few Cell Analysis for Correlative Metabolomics and Targeted Proteomics

This section discusses the development of a correlative method for metabolomics and targeted proteomics. It is a combination of the *cryoWriter* setup with mass spectrometry and reverse-phase protein arrays (RPPA). Using this combination, cellular structures can be investigated together with their metabolites and proteins.

My contribution was the co-development of this method, the execution of the cell experiments in *cryoWriter* setup, the RPPA analysis, the creation of the figures and the co-writing of the manuscript.

The following section is planned for submission

Few Cell Analysis for Correlative Metabolomics and Targeted Proteomics

Luca Rima[1], Christian Berchtold[2], Rosmarie Sütterlin[1], Stefan Arnold[3], Gregor Dernick[4], Götz Schlotterbeck[2] and Thomas Braun[1]

1 - Center for Cellular Imaging and NanoAnalytics, Biozentrum, University Basel, Switzerland
2 - FHNW Fachhochschule Nordwestschweiz, Hochschule für Life Sciences
3 - Sensirion AG, Switzerland
4 - F. Hoffmann-La Roche AG, Switzerland

Contents

5.1. Introduction **94**
5.2. Experimental Section **95**
5.3. Results **98**
5.4. Discussion **102**
5.5. Conclusion **103**

Abstract

To understand biological processes, it is of major importance to investigate the underlying processes at a cellular level. Due to several drawbacks in analyzing with the commonly performed batch lysate experiments, like dilution and averaging of signals, methods to study single cells are urgently needed. Here we present a working protocol to investigate metabolites and proteins from single adherent cells. First, cells are picked using a previously described single-cell picker and lysis apparatus from a fluorescent microscope's cell incubator. The lysates are then transferred using suitable slides to liquid-chromatography mass spectrometry (LC-MS) for the analysis of metabolites. The same type of slides can also be used for the detection of proteins using reverse-phase protein array technology. This method provides a correlative measurement of cellular structures, metabolites and proteins from single cells. The direct interface for picked cells deposited on a suitable slide with LC-MS enables new capabilities for highly sensitive measurements of single and few cells without sample preparation. The proof of concept results achieved here suggests that by ramping up the throughput in the future, this technique can help answer biological and medical questions at the single-cell level.

5.1. Introduction

A complex interplay of proteins, lipid-membranes, nucleic acids, and metabolites defines the biological systems' phenotype. However, the analysis of these interaction networks is complicated by their stochastic nature and cellular heterogeneity in cell cultures and organs. Therefore, the characterization on the few-cell, or, better, the single-cell level is essential [Wang & Bodovitz 2010], not only reducing biological noise [Newman *et al.* 2006], but also enabling new conceptions of biological experiments and data-analysis methods.

The tiny amounts of sample complicate single-cell (and few-cell) analysis. For the genome and transcriptome, amplification techniques are available for single-cell analysis [Newman *et al.* 2006, Tang *et al.* 2009]. The study of single cells' metabolome is currently dominated by targeted and dedicated approaches for the detection of specific metabolites not using a chromatographic separation system. Still, metabolome analysis by mass spectrometry (MS) suffers from low absolute metabolite quantities present in single cells. For protein investigations, so far, only paramount proteins can be detected. A potential approach for the unlabeled analysis of a single cell's proteome is provided by the single-molecule characterization power of electron microscopes. However, the 'visual proteomics' approach currently only allows the detection of large protein complexes [Syntychaki *et al.* 2019, Nickell *et al.* 2006, Beck *et al.* 2009, Förster *et al.* 2010]. The third class of methods rely on cognitive molecules,

such as antibodies, and are routinely used by immunofluorescence microscopy and flow cytometry.

Not only the acquisition of few-cell or single-cell data is difficult, but also the analysis of the information. Many samples of few or single cells must be individually characterized, which require high-throughput approaches and extensive bioinformatics for data interpretation. A significant improvement can be achieved by using correlative methods allowing the simultaneous acquisition of information of multiple domains, e.g., the characterization of proteins and metabolites.

Here we present a new strategy for the correlative few-cell analysis of proteins and metabolites. Using a light microscope that allows for live-cell imaging, we integrated a single-cell lysis device for adherent eukaryotic cells. A handover system enables the analysis of the cell lysate subsequently for metabolites by liquid-chromatography mass spectrometry (LC-MS) and target proteins by reverse-phase protein array (RPPA) technology. Our data provide proof-of-concept measurements for few-cell experiments (1 cells to 10 cells) and demonstrate the feasibility of correlative single-cell analysis.

5.2. Experimental Section

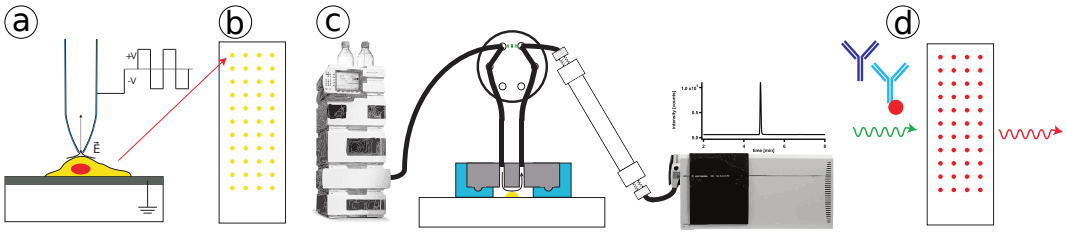

Figure 1: Workflow for the correlative analysis of cells. Cellular structures are revealed by light microscopy, metabolites by mass spectrometry, and proteins by reverse-phase protein arrays (RPPA). **(a)** The cell is imaged using a (fluorescence) light microscope. A target cell is located and lysed under microscopy supervision. **(b)** The lysate is transferred (spotted) onto a carrier slide. **(c)** The metabolites are extracted and analyzed by liquid-chromatography mass spectrometry (LC-MS). **(d)** Finally, proteins are detected by immunolabeling.

Cell Preparation

The cells (SH-SY5Y Cell Line human, 94030304, Sigma, Switzerland) were grown in a proliferation medium consisting of $1:1$ v/v mixture of DMEM (Dulbeccos Modified Eagles Medium, D6171, Sigma, Switzerland) and HamF12 (Nutrient Mixture F-12Ham, N8641, Sigma, Switzerland) with 5 % FCS (Fetal Calf Serum, E7524, Sigma, Switzerland), L-glutamine (G7513, Sigma, Switzerland) and NEAA (Non-Essential

Amino Acids, M7145, Sigma, Switzerland). After three days of proliferation in 5 % CO_2 at 37 °C the cells were washed with Phosphate-buffered saline (PBS), detached by adding trypsin-EDTA (0.05 % Trypsin, 0.53 mM EDTA; 25300-054, Invitrogen, Switzerland), diluted with proliferation medium and centrifuged for 5 min at 800 rpm. The supernatant was removed and the pellet resuspended in medium. A small amount was further diluted and sent into proliferation again. The rest was used to prepare the single-cell lysis indium tin oxide (ITO) coated glass slides. These slides were first sterilized in 70 % Ethanol, subsequently dipped in 100 % Ethanol and flame-sterilized. Poly(dimethylsiloxane) (PDMS, SYLGARD 184, Dow Corning, USA) rings were put on top on the ITO coated side to form small wells. After treating the wells with poly-L-lysine (PLL, P8920, Sigma, Switzerland) for 15 min the cells were loaded at a concentration of 10^4 cells per well and grown in 5 % CO_2 at 37 °C for 2 d.

Single Cell Picking

Cell picking and lysis was performed with the cryoWriter setup [Rima *et al.* 2018, Arnold *et al.* 2016, Kemmerling *et al.* 2013]. The cell slides and transfer slides (NEXTERION® Slide H, Schott, Germany) were placed in a cell incubator (Modell, Tokai Hit, Japan) in 5 % CO_2 at 37 °C mounted on top of an inverted microscope (Axiovert 200, Zeiss, Germany) with a motorized stage (H117EIL5, Prior Scientific, UK). Two metal screws additionally grounded the cell slides. A micro-capillary (Picotip, New Objective Inc., USA) with a conductive coating (20 nm Ti−W, 200 nm Pt) was implemented for cell picking, electrical cell lysis and lysate deposition. The micro-capillary was mounted on three linear stages (x, M-414.3PD; y,z, M-404.2PD, Physik Instrumente, Germany) and was connected to a syringe (1701 LT SYR, Hamilton, USA) on a high-precision syringe pump (neMESYS, Cetoni GmbH, Germany). The whole system was primed with degassed pure water (Water for Molecular Biology, Merck Millipore, Germany) with almost zero dead volume for precise pipetting. A function generator (33220A, Agilent, Switzerland), combined with a voltage amplifier (F20A, FLC Electronic AB, Sweden), was connected to the conductive coating of the micro-capillary. When everything was set up, the cell medium was removed, and the wells were washed three times with PBS. Cells were selected with the light microscope. The capillary was positioned 10 µm above the target cell. 50 nL of water was dispensed next to the cell to introduce osmotic pressure. Three square pulses ($f = 2$ kHz, $A = \pm 9.5$ V) were generated for the electroporation of the cell. At the same time, 3 nL containing the cell lysate were aspirated. The lysate was then deposited on the transfer slides in a distinct spiral pattern and dried under an argon atmosphere. After spotting, the slides were transferred to the LC-MS under an argon atmosphere in a lightproof tube.

Batch Lysate Preparation (SH-SY5Y)

Until centrifugation, the cells (SH-SY5Y Cell Line human, 94030304, Sigma, Switzerland) were prepared the same way as described before. Then the pellet was washed and dissolved in 25 mM HEPES−KOH, 5 mM $MgCl_2$, pH 7.5. The cell concentration was determined by counting (6×10^6 cells/mL). Cells were lysed by sonication (UP200St, Hielscher, Germany) for 40 s ($P = 200$ W, $f = 26$ kHz).

Batch Lysate Preparation (LUHMES)

Lund human mesencephalic (LUHMES) cells were grown and differentiated according to a published protocol [Scholz *et al.* 2011]. For the preparation of batch lysate the cells were washed with PBS and lysed using a lysis buffer (50 mM Tris buffer (Sigma, Switzerland), pH 8.2, 75 mM NaCl (Sigma, Switzerland), 8 M urea (Sigma, Switzerland), protease inhibitor cocktail (complete mini, Roche, Switzerland), 1 mM phenylmethylsulfonyl fluoride (PMSF) (Sigma, Switzerland), 10 mM sodium pyrophosphate (Sigma, Switzerland), 1 mM sodium orthovanadate (Sigma, Switzerland), 1 mM β-glycerophosphate (Sigma, Switzerland)). The batch lysate was aliquoted and subsequently stored at −20 °C. Before use, the aliquots were diluted with water to a final concentration of ∼1250 cells/µL [Arnold 2017].

Mass Spectrometry

The system consists of a thin-layer chromatography (TLC)-interface (TLC-MS Interface 2, CAMAG, Switzerland), which has been connected with a binary high-performance liquid chromatography (HPLC) pump (1100, Agilent, USA) and a 6 port, 2 position valve. A water-resistant C18 column (Cortecs T3 2.1x1002.7 µm, Waters, USA) was used. The TLC-MS interface's extraction head was modified with a 3D printed polypropylene cap for proper sealing with the transfer slides. Figure 1 shows the actual configuration. The interface was established between a high-resolution mass spectrometer (LTQ-Orbitrap XL, Thermo Scientific, USA) as well as a low resolving triple quadrupole system (6460, Agilent, USA) equipped both with an electrospray ionization (ESI) source (AJ-ESI, Agilent, USA). For non-targeted analysis (Orbitrap) and for the initial evaluation a gradient starting at 100 % water containing 0.1 % formic acid holding at this conditions for 1 min followed by a linear gradient for 6 min to 100 % methanol containing 0.1 % formic acid at a flow rate of 0.5 mL min^{-1} was used. For targeted analysis (triple quadrupole) the gradient was isocratic staying at 100 % water, 0.1 % formic acid for 1 minute followed by a linear gradient of 2 min to 100 % acetonitrile containing 0.1 % formic acid. The multi reaction monitoring (MRM) modes used were $148 \rightarrow 84, 6$ / collision energy

(CE) = 14 for glutamic acid; 147 → 130 / CE = 15 for glutamine; 154 → 137 / CE = 2 for dopamine. Nicotine was used as standard to validate alignment and system performance. A sensitivity in the low pg (Orbitrap) to fg (triple quadrupole) range was achieved for all standards. However, sensitivity of the current set-up could not exactly be determined.

Immunolabeling

First, the slides were treated with a blocking solution (Roti-Block, Carl Roth, Germany) for 90 min. Subsequently the slides were incubated with primary antibodies (mAb mouse anti-actin IgG CLT 9001, pAbs rabbit anti GAPDH IgG ab37168) each at a concentration of 1 µg mL^{-1} in washing buffer (10 : 1 mixture of PBST 0.05 % and blocking solution) for 20 h. Afterward, the slides were washed for 30 min in washing buffer and subsequently incubated with secondary antibodies for 60 min. For the infrared scanner (Odyssey 9120, Li-Cor, USA), donkey anti-rabbit IgG 926-68073 and donkey anti-mouse IgG 926-32212 at a dilution of 1 : 10′000 in washing buffer was used. For the fluorescent microscope (Axiophot, Zeiss, Germany) Alexa 488 donkey anti-rabbit IgG 711-545-152 and Cy3 donkey anti-mouse IgG 715-165-151 at a dilution of 1 : 1000 or 1 : 3000 respectively in washing buffer were used. The slides for the fluorescent microscope were subsequently covered with Mowiol 4-88.

5.3. Results

We combined a single cell picker mounted on a light microscope [Kemmerling *et al.* 2013, Arnold *et al.* 2016] with a hand-over system, which allows the deposition of nanoliter sized sample volumes on a carrier-slide for subsequent correlative analysis by (i) LC-MS, and, (ii) RPPA (Figure 1). Several samples can be dispensed on the carrier slide in the form of an array. For the metabolite analysis by LC-MS, the low-molecular-weight analytes were extracted from a selected sample-spot by a solvent using a modified TLC-MS interface (Supplementary Information B). The extraction system is directly connected to an LC-MS and allows the metabolite analysis in a targeted or untargeted configuration. The system allows the sequential analysis of all sample spots on the carrier by LC-MS. For protein-detection, an RPPA immunoassay was used, and the whole slide is incubated with a primary and secondary antibody. Combined, this workflow enables the correlative measurement of cellular structures, metabolites, and proteins.

We tested the workflow first using batch cell lysate. In this case, standard cell culturing protocols were used to grow the cells. Subsequently, the cells were detached and lysed. This allowed the dispensing of cell lysate amounts scalable between 1

to 20 cells. Furthermore, we tested the set-up using the single-cell picker to lyse individual single cells grown on poly-lysine functionalized ITO coated slides in miniaturized Petri dishes.

Assay Development Using Batch Cell Lysate

The use of a suitable carrier-slide is crucial for the subsequent analysis by LC-MS and RPPA. The slides need to fulfill the following criteria: resistance to the used extraction solvents, proper sealing with the extraction-interface, and proteins must be retained on the slide for the subsequent analysis by RPPA.

We tested different materials for the carrier-slide. Slides made from PTFE, PEEK, and COC polymers were examined as potential sample carriers. These polymers seal sufficiently up to 400 bar and might be used for this work-flow (data not shown). All in all, the COC slides were the most suitable in pliability, solvent resistance, and, importantly, provided no additional background signals in the mass spectrometer. COC seems to be the ideal carrier material for the analysis of metabolites by LC-MS. Moreover, COC is transparent and, therefore, well suited for all kinds of light-microscopy.

The first experiments were performed using a dilution series of LUHMES batch lysate. We tested the hand-over and LC-MS extraction system using the Orbitrap configuration for the targeted and untargeted detection of metabolites. The initial untargeted experiments showed that this interface can transit several metabolites for LC-MS analysis even at a low number of cells. Glutamic acid was also measured using targeted MRM showing that this configuration provides measurements down to a level of approximately 2.5 cells, even quantitatively (Figure 2d). Further tests were performed using diluted SH-SY5Y batch lysate. Measurement and the corresponding RPPA dot-blot is shown in Figure 2 a & c. An evaluation of the signal intensities from Figure 2a and the peak areas of Figure 2c is given in the column plot in Figure 2b. This data is not sufficient for accurate quantification of the metabolites and proteins but shows a clear dependency on the number of analyzed cells.

Single Cells

The combined forces of electroporation and suction were used to pick adherent eukaryotic cells under the supervision of a light-microscope. The microcapillary is coated with an 200 nm Pt layer, and the cells are grown on an ITO-coated, PLL-functionalized surface. This allows the destabilization of the target-cell by electro-pulses (3×0.5 ms, amplitude of 9.5 V, and a nozzle distance of $\sim$10 µm from the cell). Simultaneously, a volume of 3 nL is aspirated, which takes up the

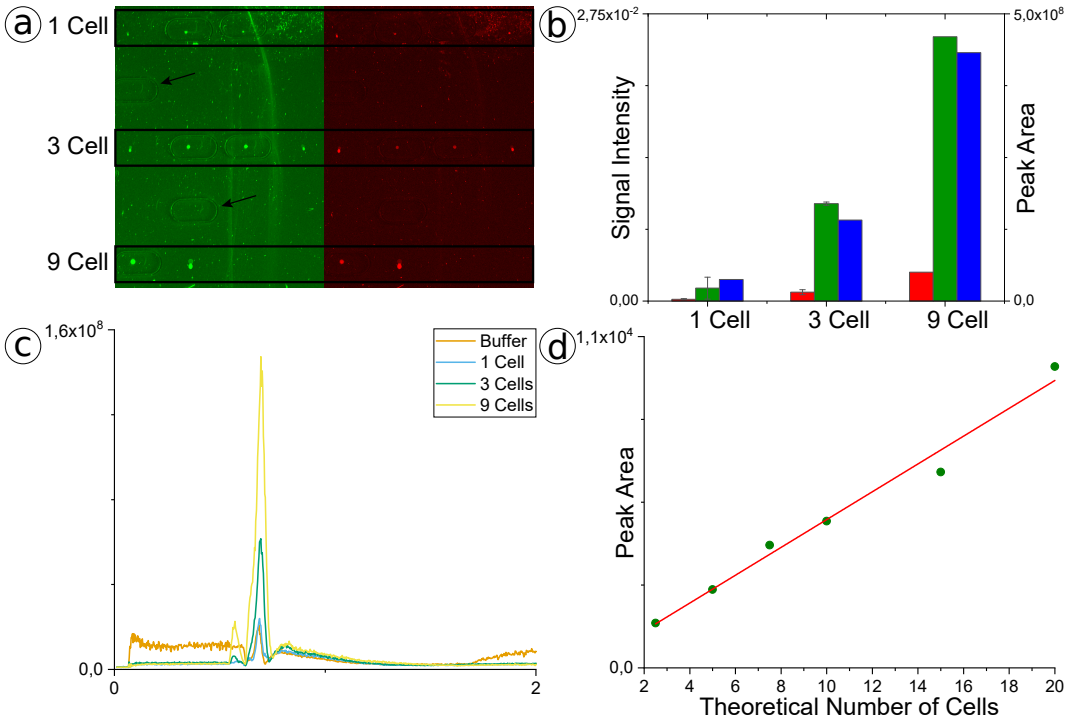

Figure 2: Assay development using batch cell-lysate. RPPA dot-blots (a) and corresponding HPLC-MS base peak chromatograms (c) of SH-SY5Y batch lysate diluted to an equivalent of 1, 3 and 9 cells. **(a)** For the RPPA analysis, two abundant proteins were analysed: actin (red) and GAPDH (green). Positions of extraction can be recognized by the imprint of the HPLC-MS interface. The black arrows indicate blank positions. For 1 and 3 cells four dots and for 9 cells two dots are present. **(b)** Comparison of intensities from panel (a) and peak areas of the most intense peak in panel (c) for 1, 3 and 9 cells. **(c)** Base peak chromatogram of the untargeted LC-MS experiment on the Orbitrap instrument. Mass range 80-500. Spectra shown in Supplementary Information C shows clear differences between buffer and cells also in a semi-quantitative matter. **(d)** Targeted experiment using the MRM of glutamic acid on the Orbitrap setting (linear trap). The linear regression shows an equivalent amount of 2.5 cells is needed to detect this metabolite in this configuration.

cell lysate into the microcapillary. The whole cell-lysis process takes less than one second; see [Kemmerling *et al.* 2013] for a detailed discussion. Unfortunately, all polymers discussed in the section before did not retain the proteins efficiently during the metabolite extraction. The sensitivity for the subsequent detection of the proteins on the single-cell level was significantly degraded (Supplementary Information A). Therefore, we tested functionalized glass slides, which allow the covalent immobilization of proteins via their primary amines, e.g., lysines. Figure 3 shows a RPPA dot-blot from single picked cells on such a functionalized glass slide before metabolite extraction. Single cells can be easily detected and the overall quality of the RPPA dot-blot is better than with the previously utilized COC slides.

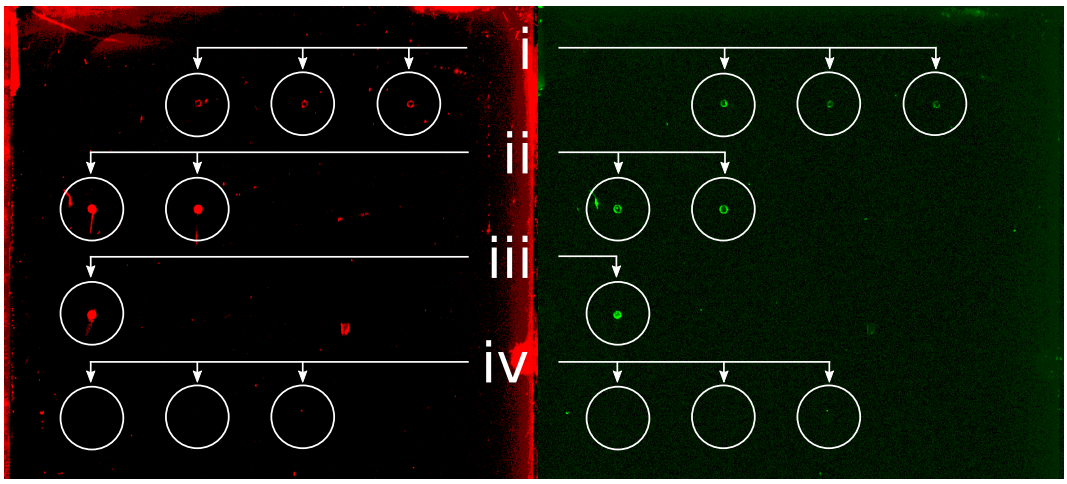

Figure 3: Single cell RPPA dot-blot on a functionalized glass slide. GAPDH is represented in green, actin in red. **(i)** 1 Cell, **(ii)** 5 Cells, **(iii)** 10 Cells, **(iv)** 10, 20 and 30 nL of the buffer surrounding the cells as a negative control (from left to right).

Because glass slides are not self-sealing with the extraction interface for LC-MS, and tend to break, we used 3D printed polypropylene caps as a washer in-between the glass carrier-slide and the extraction head (Supplementary Information B). This configuration enabled the combined analysis of metabolites by LC-MS and proteins by RPPA on the single-cell level. Nevertheless, it is important to note that even with the functionalized glass slides a lot of protein is lost during metabolite extraction and only remnants can be detected by RPPA.

One single-cell measurement is depicted in Figure 4. We lysed an individual SH-SY5Y cell under the supervision of a light microscope (Figure 4a) and transferred the cell-lysate onto a functionalized sample carrier. LC-MS analysis was performed on a triple quadrupole LC-MS system using the modified TLC-Interface. The eluent was used to transfer the metabolites onto the column. Figure 4b shows the MRM chromatograms of glutamine (Figure 4b (i)), dopamine (Figure 4b (ii)), and glutamic acid (Figure 4b (iii)) overlaid with the signals recorded from a blank. In this measurement, the signal to noise ratios (SNR) of the Glutamine, Dopamine, and Glutamic acid measurements are 35.9, 1.8, and 2.7, respectively. The rather low SNR values of dopamine and glutamic acid suggest that the mass spectrometer was operating close to its detection limit and that the metabolites are probably also partly retained on the slide. Even if the data clearly does not allow for quantification, signals of the metabolites can be detected. Considering that much more sensitive LC-MS systems are already on the market (e.g., Agilent 6495 MS systems or others), quantifying these metabolites would be feasible today. Figure 4c shows the corresponding dot in the RPPA analysis for actin (red) and GAPDH (green) superimposed. Integration shows that the proteins

are indeed detected and exhibit an SNR of 1.1. There are three reasons for this low SNR: First, the fluorescent camera was operating close to its detection limit. Second, we observe a large deposition area of the droplet. Particularly, a "coffee-ring" effect is visible, which is occurring during the drying process after sample deposition. This effect leaves behind a big area without significant amounts of cell-content, which is accumulated almost exclusively toward the droplet's edges. Thirdly, despite the use of functionalized slides, some proteins are still lost during the extraction process. More measurements (data not shown) were performed in the same way, yielded similar results with variations in signal strength in LC-MS, and the RPPA analysis supporting the interest to investigate cells at the single-cell level.

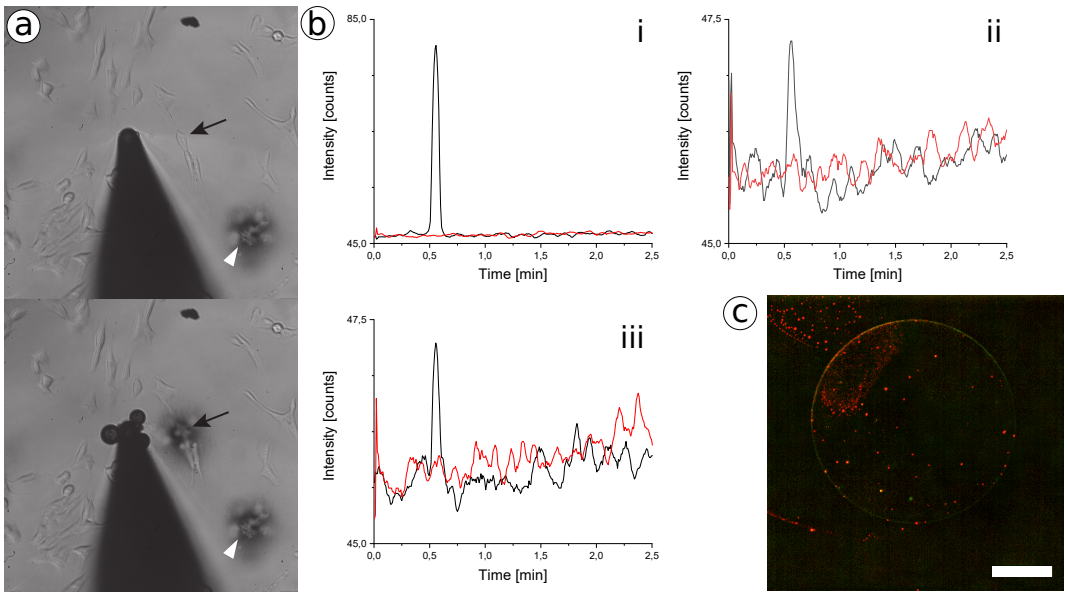

Figure 4: Correlative single-cell analysis. **(a)** Cell picking: Black arrows point to the cell before and after cell-lysis. The white arrowheads indicate a previously lysed cell. **(b)** Single-cell HPLC-MS analysis of Glutamine (i), Dopamine (ii), and Glutamic acid (iii). The signal of the metabolites is represented in black and for the blank in red. **(c)** Dot blot of the corresponding cell. The signals for actin (red) and GAPDH (green) are superimposed. Scale bar: 120 µm.

5.4. Discussion

The presented setup and strategy enables the analysis of single and few cells by several technologies comprehensively. The main advantage of LC-MS analysis is transferring the complete sample into the instrument and the in-cooperation of a chromatography column. This enables a sensitive measurement using chromatography advantages without losing analyte by sample preparation or within an injection vial. Using

untargeted settings, it was shown that numerous metabolites could be analyzed, even if the sensitivity does not reach a true single-cell level. The cell picking device could overcome this sensitivity issue by lysing several cells of the same appearance turning the experiment into a sophisticated few-cell experiment. There are indications that if the sensitivity is reached, a quantitative measurement would be possible. However, the focus was on qualitative measurement. The presented concept allows many different applications, but several difficulties should be overcome to optimize this interface for research applications. The main analytes in focus (glutamic acid, glutamine, and dopamine) do not show much retention on the column and, therefore, do not take full advantage of the chromatographic dimension. For future experiments or other applications, a more suitable choice of the column may be needed. The second critical issue is the manual nature of the current configuration. It is difficult to maintain the correct alignment of the TLC-MS interface and is too time-consuming to measure a statistically relevant amount of cells. Automation of the cell picking and analysis is, therefore, an important next step in further development. This is possibly also critical for some metabolites of low stability (e.g., dopamine).

The final experiment using the hydrogel transfer slides and the more sensitive configuration of a triple quad instrument focusing only on three main metabolites was combining all techniques proofing the comprehensiveness of the current setup qualitatively. However, optimizations are required. In order to eliminate differences resulting from the experimental setup, a more sensitive mass spectrometer and a better fluorescence camera could be implemented and the proper function could be validated by intensive testing of different standard solutions. The coffee ring effect can be avoided by keeping the deposited sample for a few seconds at the dew-point temperature. This would also allow the primary amines of the proteins to react with the NHS-groups of the functionalized glass slide, before the sample spot is dried by increasing the temperature. Since the modified TLC interface allows the use of a variety of slides, different functionalization's could also be tested to improve protein retention. For the future, however, it has to be considered that there is no risk of binding the metabolites of interest.

5.5. Conclusion

By the combination of three different techniques this new method presented here offers great opportunities for single-cell analysis. The transfer protocol developed enables the combination of the cryoWriter setup together with the powerful techniques of LC-MS and RPPA analysis. The possibility to obtain optical information from light microscopy, information about metabolites from mass spectrometry and information about proteins by RPPA from single cells offers new ways to answer important biological and medical questions. The proof of concept of this new method has been

successfully demonstrated. In the future, an additional fluorescent labeling of the cells would help selecting cells of interest. Also, automation of the cryoWriter setup and the MS interface will be of great importance to increase the throughput substantially in order to receive statistically significant results and the implementation of a more sensitive mass spectrometer will offer the possibility to detect and potentially quantify a sufficient number of metabolites of interest.

Author Contributions

L.R. performed the cell experiments in the cryoWriter setup and the RPPA analysis. C.B. performed the mass spectrometry measurements. R.S. was responsible for the cell culturing and provided expertise in immunolabeling. S.A. performed and developed the initial experiments. G.D. performed the first RPPA experiments. G.S. coordinated the mass spectrometry measurements. T.B. coordinated the project. L.R., C.B., and T.B. wrote the manuscript.

Conflicts of Interest

The cryoWriter is element of the PCT/EP2015/065398 patent application.

Supplementary Information

A. COC Slides

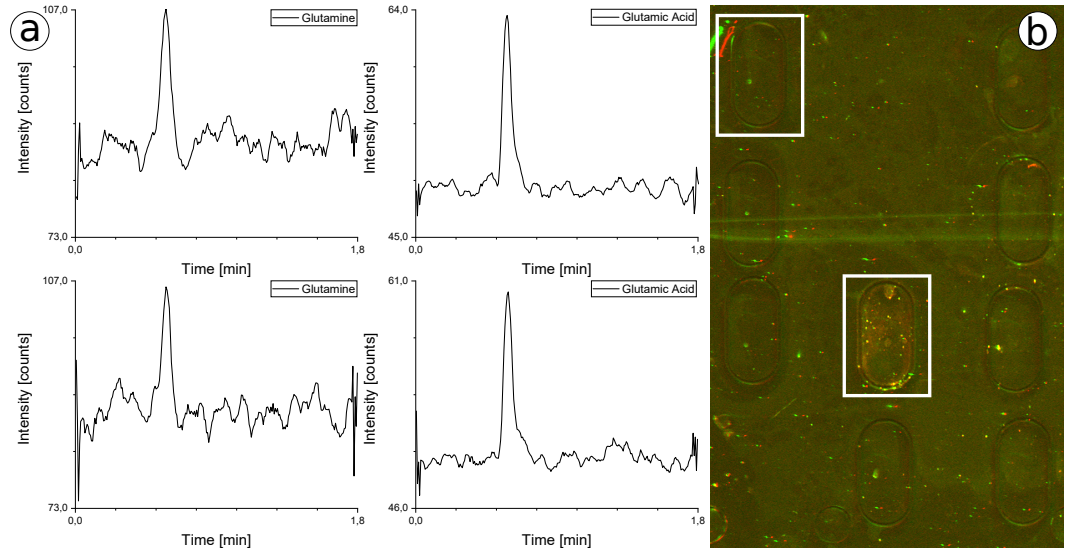

Figure S1: Using COC slides HPLC-MS analysis was feasible as can be seen in in panel **(a)** for glutamine and glutamic acid. The immunolabeling yielded no distinct results. The white frames in panel **(b)** indicate the areas of measurements.

B. 3D Printed Polypropylen Cap

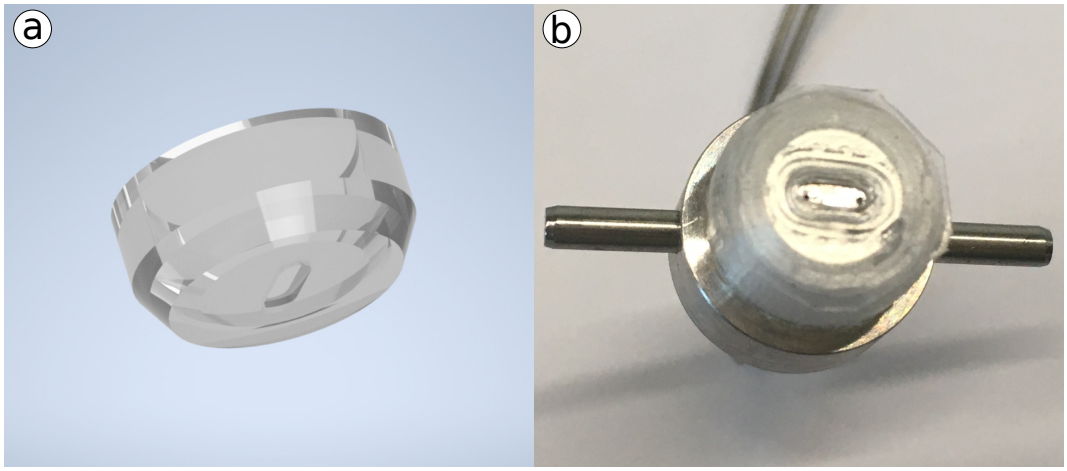

Figure S2: **(a)** Rendered image of the 3D printed polypropylen cap for sealing. **(b)** Picture of the cap mounted on the extraction head of the TLC-MS Interface 2.

C. Mass Spectra

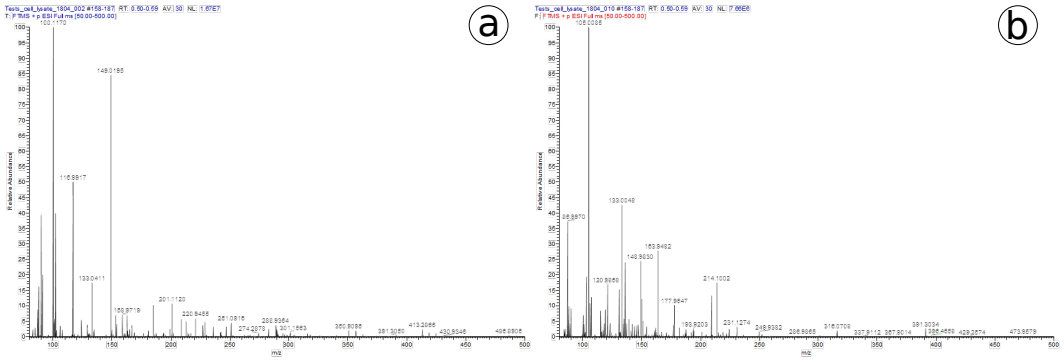

Figure S3: Extracted mass spectra. Mass range 80-500 from the main peak (Retention time 0.5 -0.59 min) is shown. **(a)** is the buffer and **(b)** shows 9 cells. There is a number of metabolites seen, which are also represented in the buffer. However there is a clear difference in intensity and number of signals.

6. Conclusion and Outlook

Conclusion

The field of cryo-EM has experienced a veritable boom in recent years. Developments in electron detection and data processing as well as automation in data acquisition have contributed significantly to this development. Today, cryo-EM has increasingly become the method of choice for the structural elucidation of biological macromolecules. Therefore the required equipment is made accessible and operational for more and more people in the scientific community and industry by continuous improvements and openings of new EM centers. A new front of scientific developments in recent years is the progress in sample preparation. After years of stagnation, this aspect of cryo-EM is now gaining momentum and an increasing number of scientists are trying to improve the established methods, which are turning into a major bottleneck. To do this, they have to deal with problems that are caused by the properties of thin aqueous films. These include both stability problems and associated difficulties in preparation, as well as problems with the conditions that are very hostile to biological macromolecules. The aim of this thesis was therefore to further develop and extend the approach pursued by our group, namely the microfluidic sample preparation for EM. To this end, the existing system was first improved in various aspects and the working protocols were adapted and optimized. The improved system is now able to produce samples much more reproducibly, offers more control over the processes and has comfort functions for operation. It is therefore better suited for inexperienced users and allows respectable results to be obtained more quickly. At the same time, new extensions have been added, which offer completely new possibilities and expand the range of experiments that can be performed. These include the *climateJet* and the magnetic trap, which were discussed in more detail in this thesis. The *climateJet* offers the possibility to create a well-defined microclimate around the grid during sample preparation. This expands the parameter space, which increases the possibilities in grid preparation and allows better control, which in turn leads to better reproducibility. Furthermore, it decouples the setup from the influence of changing room conditions, which have often been a problem before. It also offers the possibility of transporting surfactants via the gas phase to the grid, which opens up the opportunity to use them systematically in grid preparation. A "cover slip" made of surfactants could shield macromolecules from the air-water interface and help to maintain their conformations and prevent preferred orientations. The magnetic trap takes advantage of the fact that the protein quantity required for structure determination is easy to handle microfluidically and that such small quantities can be prepared with the *cryoWriter* setup for examination in a TEM. For this purpose, superparamagnetic particles are used, which can be functionalized with specific linker molecules. If the target structures bind to such particles, they

can be immobilized in the same capillary required for grid preparation using the magnetic trap and separated from other components. The isolated target structures can then be cleaved from the particles or prepared together for TEM analysis. In contrast to classical sample purification and preparation, which require relatively large volumes, the use of the *cryoWriter* in combination with the magnetic trap allows working with very small quantities. This is on one hand cheaper, and on the other hand makes new biological macromolecules accessible, which were previously either not available at all or only in too small amounts or too low concentrations due to problems in expression or purification. Another feature of the *cryoWriter* used in this thesis is the ability to pick and lyse single cells. The collected cell lysates can then be prepared for negative staining EM or cryo-EM and analyzed using a "differential visual proteomics" approach. Thereby proteins from single cell lysates are classified and the obtained classes of different cells are examined for their relative frequency. This allows one to exploit the single molecule resolution of TEM for the proteome-wide comparison of protein structures. The lysates can also be prepared for other analytical methods that can provide complementary information. The use of a suitable slide allows the mass spectrometric analysis of the single cell lysates, which enables the investigation of metabolites. However, for single cells the resulting signals are still below or just above the detection limit, which may change in the future due to improvements in mass spectrometry. The same slides can also be used for reverse-phase protein array studies, allowing the detection and, to a certain extent, quantification of proteins for which specific antibodies are available. By using optimized slides and improved working protocols for metabolite extraction in mass spectrometry, it may be possible in the future to reliably combine both methods.

Outlook

At this time the *cryoWriter* offers various possibilities for exciting new experiments, projects, further developments and extensions. The *climateJet*, for example, represents an interesting new possibility to extend and improve the sample preparation. For instance, the lossless cryo-EM grid preparation for single cell lysates could be improved. In this case, no sample is re-aspirated and it is therefore difficult to obtain ice of the desired thickness and quality. However, with a controlled injection of surfactants, an attempt could be made to use the Marangoni effect to thin the sample. Nevertheless, the main objective should be to first systematically test many surfactants in order to create a database that can be accessed when needed. This would allow a fast and efficient response to problems in the future, which would increase the chances for successful sample preparation. There are also many interesting applications for the magnetic trap. Recently, a master student in our laboratory used it to extract commercially available full-length LRRK2 from a storage buffer with high glycerol content and prepare grids for cryo-EM. Preliminary results look

quite promising, and a medium-high resolution structure at 10.2 Å, obtained from a data set from an FEI Talos equipped with a Ceta CMOS camera, suggests that the protein is intact [Zimmermann 2020]. Figure 1 shows the obtained density. Data acquisition on a better microscope with a direct electron detector is now necessary to validate that the protein has been successfully isolated and to check whether a high-resolution structure can be obtained.

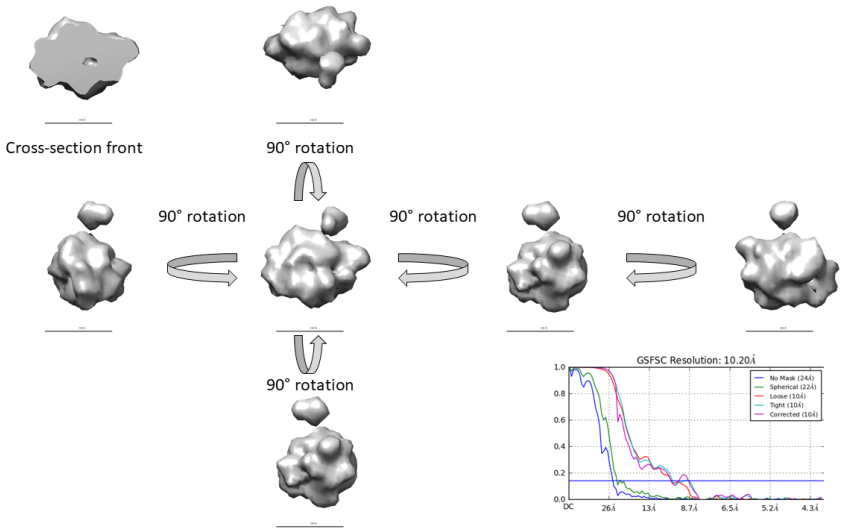

Figure 1: Obtained density of full-length LRRK2 at a resolution of 10.2 Å. The two monomers and the central cavity are visible in the cross-section. The small density on the surface of the protein is caused by the FAB fragment. Scale bar: 10 nm. The image was adopted from [Zimmermann 2020].

In addition to commercially available proteins, the purification and preparation of sensitive, rare or difficult, but medically relevant proteins is of course extremely exciting, since these proteins often cannot be properly expressed, isolated or prepared by other methods. Another obvious possibility is to combine the magnetic trap with the single-cell lysis module. Theoretically, there would already be enough copies of highly expressed proteins in a single cell to perform a single particle analysis. If this could be realized, it would then be possible to study conformational changes of proteins from cells lysed under different conditions. However, this requires first a modification of the *cryoWriter* setup since the magnetic trap cannot be placed over the cell incubator at the moment. Another exciting approach would be integrating a new module that enables the combination of the *cryoWriter* with cryo-FIB milling and CLEM. This would allow us first to vitrify cells grown on gold grids, dissect them by FIB milling, and examine them by CLEM. Together with advanced microfluidic designs for controlled cell growth and the blotting-free sample preparation of the

cryoWriter, this would create a new valuable tool for the examination of single cells and cell structures. In conclusion, it can be said that all techniques presented use parts of the *cryoWriter* and, therefore, all benefit from improvements in the setup. For this reason, the design should be constantly refined in the future, even if this does not directly lead to completely new possibilities. This could be increased speed, easier handling, or improved automation. The latter two points could also help ensure that less experienced users can use the setup for their research. Although there is room for improvement since many of the difficulties arise from the fact that the setup has grown over a long period of time and new things have been added bit by bit, a second prototype is now being planned. This has the great advantage that the required functions are already known from the beginning and can therefore be considered directly in the planning phase. Combined with the experience gained with the current setup, this will help make the new version much more compact, user-friendly, efficient, and versatile. For example, as mentioned above, the magnetic trap can then be placed above the cell incubator. It will also reduce distances, reposition parts that are difficult to access, eliminate potential crash risks, and simplify alignment. This second version of the *cryoWriter* also represents the first step in commercialization, which could eventually lead to a breakthrough in microfluidic sample preparation, as presented in this thesis.

A. *cryoWriter* setup

In the following section the most important parts of the *cryoWriter* setup are shown which are referred to throughout the thesis.

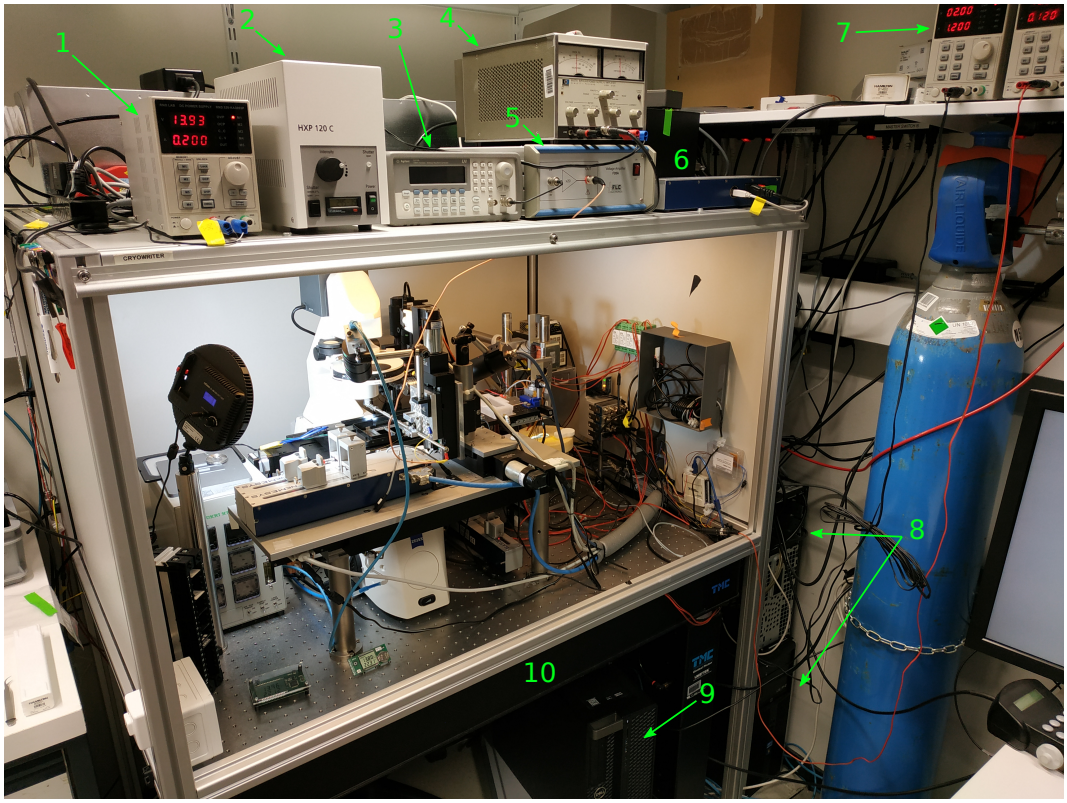

Figure 1: Overview of the *cryoWriter* setup

1. Labview controlled PSU. RND 320-KA3005P. Used together with resistance wire (RD 100/0,1) to keep humidifier at constant temperature.

2. Lighting unit for fluorescent microscope. ZEISS HXP 120 C.

3. Function generator for cell lysis. Agilent 33220A.

4. PSU for driving the magnets of the magnetic trap. HP 6827A.

5. Single channel high voltage linear amplifier. FLC Electronic F20A. Used in combination with 3) for cell lysis.

6. Controllers for motorized stages. Cetoni neMESYS pump and Prior Scientific.

7. 2 Labview controlled PSU. RND 320-KA3005P. One controls the peltier element of the sample holder, one controls the temperature of the ethane cup.

8. Watercooling systems for the temperature block of the climate jet and dew point stage.

9. Workstation.

10. Optical table. TMC Gimbal Piston + TMC CleanTop

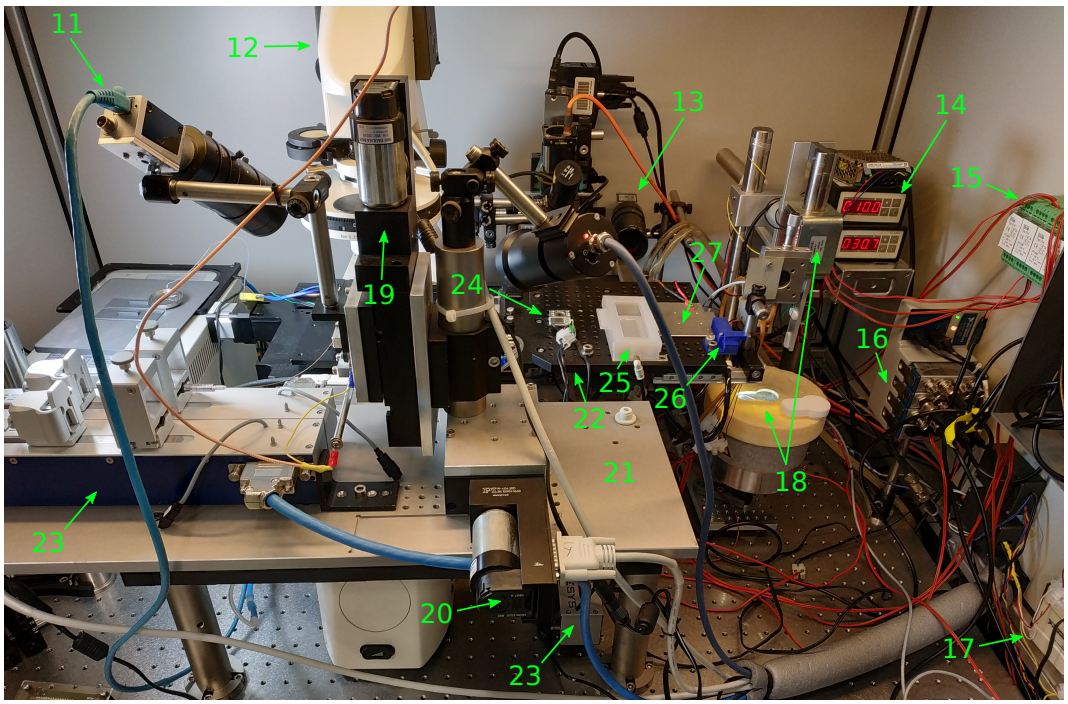

Figure 2: Inside view of the *cryoWriter* setup

11. Camera. Basler acA640-90gm.

12. Inverted microscope. Zeiss Axiovert 200.

13. Camera. Basler acA640-90gm.

14. 2 Peltier Controllers. Cooltronic TC3212. Controls the peltier element of the temperature block of the *climateJet* and dew point stage.

15. 4 Analog transmitters for Pt1000. LKM214.

16. cDAQ-9174 with NI 9402, NI 9234, NI 9215, NI 9269.

17. LV card. NI USB-6009.

18. Ethane cup and plunge freeze mechanism.

19. Z-Axis. PI M-404.2PD.

20. Y-Axis. PI M-404.2PD.

21. X-Axis. PI M-414.3PD.

22. XY-Stage. Prior Scientific H117EIL5.

23. High-precision syringe pump. Cetoni neMESYS.

24. Temperature controlled sample holder.

25. Argon chamber for cell slide spotting.

26. Outlet of *climateJet*

27. Dew point stage.

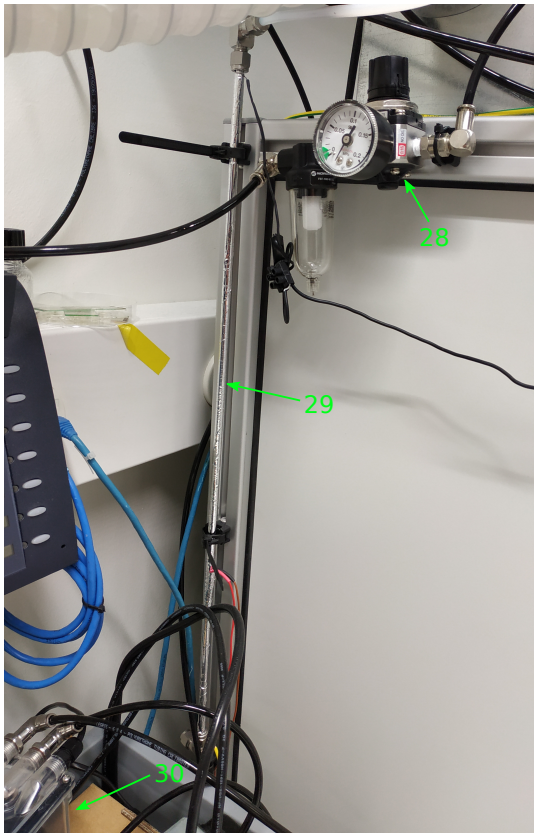

Figure 3: Side view of the *cryoWriter* setup

28. Regulator SRH3000-01 with filter for *climateJet*.

29. Shell and tube moisture exchanger MH-110-24S-2 for *climateJet*.

30. Watercooling pump for tips of the magnetic trap.

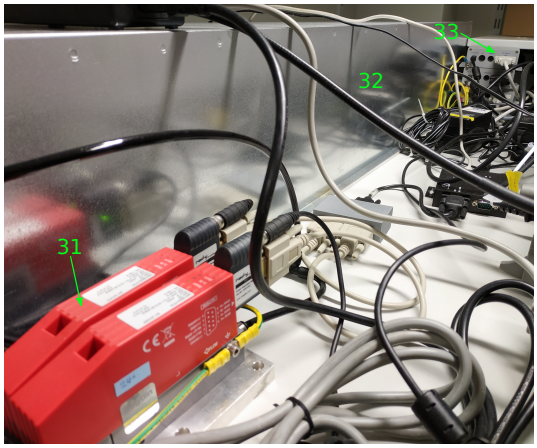

Figure 4: Top view of the *cryoWriter* setup

31. Mass flow controllers Voegtlin GSC-B9SA-FF23 for *climateJet*.
32. Ventilation system.
33. Mercury motor controllers C-863.

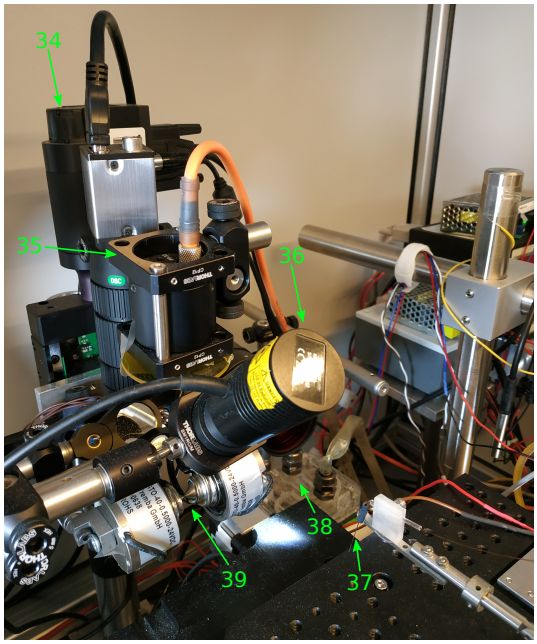

Figure 5: Close-up view

34. Z-Axis. PI M-404.2PD.
35. Camera and LED light for the operation of the magnetic trap.

36. UV LED. Thorlabs M365LP1c.For photocleavage.

37. Capillary for liquid handling. New Objective Picotip.

38. Temperature control block of *climateJet*.

39. Magnetic trap.

List of Abbreviations

2D, 3D	2-dimensional, 3-dimensional
ATP	Adenosine triphosphate
CCD	Charge-coupled device
CE	Collision energy
CLEM	Correlative light-electron microscopy
CMC	Critical micelle concentration
CMOS	Complementary metaloxidesemiconductor
COC	Cyclo-olefin copolymer
cryo-EM	Cryogenic electron microscopy
CTF	Contrast transfer function
DED	Direct electron detector
DESI	Desorption electrospray ionization
DP	Dew point
DSP	Direct sampling probe
EASI	Easy ambient sonic-spray ionization
EM	Electron microscopy
ESI	Electrospray ionization
FAB	Antigen-binding fragment
FEG	Field emission gun
FIB	Focused ion beam
FPPA	Forward phase protein array
FSC	Fourier shell correlation
GAPDH	Glyceraldehyde 3-phosphate dehydrogenase
GIF	Gatan Imaging Filter
GUI	Graphical user interface
HEK	Human embryonic kidney
HEPES	4-(2-hydroxyethyl)-1-piperazineethanesulfonic acid
HPF	High pressure freeze
HPLC	High-performance liquid chromatography
ITO	Indium tin oxide
LAESI	Laser ablation electrospray ionization
LC	Liquid chromatography
LDIDD	Laser desorption/ionization droplet delivery
LED	Light-emitting diode
LUHMES	Lund human mesencephalic
LLME	Liquid-liquid microextraction
MALDI	Matrix-assisted laser desorption/ionization
MRM	Multi reaction monitoring
MS	Mass spectrometry
NCC	Normalized cross correlation

NHS	N-Hydroxysuccinimide
NMR	Nuclear magnetic resonance
NS-EM	Negative stain TEM
OG	Octyl glucoside
PBS	Phosphate-buffered saline
PCR	Polymerase chain reaction
PDB	Protein Data Bank
PDMS	Polydimethylsiloxane
PEEK	Polyether ether ketone
PEG	Polyethylene glycol
PESI	Probe electrospray ionization
PID	Proportionalintegralderivative
PLL	Poly-L-lysine
PSF	Point spread function
PTFE	Polytetrafluoroethylene
RH	Relative humidity
RMSD	Root-mean-square deviation
RPPA	Reverse-Phase Protein Arrays
SCL	Single-cell lysis
SCP	Surface-coated probe
SIMS	Secondary ion mass spectrometry
SLME	Solid-liquid microextraction
SNR	Signal-to-noise ratio
SPA	Single Particle Analysis
TEM	Transmission electron microscopy
TLC	Thin-layer chromatography
TMV	Tobacco mosaic virus
TTL	Transistortransistor logic
UV	Ultraviolet
XRC	X-ray crystallography

List of symbols

a	Radius droplet, m
d	Cutoff distance, m
D	Diffusion coefficient, $\mathrm{m^2\,s^{-1}}$
E	Electric field, $\mathrm{V\,m^{-1}}$
F_m	Magnetic force, N
g	Gravitational acceleration, $\mathrm{m\,s^{-2}}$
ΔG	Excess free energy per unit area, $\mathrm{J\,m^{-2}}$
h	Height droplet, m
H	Magnetic field strength, $\mathrm{A\,m^{-1}}$
h_c	Critical height, m
h_r	Rupture height, m
l	Correlation length for the hydrophobic interaction, m
M_s	Saturation magnetization, $\mathrm{A\,m^{-1}}$
q	Number of dimensions
S	Spreading coefficient, $\mathrm{N\,m^{-1}}$
t	Time, s
V	Volume droplet/particle, $\mathrm{m^3}$
γ_{lg}	Surface tension liquid-gas, $\mathrm{N\,m^{-1}}$
γ_{sg}	Surface tension solid-gas, $\mathrm{N\,m^{-1}}$
γ_{sl}	Surface tension solid-liquid, $\mathrm{N\,m^{-1}}$
θ_c	Contact angle, $^\circ$
γ_c	Capillary length, m
μ_0	Magnetic constant, $\mathrm{N\,A^{-2}}$
Π	Disjoining pressure, $\mathrm{N\,m^{-2}}$
ρ	Density, $\mathrm{kg\,m^{-3}}$

List of Figures

1.1. Negative Staining EM 6
1.2. cryo-EM 7
1.3. *cryoWriter* - Grid Preparation 11
1.4. Sample Purification Using Magnetic Trap 12
1.5. Drop of Liquid Deposited on a Hydrophilic Surface 14
1.6. Variation of Φ_h 17
1.7. Thin Film Rupture 18
1.8. Proteins in a Vitrified Ice Layer 22
1.9. Combination of the SCL Module With MS and RPPA 28
2.1. Principles of TEM Grid Preparation and Comparison Between the Classical and a Microfluidic Approach 35
2.2. Overview of the cryoWriter Setup 47
2.3. Typical Results for NS Grids Prepared Using the cryoWriter Setup . 48
2.4. Typical Results for cryo-EM Grids Prepared Using the cryoWriter Setup 49
2.5. Systematic Changes and Artifacts Observed When The cryoWriter Set-up Was Used 51
2.6. Single Cell Visual Proteomics Using The cryoWriter Set-up 52
3.1. Overview of the *climateJet* Module 59
3.2. Gas Flow Characteristics of the Outlet 61
3.3. Comparison of Vitreous Ice With and Without Injection of OG . . . 62
3.4. Efficiency Scores of Different Grid Preparations 63
3.5. Comparison of Ice and Particle Density 64
S1. GUI *climateJet* 68
1. Schematic Work-Flow for Microfluidic Protein Isolation and cryo-EM Grid Preparation 74

2. Sample Quality and Data-Collection 77
3. 3D Reconstruction of the Human 20S Proteasome 79
S1. Image of the Magnetic Trap Set-up 84
S2. Finite Element Simulation of the Magnetic Field Generated by the Electromagnetic Trap System 86
S3. Illustration of the Magnetic Particle-Plug Enclosed Between Two 6 nL Air Bubbles 86
S4. Resolution Estimation for the 20S Proteasome and TMV 88
S5. Local Resolution Map for the Human 20S Proteasome 89
S6. Testing Overfitting of 20S Proteasome Model 91
S7. Testing Overfitting of TMV Model 91
S8. 3D Reconstruction of TMV 92
1. Workflow Correlative Analysis 95
2. Assay Development 100
3. Single Cell RPPA Dot-blot 101
4. Correlative Single-Cell Analysis 102
S1. COC Slides 105
S2. 3D Printed Polypropylen Cap 105
S3. Mass Spectra 106
1. Full-Length LRRK2 109
1. Overview *cryo Writer* Setup 111
2. Inside View *cryo Writer* Setup 112
3. Side View *cryo Writer* Setup 113
4. Top View *cryo Writer* Setup 114
5. Close-up View 114

List of Tables

S1. Materials list of the *climateJet*. 66

S2. Data collection parameters. 67

S3. Image processing workflow in cryoSPARC 67

S4. Other processing parameters and values. 68

S5. Input parameters for cryoEF used to calculate the efficiency score. . 68

S1. Parts list of the magnetic trap setup. 85

S2. Data collection parameters. 87

S3. Image processing parameters used for 20S proteasome structure determination with RELION3. 87

S4. Image processing parameters used for helical structure determination of TMV with RELION3. 88

S5. 20S proteasome model validation statistics. 90

S6. TMV model validation statistics. 90

References

[Adams *et al.* 2010] Paul D. Adams, Pavel V. Afonine, Gábor Bunkóczi, Vincent B. Chen, Ian W. Davis, Nathaniel Echols, Jeffrey J. Headd, Li-Wei Hung, Gary J. Kapral, Ralf W. Grosse-Kunstleve, Airlie J. McCoy, Nigel W. Moriarty, Robert Oeffner, Randy J. Read, David C. Richardson, Jane S. Richardson, Thomas C. Terwilliger and Peter H. Zwart. *PHENIX: a comprehensive Python-based system for macromolecular structure solution.* Acta Crystallographica Section D Biological Crystallography, vol. 66, no. 2, pages 213–221, jan 2010. (Cited on page 82.)

[Altschuler & Wu 2010] Steven J. Altschuler and Lani F. Wu. *Cellular Heterogeneity: Do Differences Make a Difference?* Cell, vol. 141, no. 4, pages 559–563, may 2010. (Cited on page 24.)

[Armstrong *et al.* 2019] Maxim Armstrong, Bong-Gyoon Han, Salvador Gomez, John Turner, Daniel A. Fletcher and Robert M. Glaeser. *Microscale Fluid Behavior during Cryo-EM Sample Blotting.* Biophysical Journal, dec 2019. (Cited on page 7.)

[Arnold *et al.* 2016] Stefan A. Arnold, Stefan Albiez, Nadia Opara, Mohamed Chami, Claudio Schmidli, Andrej Bieri, Celestino Padeste, Henning Stahlberg and Thomas Braun. *Total Sample Conditioning and Preparation of Nanoliter Volumes for Electron Microscopy.* ACS Nano, vol. 10, no. 5, pages 4981–4988, apr 2016. (Cited on pages 10, 34, 35, 43, 45, 46, 48, 52, 53, 57, 73, 78, 96 and 98.)

[Arnold *et al.* 2017] Stefan A. Arnold, Stefan Albiez, Andrej Bieri, Anastasia Syntychaki, Ricardo Adaixo, Robert A. McLeod, Kenneth N. Goldie, Henning Stahlberg and Thomas Braun. *Blotting-free and lossless cryo-electron microscopy grid preparation from nanoliter-sized protein samples and single-cell extracts.* Journal of Structural Biology, vol. 197, no. 3, pages 220–226, mar 2017. (Cited on pages 10, 19, 34, 45, 50, 52, 57, 73, 76, 78 and 81.)

[Arnold *et al.* 2018] Stefan Alexander Arnold, Thomas Braun and Henning Stahlberg. *Lossless cryo-grid preparation stage for high-resolution electron microscopy*, July 26 2018. US Patent App. 15/742,532. (Cited on page 73.)

[Arnold 2017] Stefan Alexander Arnold. *Nanoliter sample preparation for electron microscopy and single-cell analysis.* PhD thesis, University of Basel, 2017. (Cited on pages 69 and 97.)

[Asarnow *et al.* 2019] Daniel Asarnow, Eugene Palovcak and Yifan Cheng. *asarnow/pyem: UCSF pyem v0.5*, 2019. (Cited on page 59.)

[Ashtiani *et al.* 2018] Dariush Ashtiani, Hari Venugopal, Matthew Belousoff, Bradley Spicer, Johnson Mak, Adrian Neild and Alex de Marco. *Delivery of femtolitre droplets using surface acoustic wave based atomisation for cryo-EM grid preparation.* Journal of Structural Biology, vol. 203, no. 2, pages 94–101, aug 2018. (Cited on pages 9 and 57.)

[Baker & Rubinstein 2010] Lindsay A Baker and John L Rubinstein. *Radiation damage in electron cryomicroscopy.* Methods in enzymology, vol. 481, pages 371–388, 2010. (Cited on page 33.)

[Beck *et al.* 2009] Martin Beck, Johan A. Malmstroem, Vinzenz Lange, Alexander Schmidt, Eric W. Deutsch and Ruedi Aebersold. *Visual proteomics of the human pathogen Leptospira interrogans.* Nature Methods, vol. 6, no. 11, page 817U55, Nov 2009. Citation Key: beck:2009aa tex.address: MACMILLAN BUILDING, 4 CRINAN ST, LONDON N1 9XW, ENGLAND tex.bdsk-url-2: https://doi.org/10.1038/NMETH.1390 tex.date-added: 2018-08-17 13:31:28 +0200 tex.date-modified: 2019-10-02 22:44:42 +0200 tex.publisher: NATURE PUBLISHING GROUP tex.times-cited: 90 tex.wok-uid: WOS:000271247200015. (Cited on page 94.)

[Bedanta & Kleemann 2008] Subhankar Bedanta and Wolfgang Kleemann. *Supermagnetism.* Journal of Physics D: Applied Physics, vol. 42, no. 1, page 013001, dec 2008. (Cited on page 12.)

[Benjamin *et al.* 2016] Christopher J. Benjamin, Kyle J. Wright, Scott C. Bolton, Seok-Hee Hyun, Kyle Krynski, Mahima Grover, Guimei Yu, Fei Guo, Tamara L. Kinzer-Ursem, Wen Jiang and David H. Thompson. *Selective Capture of Histidine-tagged Proteins from Cell Lysates Using TEM grids Modified with NTA-Graphene Oxide.* Scientific Reports, vol. 6, no. 1, oct 2016. (Cited on page 24.)

[Berriman & Unwin 1994] John Berriman and Nigel Unwin. *Analysis of transient structures by cryo-microscopy combined with rapid mixing of spray droplets.* Ultramicroscopy, vol. 56, no. 4, pages 241–252, dec 1994. (Cited on pages 9 and 57.)

[Bhardwaj *et al.* 2009] Rajneesh Bhardwaj, Xiaohua Fang and Daniel Attinger. *Pattern formation during the evaporation of a colloidal nanoliter drop: a numerical and experimental study.* New Journal of Physics, vol. 11, no. 7, page 075020, jul 2009. (Cited on page 73.)

[Biyani *et al.* 2017] Nikhil Biyani, Ricardo D. Righetto, Robert McLeod, Daniel Caujolle-Bert, Daniel Castano-Diez, Kenneth N. Goldie and Henning Stahlberg. *Focus: The interface between data collection and data processing*

in cryo-EM. Journal of Structural Biology, vol. 198, no. 2, pages 124–133, may 2017. (Cited on page 81.)

[Boellner & Becker 2015] Stefanie Boellner and Karl-Friedrich Becker. *Reverse Phase Protein Arrays—Quantitative Assessment of Multiple Biomarkers in Biopsies for Clinical Use.* Microarrays, vol. 4, no. 2, pages 98–114, mar 2015. (Cited on page 27.)

[Brenner & Horne 1959] S. Brenner and R.W. Horne. *A negative staining method for high resolution electron microscopy of viruses.* Biochimica et Biophysica Acta, vol. 34, pages 103–110, July 1959. (Cited on page 33.)

[Brullot *et al.* 2012] W. Brullot, N.K. Reddy, J. Wouters, V.K. Valev, B. Goderis, J. Vermant and T. Verbiest. *Versatile ferrofluids based on polyethylene glycol coated iron oxide nanoparticles.* Journal of Magnetism and Magnetic Materials, vol. 324, no. 11, pages 1919–1925, jun 2012. (Cited on page 12.)

[Campbell *et al.* 2012] Melody G. Campbell, Anchi Cheng, Axel F. Brilot, Arne Moeller, Dmitry Lyumkis, David Veesler, Junhua Pan, Stephen C. Harrison, Clinton S. Potter, Bridget Carragher and Nikolaus Grigorieff. *Movies of Ice-Embedded Particles Enhance Resolution in Electron Cryo-Microscopy.* Structure, vol. 20, no. 11, pages 1823–1828, nov 2012. (Cited on page 33.)

[Cardone *et al.* 2013] Giovanni Cardone, J. Bernard Heymann and Alasdair C. Steven. *One number does not fit all: Mapping local variations in resolution in cryo-EM reconstructions.* Journal of Structural Biology, vol. 184, no. 2, pages 226–236, nov 2013. (Cited on page 88.)

[Carlo & Harris 2011] Sacha De Carlo and J. Robin Harris. *Negative staining and cryo-negative staining of macromolecules and viruses for TEM.* Micron, vol. 42, no. 2, pages 117–131, feb 2011. (Cited on page 33.)

[Castro-Hartmann *et al.* 2013] P. Castro-Hartmann, G. Heck, J. M. Eltit, P. Fawcett and M. Samso. *The ArrayGrid: a methodology for applying multiple samples to a single TEM specimen grid.* Ultramicroscopy, vol. 135, pages 105–12, dec 2013. (Cited on page 8.)

[chen Bai *et al.* 2015] Xiao chen Bai, Greg McMullan and Sjors H.W Scheres. *How cryo-EM is revolutionizing structural biology.* Trends in Biochemical Sciences, vol. 40, no. 1, pages 49–57, jan 2015. (Cited on page 32.)

[Chen *et al.* 2013] Shaoxia Chen, Greg McMullan, Abdul R. Faruqi, Garib N. Murshudov, Judith M. Short, Sjors H.W. W Scheres and Richard Henderson. *High-resolution noise substitution to measure overfitting and validate resolution in 3D structure determination by single particle electron cryomicroscopy.*

Ultramicroscopy, vol. 135, no. 0, pages 24–35, dec 2013. (Cited on page 88.)

[Chen *et al.* 2015] Bo Chen, Sandip Kaledhonkar, Ming Sun, Bingxin Shen, Zonghuan Lu, David Barnard, Toh-Ming Lu, Ruben L. Gonzalez and Joachim Frank. *Structural Dynamics of Ribosome Subunit Association Studied by Mixing-Spraying Time-Resolved Cryogenic Electron Microscopy.* Structure, vol. 23, no. 6, pages 1097–1105, jun 2015. (Cited on pages 9 and 57.)

[Chen *et al.* 2016] Fengming Chen, Luyao Lin, Jie Zhang, Ziyi He, Katsumi Uchiyama and Jin-Ming Lin. *Single-Cell Analysis Using Drop-on-Demand Inkjet Printing and Probe Electrospray Ionization Mass Spectrometry.* Analytical Chemistry, vol. 88, no. 8, page 43544360, apr 2016. (Cited on page 26.)

[Cheng *et al.* 2015] Yifan Cheng, Nikolaus Grigorieff, Pawel A. Penczek and Thomas Walz. *A Primer to Single-Particle Cryo-Electron Microscopy.* Cell, vol. 161, no. 3, pages 438–449, apr 2015. (Cited on page 33.)

[Cheng 2018] Yifan Cheng. *Single-particle cryo-EM-How did it get here and where will it go.* Science, vol. 361, no. 6405, pages 876–+, August 2018. (Cited on page 72.)

[Crewe *et al.* 1968] A. V. Crewe, D. N. Eggenberger, J. Wall and L. M. Welter. *Electron Gun Using a Field Emission Source.* Review of Scientific Instruments, vol. 39, no. 4, pages 576–583, apr 1968. (Cited on page 33.)

[Cromm & Crews 2017] Philipp M. Cromm and Craig M. Crews. *The Proteasome in Modern Drug Discovery: Second Life of a Highly Valuable Drug Target.* ACS Central Science, vol. 3, no. 8, pages 830–838, aug 2017. (Cited on page 73.)

[Crucifix *et al.* 2004] Corinne Crucifix, Muriel Uhring and Patrick Schultz. *Immobilization of biotinylated DNA on 2-D streptavidin crystals.* Journal of Structural Biology, vol. 146, no. 3, pages 441–451, jun 2004. (Cited on page 24.)

[Cyrklaff *et al.* 1990] Marek Cyrklaff, Marc Adrian and Jacques Dubochet. *Evaporation during preparation of unsupported thin vitrified aqueous layers for cryo-electron microscopy.* Journal of Electron Microscopy Technique, vol. 16, no. 4, pages 351–355, dec 1990. (Cited on page 19.)

[da Fonseca & Morris 2015] Paula C.A. da Fonseca and Edward P. Morris. *Cryo-EM reveals the conformation of a substrate analogue in the human 20S proteasome core.* Nature Communications, vol. 6, no. 1, jul 2015. (Cited on pages 76, 78 and 89.)

[Dandey *et al.* 2018] Venkata P. Dandey, Hui Wei, Zhening Zhang, Yong Zi Tan, Priyamvada Acharya, Edward T. Eng, William J. Rice, Peter A. Kahn, Clin-

ton S. Potter and Bridget Carragher. *Spotiton: New features and applications.* Journal of Structural Biology, vol. 202, no. 2, pages 161–169, may 2018. (Cited on pages 9, 57 and 78.)

[Deng *et al.* 2015] Jiewei Deng, Yunyun Yang, Mingzhi Xu, Xiaowei Wang, Li Lin, Zhong-Ping Yao and Tiangang Luan. *Surface-Coated Probe Nanoelectrospray Ionization Mass Spectrometry for Analysis of Target Compounds in Individual Small Organisms.* Analytical Chemistry, vol. 87, no. 19, page 99239930, October 2015. (Cited on page 26.)

[Derrick 1973] K. S. Derrick. *Quantitative assay for plant viruses using serologically specific electron microscopy.* Virology, vol. 56, no. 2, pages 652–653, dec 1973. (Cited on page 78.)

[Dubochet *et al.* 1988] Jacques Dubochet, Marc Adrian, Jiin-Ju Chang, Jean-Claude Homo, Jean Lepault, Alasdair W. McDowall and Patrick Schultz. *Cryo-electron microscopy of vitrified specimens.* Quarterly Reviews of Biophysics, vol. 21, no. 2, pages 129–228, may 1988. (Cited on pages 3, 6, 32, 56, 72 and 73.)

[Emsley *et al.* 2010] Paul Emsley, Bernhard Lohkamp, William G. Scott and Kevin Cowtan. *Features and Development of Coot.* Acta Crystallographica Section D Biological Crystallography, vol. 66, no. 4, pages 486–501, mar 2010. (Cited on page 82.)

[Engel 2009] Andreas Engel. Assessing biological samples with scanning probes, volume 96. Springer Berlin Heidelberg, Berlin, Heidelberg, nov 2009. (Cited on page 34.)

[Evers *et al.* 2019] Tom M. J. Evers, Mazène Hochane, Sander J. Tans, Ron M. A. Heeren, Stefan Semrau, Peter Nemes and Alireza Mashaghi. *Deciphering Metabolic Heterogeneity by Single-Cell Analysis.* Analytical Chemistry, vol. 91, no. 21, pages 13314–13323, sep 2019. (Cited on page 25.)

[Feng *et al.* 2017] X. Feng, Z. Fu, S. Kaledhonkar, Y. Jia, B. Shah, A. Jin, Z. Liu, M. Sun, B. Chen, R. A. Grassucci, Y. Ren, H. Jiang, J. Frank and Q. Lin. *A fast and effective microfluidic spraying-plunging method for high-resolution single-particle cryo-EM.* Structure, vol. 25, no. 4, pages 663–670 e3, 2017. (Cited on pages 9, 57 and 78.)

[Ferreira *et al.* 2012] C. R. Ferreira, L. S. Eberlin, J. E. Hallett and R. G. Cooks. *Single oocyte and single embryo lipid analysis by desorption electrospray ionization mass spectrometry.* Journal of Mass Spectrometry, vol. 47, no. 1, pages 29–33, jan 2012. (Cited on page 27.)

[Frank 1975] Joachim Frank. *Averaging of low exposure electron micrographs of non-periodic objects.* Ultramicroscopy, vol. 1, no. 2, pages 159–162, jan 1975. (Cited on page 72.)

[Frederik *et al.* 1989] P. M. Frederik, M. C. A. Stuart, P. H. H. Bomans and W. M. Busing. *Phospholipid, Nature's own slide and cover slip for cryo-electron microscopy.* Journal of Microscopy, vol. 153, no. 1, pages 81–92, jan 1989. (Cited on page 23.)

[Förster *et al.* 2010] Friedrich Förster, Bong-Gyoon Han and Martin Beck. Visual proteomics, volume 483. Elsevier, 1 édition, 2010. Citation Key: forster:2010aa tex.date-added: 2018-03-15 08:56:40 +0000 tex.date-modified: 2018-03-29 14:43:55 +0000 tex.type: Book. (Cited on page 94.)

[Giss *et al.* 2013] Dominic Giss, Simon Kemmerling, Venkata P. Dandey, Henning Stahlberg and Thomas Braun. *Microfluidics to isolate untagged proteins from cell extracts for visual analysis by electron microscopy.* In 17th International Conference on Miniaturized Systems for Chemistry and Life Sciences, 2013. (Cited on page 75.)

[Giss *et al.* 2014] Dominic Giss, Simon Kemmerling, Venkata Dandey, Henning Stahlberg and Thomas Braun. *Exploring the Interactome: Microfluidic Isolation of Proteins and Interacting Partners for Quantitative Analysis by Electron Microscopy.* Analytical Chemistry, vol. 86, no. 10, pages 4680–4687, apr 2014. (Cited on pages 54, 73 and 75.)

[Glaeser & Han 2017] Robert M. Glaeser and Bong-Gyoon Han. *Opinion: hazards faced by macromolecules when confined to thin aqueous films.* Biophysics Reports, vol. 3, no. 1-3, pages 1–7, jul 2017. (Cited on page 21.)

[Glaeser *et al.* 2016] Robert M. Glaeser, Bong-Gyoon Han, Roseann Csencsits, Alison Killilea, Arto Pulk and Jamie H.D. Cate. *Factors that Influence the Formation and Stability of Thin, Cryo-EM Specimens.* Biophysical Journal, vol. 110, no. 4, pages 749–755, feb 2016. (Cited on pages 10, 15, 17, 18, 57 and 73.)

[Glaeser 2016] Robert M Glaeser. *How good can cryo-EM become?* Nature Methods, vol. 13, no. 1, pages 28–32, jan 2016. (Cited on pages 23, 34 and 73.)

[Glaeser 2018] Robert M. Glaeser. *Proteins, interfaces, and cryo-EM grids.* Current Opinion in Colloid & Interface Science, vol. 34, pages 1–8, mar 2018. (Cited on pages 19, 20, 21, 23 and 24.)

[Gong *et al.* 2014] Xiaoyun Gong, Yaoyao Zhao, Shaoqing Cai, Shujie Fu, Chengdui Yang, Sichun Zhang and Xinrong Zhang. *Single Cell Analysis with Probe ESI-Mass Spectrometry: Detection of Metabolites at Cellular and Subcellular*

Levels. Analytical Chemistry, vol. 86, no. 8, pages 3809–3816, mar 2014. (Cited on page 26.)

[Gowda & Djukovic 2014] G. A. Nagana Gowda and Danijel Djukovic. *Overview of Mass Spectrometry-Based Metabolomics: Opportunities and Challenges*. In Methods in Molecular Biology, pages 3–12. Springer New York, 2014. (Cited on page 25.)

[Grigorieff 2007] Nikolaus Grigorieff. *FREALIGN: High-resolution refinement of single particle structures*. Journal of Structural Biology, vol. 157, no. 1, pages 117–125, jan 2007. (Cited on page 33.)

[Han *et al.* 2012] Bong-Gyoon Han, Ross W. Walton, Amos Song, Peter Hwu, Milton T. Stubbs, Steven M. Yannone, Pablo Arbeláez, Ming Dong and Robert M. Glaeser. *Electron microscopy of biotinylated protein complexes bound to streptavidin monolayer crystals*. Journal of Structural Biology, vol. 180, no. 1, pages 249–253, oct 2012. (Cited on page 23.)

[Harauz & van Heel 1986] George Harauz and Marin van Heel. *Exact filters for general geometry three dimensional reconstruction*. Optik, vol. 78, no. 4, pages 146–156, 1986. (Cited on page 87.)

[He & Scheres 2017] Shaoda He and Sjors H.W. Scheres. *Helical reconstruction in RELION*. Journal of Structural Biology, vol. 198, no. 3, pages 163–176, jun 2017. (Cited on page 82.)

[Heel & Frank 1981] Marin Van Heel and Joachim Frank. *Use of multivariate statistics in analysing the images of biological macromolecules*. Ultramicroscopy, vol. 6, no. 2, pages 187–194, jan 1981. (Cited on page 72.)

[Jain *et al.* 2012] Tilak Jain, Patrick Sheehan, John Crum, Bridget Carragher and Clinton S. Potter. *Spotiton: A prototype for an integrated inkjet dispense and vitrification system for cryo-TEM*. Journal of Structural Biology, vol. 179, no. 1, pages 68–75, jul 2012. (Cited on pages 8, 9 and 57.)

[Kelly *et al.* 2008a] D. F. Kelly, D. Dukovski and T. Walz. *Monolayer purification: A rapid method for isolating protein complexes for single-particle electron microscopy*. Proceedings of the National Academy of Sciences, vol. 105, no. 12, pages 4703–4708, mar 2008. (Cited on page 24.)

[Kelly *et al.* 2008b] Deborah F. Kelly, Priyanka D. Abeyrathne, Danijela Dukovski and Thomas Walz. *The Affinity Grid: A Pre-fabricated EM Grid for Monolayer Purification*. Journal of Molecular Biology, vol. 382, no. 2, pages 423–433, oct 2008. (Cited on page 78.)

[Kelly *et al.* 2010] Deborah F. Kelly, Danijela Dukovski and Thomas Walz. *Strategy for the Use of Affinity Grids to Prepare Non-His-Tagged Macromolecular Complexes for Single-Particle Electron Microscopy.* Journal of Molecular Biology, vol. 400, no. 4, pages 675–681, jul 2010. (Cited on page 24.)

[Kemmerling *et al.* 2012] Simon Kemmerling, Jörg Ziegler, Gabriel Schweighauser, Stefan A. Arnold, Dominic Giss, Shirley A. Müller, Philippe Ringler, Kenneth N. Goldie, Nils Goedecke, Andreas Hierlemann, Henning Stahlberg, Andreas Engel and Thomas Braun. *Connecting* µ*-fluidics to electron microscopy.* Journal of Structural Biology, vol. 177, no. 1, pages 128–134, jan 2012. (Cited on pages 8, 34, 46 and 73.)

[Kemmerling *et al.* 2013] Simon Kemmerling, Stefan A. Arnold, Benjamin A. Bircher, Nora Sauter, Carlos Escobedo, Gregor Dernick, Andreas Hierlemann, Henning Stahlberg and Thomas Braun. *Single-cell lysis for visual analysis by electron microscopy.* Journal of Structural Biology, vol. 183, no. 3, pages 467–473, sep 2013. (Cited on pages 10, 24, 28, 34, 43, 45, 50, 52, 57, 78, 96, 98 and 100.)

[Kontziampasis *et al.* 2019] Dimitrios Kontziampasis, David P. Klebl, Matthew G. Iadanza, Charlotte A. Scarff, Florian Kopf, Frank Sobott, Diana C. F. Monteiro, Martin Trebbin, Stephen P. Muench and Howard D. White. *A cryo-EM grid preparation device for time-resolved structural studies.* IUCrJ, vol. 6, no. 6, pages 1024–1031, sep 2019. (Cited on pages 9 and 57.)

[Kuhlbrandt 2014] W. Kuhlbrandt. *The Resolution Revolution.* Science, vol. 343, no. 6178, pages 1443–1444, mar 2014. (Cited on pages 4, 32 and 72.)

[Lai & Wang 2017] Yin-Hung Lai and Yi-Sheng Wang. *Matrix-Assisted Laser Desorption/Ionization Mass Spectrometry: Mechanistic Studies and Methods for Improving the Structural Identification of Carbohydrates.* Mass Spectrometry, vol. 6, no. 3, pages S0072–S0072, 2017. (Cited on page 25.)

[Leaver-Fay *et al.* 2007] Andrew Leaver-Fay, Gary J. Kapral, Ian W. Davis, Jack Snoeyink, Jane S. Richardson, Jeremy N. Block, Laura W. Murray, Vincent B. Chen, III Arendall W. Bryan, Xueyi Wang and David C. Richardson. *MolProbity: all-atom contacts and structure validation for proteins and nucleic acids.* Nucleic Acids Research, vol. 35, no. suppl_2, pages W375–W383, 07 2007. (Cited on page 90.)

[Lee *et al.* 2012] Jinkee Lee, Amitesh Saha, Sabrina Montero Pancera, Andreas Kempter, Jens Rieger, Arijit Bose and Anubhav Tripathi. *Shear free and blotless cryo-TEM imaging: a new method for probing early evolution of nanostructures.* Langmuir, vol. 28, no. 9, pages 4043–4046, 2012. (Cited on page 9.)

[Lee *et al.* 2016] Jae Kyoo Lee, Erik T. Jansson, Hong Gil Nam and Richard N. Zare. *High-Resolution Live-Cell Imaging and Analysis by Laser Desorption/Ionization Droplet Delivery Mass Spectrometry.* Analytical Chemistry, vol. 88, no. 10, pages 5453–5461, may 2016. (Cited on page 27.)

[Leggett *et al.* 2005] David S. Leggett, Michael H. Glickman and Daniel Finley. Purification of proteasomes, proteasome subcomplexes, and proteasome-associated proteins from budding yeast, pages 057–070. Humana Press, Totowa, NJ, 2005. (Cited on page 80.)

[Lepault *et al.* 1983] J Lepault, F P Booy and J Dubochet. *Electron microscopy of frozen biological suspensions.* Journal of Microscopy, vol. 129, no. 1, pages 89–102, jan 1983. (Cited on pages 3, 32 and 56.)

[Li *et al.* 2013] Xueming Li, Paul Mooney, Shawn Zheng, Christopher R Booth, Michael B Braunfeld, Sander Gubbens, David A Agard and Yifan Cheng. *Electron counting and beam-induced motion correction enable near-atomic-resolution single-particle cryo-EM.* Nature Methods, vol. 10, no. 6, pages 584–590, may 2013. (Cited on page 33.)

[Liu *et al.* 2014] Yiqun Liu, Jialing Zhang, Honggang Nie, Chunxia Dong, Ze Li, Zhenggao Zheng, Yu Bai, Huwei Liu and Jindong Zhao. *Study on Variation of Lipids during Different Growth Phases of Living Cyanobacteria Using Easy Ambient Sonic-Spray Ionization Mass Spectrometry.* Analytical Chemistry, vol. 86, no. 14, pages 7096–7102, jun 2014. (Cited on page 27.)

[Lu *et al.* 2009] Zonghuan Lu, Tanvir R. Shaikh, David Barnard, Xing Meng, Hisham Mohamed, Aymen Yassin, Carmen A. Mannella, Rajendra K. Agrawal, Toh-Ming Lu and Terence Wagenknecht. *Monolithic microfluidic mixing–spraying devices for time-resolved cryo-electron microscopy.* Journal of Structural Biology, vol. 168, no. 3, pages 388–395, dec 2009. (Cited on pages 9 and 57.)

[Lu *et al.* 2014] Z. H. Lu, D. Barnard, T. R. Shaikh, X. Meng, C. A. Mannella, A. S. Yassin, R. K. Agrawal, T. Wagenknecht and T. M. Lu. *Gas-assisted annular microsprayer for sample preparation for time-resolved cryo-electron microscopy.* Journal of Micromechical Microengeneering, vol. 24, no. 11, 2014. (Cited on pages 9 and 57.)

[Lyumkis 2019] Dmitry Lyumkis. *Challenges and opportunities in cryo-EM single-particle analysis.* Journal of Biological Chemistry, vol. 294, no. 13, pages 5181–5197, feb 2019. (Cited on pages 3 and 56.)

[MacRitchie & Alexander 1963] F MacRitchie and A.E Alexander. *Kinetics of adsorption of proteins at interfaces. Part I. The role of bulk diffusion in ad-*

sorption. Journal of Colloid Science, vol. 18, no. 5, pages 453–457, jun 1963. (Cited on page 23.)

[Mastronarde 2005] David N. Mastronarde. *Automated electron microscope tomography using robust prediction of specimen movements.* Journal of Structural Biology, vol. 152, no. 1, pages 36–51, oct 2005. (Cited on page 81.)

[McLeod *et al.* 2017] Robert A. McLeod, Julia Kowal, Philippe Ringler and Henning Stahlberg. *Robust image alignment for cryogenic transmission electron microscopy.* Journal of Structural Biology, vol. 197, no. 3, pages 279–293, mar 2017. (Cited on page 33.)

[Milazzo *et al.* 2011] Anna-Clare Milazzo, Anchi Cheng, Arne Moeller, Dmitry Lyumkis, Erica Jacovetty, James Polukas, Mark H. Ellisman, Nguyen-Huu Xuong, Bridget Carragher and Clinton S. Potter. *Initial evaluation of a direct detection device detector for single particle cryo-electron microscopy.* Journal of Structural Biology, vol. 176, no. 3, pages 404–408, dec 2011. (Cited on page 33.)

[Mizuno *et al.* 2008] Hajime Mizuno, Naohiro Tsuyama, Takanori Harada and Tsutomu Masujima. *Live single-cell video-mass spectrometry for cellular and subcellular molecular detection and cell classification.* Journal of Mass Spectrometry, vol. 43, no. 12, pages 1692–1700, dec 2008. (Cited on page 26.)

[Morris & da Fonseca 2017] Edward P. Morris and Paula C. A. da Fonseca. *High-resolution cryo-EM proteasome structures in drug development.* Acta Crystallographica Section D Structural Biology, vol. D73, no. 6, pages 522–533, may 2017. (Cited on page 78.)

[Mukhitov *et al.* 2016] Nikita Mukhitov, John M. Spear, Scott M. Stagg and Michael G. Roper. *Interfacing Microfluidics with Negative Stain Transmission Electron Microscopy.* Analytical Chemistry, vol. 88, no. 1, pages 629–634, dec 2016. (Cited on page 8.)

[Mulligan *et al.* 2015] Sėan K. Mulligan, Jeffrey A. Speir, Ivan Razinkov, Anchi Cheng, John Crum, Tilak Jain, Erika Duggan, Er Liu, John P. Nolan, Bridget Carragher and Clinton S. Potter. *Multiplexed TEM Specimen Preparation and Analysis of Plasmonic Nanoparticles.* Microscopy and Microanalysis, vol. 21, no. 4, pages 1017–1025, jul 2015. (Cited on page 8.)

[Nakane *et al.* 2020] Takanori Nakane, Abhay Kotecha, Andrija Sente, Greg McMullan, Simonas Masiulis, Patricia M.G.E. Brown, Ioana T. Grigoras, Lina Malinauskaite, Tomas Malinauskas, Jonas Miehling, Lingbo Yu, Dimple Karia, Evgeniya V. Pechnikova, Erwin de Jong, Jeroen Keizer, Maarten

Bischoff, Jamie McCormack, Peter Tiemeijer, Steven W. Hardwick, Dimitri Y. Chirgadze, Garib Murshudov, A. Radu Aricescu and Sjors H.W. Scheres. *Single-particle cryo-EM at atomic resolution.* may 2020. (Cited on page 56.)

[Nakashima *et al.* 2016] Taiken Nakashima, Hiroshi Wada, Satoshi Morita, Rosa Erra-Balsells, Kenzo Hiraoka and Hiroshi Nonami. *Single-Cell Metabolite Profiling of Stalk and Glandular Cells of Intact Trichomes with Internal Electrode Capillary Pressure Probe Electrospray Ionization Mass Spectrometry.* Analytical Chemistry, vol. 88, no. 6, pages 3049–3057, feb 2016. (Cited on page 26.)

[Naydenova & Russo 2017] Katerina Naydenova and Christopher J. Russo. *Measuring the effects of particle orientation to improve the efficiency of electron cryomicroscopy.* Nature Communications, vol. 8, no. 1, sep 2017. (Cited on page 59.)

[Naydenova *et al.* 2020] Katerina Naydenova, Peipei Jia and Christopher J. Russo. *Cryo-EM with sub–1 Å specimen movement.* Science, vol. 370, no. 6513, pages 223–226, 2020. (Cited on page 8.)

[Newman *et al.* 2006] John R. S. Newman, Sina Ghaemmaghami, Jan Ihmels, David K. Breslow, Matthew Noble, Joseph L. DeRisi and Jonathan S. Weissman. *Single-cell proteomic analysis of S-cerevisiae reveals the architecture of biological noise.* Nature, vol. 441, no. 7095, page 840846, June 2006. (Cited on page 94.)

[Nickell *et al.* 2006] S. Nickell, C. Kofler, A. P. Leis and W. Baumeister. *A visual approach to proteomics.* Nature Reviews. Molecular Cell Biology, vol. 7, no. 3, pages 225–230, feb 2006. Citation Key: nickell:2006aa tex.bdsk-url-1: %3CGo%20to%20ISI%3E://WOS:000235590500017 tex.date-added: 2018-03-15 08:56:40 +0000 tex.date-modified: 2018-03-15 21:27:08 +0000 tex.type: Journal article tex.url: <Go to ISI>://WOS:000235590500017. (Cited on page 94.)

[Noble *et al.* 2018a] Alex J Noble, Venkata P Dandey, Hui Wei, Julia Brasch, Jillian Chase, Priyamvada Acharya, Yong Zi Tan, Zhening Zhang, Laura Y Kim, Giovanna Scapin, Micah Rapp, Edward T Eng, William J Rice, Anchi Cheng, Carl J Negro, Lawrence Shapiro, Peter D Kwong, David Jeruzalmi, Amedee des Georges, Clinton S Potter and Bridget Carragher. *Routine single particle CryoEM sample and grid characterization by tomography.* eLife, vol. 7, may 2018. (Cited on page 21.)

[Noble *et al.* 2018b] Alex J. Noble, Hui Wei, Venkata P. Dandey, Zhening Zhang, Yong Zi Tan, Clinton S. Potter and Bridget Carragher. *Reducing effects of*

particle adsorption to the air–water interface in cryo-EM. Nature Methods, vol. 15, no. 10, pages 793–795, October 2018. (Cited on pages 20, 21 and 78.)

[Nogales 2015] Eva Nogales. *The development of cryo-EM into a mainstream structural biology technique*. Nature Methods, vol. 13, no. 1, pages 24–27, dec 2015. (Cited on pages 3 and 5.)

[Oomen *et al.* 2018] Pieter E. Oomen, Mohaddeseh A. Aref, Ibrahim Kaya, Nhu T. N. Phan and Andrew G. Ewing. *Chemical Analysis of Single Cells*. Analytical Chemistry, vol. 91, no. 1, pages 588–621, oct 2018. (Cited on pages 25 and 26.)

[Padmakar *et al.* 1999] A. S. Padmakar, Kajari Kargupta and Ashutosh Sharma. *Instability and dewetting of evaporating thin water films on partially and completely wettable substrates*. The Journal of Chemical Physics, vol. 110, no. 3, pages 1735–1744, jan 1999. (Cited on pages 16, 17, 18 and 76.)

[Pan *et al.* 2014] Ning Pan, Wei Rao, Naga Rama Kothapalli, Renmeng Liu, Anthony W. G. Burgett and Zhibo Yang. *The Single-Probe: A Miniaturized Multifunctional Device for Single Cell Mass Spectrometry Analysis*. Analytical Chemistry, vol. 86, no. 19, pages 9376–9380, sep 2014. (Cited on page 26.)

[Pantelic *et al.* 2010] Radosav S. Pantelic, Jannik C. Meyer, Ute Kaiser, Wolfgang Baumeister and Jürgen M. Plitzko. *Graphene oxide: A substrate for optimizing preparations of frozen-hydrated samples*. Journal of Structural Biology, vol. 170, no. 1, pages 152–156, apr 2010. (Cited on page 23.)

[Park *et al.* 2020] Junsun Park, Ji yeon Park, Seowon Lee and Soung-Hun Roh. *Grid selection strategy for high-resolution cryo-EM*. Korean Society for Structural Biology, vol. 8, no. 2, pages 41–48, jun 2020. (Cited on page 23.)

[Petri-Fink *et al.* 2008] Alke Petri-Fink, Benedikt Steitz, Andrija Finka, Jatuporn Salaklang and Heinrich Hofmann. *Effect of cell media on polymer coated superparamagnetic iron oxide nanoparticles (SPIONs): Colloidal stability, cytotoxicity, and cellular uptake studies*. European Journal of Pharmaceutics and Biopharmaceutics, vol. 68, no. 1, pages 129–137, jan 2008. (Cited on page 13.)

[Pettersen *et al.* 2004] Eric F. Pettersen, Thomas D. Goddard, Conrad C. Huang, Gregory S. Couch, Daniel M. Greenblatt, Elaine C. Meng and Thomas E. Ferrin. *UCSF Chimera?A visualization system for exploratory research and analysis*. Journal of Computational Chemistry, vol. 25, no. 13, pages 1605–1612, 2004. (Cited on page 82.)

[Phelps *et al.* 2014] Mandy Phelps, Jason Hamilton and Guido F. Verbeck. *Nanomanipulation-coupled nanospray mass spectrometry as an approach for*

single cell analysis. Review of Scientific Instruments, vol. 85, no. 12, page 124101, dec 2014. (Cited on page 26.)

[Punjani *et al.* 2017] Ali Punjani, John L Rubinstein, David J Fleet and Marcus A Brubaker. *CryoSPARC: Algorithms for rapid unsupervised cryo-EM structure determination*. Nature Methods, vol. 14, no. 3, pages 290–296, feb 2017. (Cited on pages 76 and 82.)

[Raffaini & Ganazzoli 2010] Giuseppina Raffaini and Fabio Ganazzoli. *Protein Adsorption on a Hydrophobic Surface: A Molecular Dynamics Study of Lysozyme on Graphite*. Langmuir, vol. 26, no. 8, pages 5679–5689, apr 2010. (Cited on page 20.)

[Ramakrishnan *et al.* 2014] Chandrasekhar Ramakrishnan, Andrej Bieri, Nora Sauter, Sophie Roizard, Philippe Ringler, Shirley A Müller, Kenneth N Goldie, Kaloyan Enimanev, Henning Stahlberg, Bernd Rinn and Thomas Braun. *openBEB: open biological experiment browser for correlative measurements*. BMC Bioinformatics, vol. 15, no. 1, page 84, 2014. (Cited on pages 11, 34, 60 and 69.)

[Ravelli *et al.* 2020] Raimond B. G. Ravelli, Frank J. T. Nijpels, Rene J. M. Henderikx, Giulia Weissenberger, Sanne Thewessem, Abril Gijsbers, Bart W. A. M. M. Beulen, Carmen López-Iglesias and Peter J. Peters. *Cryo-EM structures from sub-nl volumes using pin-printing and jet vitrification*. Nature Communications, vol. 11, no. 1, may 2020. (Cited on pages 9 and 57.)

[Razinkov *et al.* 2016] Ivan Razinkov, Venkata P. Dandey, Hui Wei, Zhening Zhang, David Melnekoff, William J. Rice, Christoph Wigge, Clinton S. Potter and Bridget Carragher. *A new method for vitrifying samples for cryoEM*. Journal of Structural Biology, vol. 195, no. 2, pages 190–198, aug 2016. (Cited on pages 9 and 78.)

[Razumovsky & Damodaran 1999] Lev Razumovsky and Srinivasan Damodaran. *Surface Activity-Compressibility Relationship of Proteins at the Air-Water Interface*. Langmuir, vol. 15, no. 4, pages 1392–1399, feb 1999. (Cited on page 21.)

[Renaud *et al.* 2018] Jean-Paul Renaud, Ashwin Chari, Claudio Ciferri, Wen ti Liu, Hervé-William Rémigy, Holger Stark and Christian Wiesmann. *Cryo-EM in drug discovery: achievements, limitations and prospects*. Nature Reviews Drug Discovery, vol. 17, no. 7, pages 471–492, jun 2018. (Cited on page 4.)

[Rima *et al.* 2018] Luca Rima, Claudio Schmidli, Stefan A. Arnold, Thomas Stohler, Anastasia Syntychaki, Andrej Bieri, Stefan Albiez, Kenneth N. Goldie, Mo-

hamed Chami, Henning Stahlberg and Thomas Braun. *Miniaturized Sample Preparation for Transmission Electron Microscopy.* Journal of Visualized Experiments, no. 137, page e57310, jul 2018. (Cited on pages 10, 57, 58, 73, 76, 85 and 96.)

[Ripstein & Rubinstein 2016] Z.A. Ripstein and J.L. Rubinstein. *Processing of Cryo-EM Movie Data.* In Methods in Enzymology, pages 103–124. Elsevier, 2016. (Cited on page 33.)

[Rosenthal & Henderson 2003] Peter B. Rosenthal and Richard Henderson. *Optimal Determination of Particle Orientation, Absolute Hand, and Contrast Loss in Single-particle Electron Cryomicroscopy.* Journal of Molecular Biology, vol. 333, no. 4, pages 721–745, oct 2003. (Cited on page 88.)

[Rubinstein *et al.* 2019] John L. Rubinstein, Hui Guo, Zev A. Ripstein, Ali Haydaroglu, Aaron Au, Christopher M. Yip, Justin M. Di Trani, Samir Benlekbir and Timothy Kwok. *Shake-it-off: a simple ultrasonic cryo-EM specimen-preparation device.* Acta Crystallographica Section D Structural Biology, vol. 75, no. 12, pages 1063–1070, nov 2019. (Cited on page 9.)

[Ruskin *et al.* 2013] Rachel S. Ruskin, Zhiheng Yu and Nikolaus Grigorieff. *Quantitative characterization of electron detectors for transmission electron microscopy.* Journal of Structural Biology, vol. 184, no. 3, pages 385–393, dec 2013. (Cited on page 33.)

[Russo & Passmore 2014] Christopher J Russo and Lori A Passmore. *Controlling protein adsorption on graphene for cryo-EM using low-energy hydrogen plasmas.* Nature Methods, vol. 11, no. 6, pages 649–652, apr 2014. (Cited on page 23.)

[Scheres & Chen 2012] Sjors H W Scheres and Shaoxia Chen. *Prevention of overfitting in cryo-EM structure determination.* Nature Methods, vol. 9, no. 9, pages 853–854, jul 2012. (Cited on page 87.)

[Scheres 2012] Sjors H.W. Scheres. *RELION: Implementation of a Bayesian approach to cryo-EM structure determination.* Journal of Structural Biology, vol. 180, no. 3, pages 519–530, dec 2012. (Cited on pages 4 and 33.)

[Schmidli *et al.* 2019] Claudio Schmidli, Stefan Albiez, Luca Rima, Ricardo Righetto, Inayatulla Mohammed, Paolo Oliva, Lubomir Kovacik, Henning Stahlberg and Thomas Braun. *Microfluidic protein isolation and sample preparation for high-resolution cryo-EM.* Proceedings of the National Academy of Sciences, page 201907214, jul 2019. (Cited on pages 10, 12, 13 and 57.)

[Scholz *et al.* 2011] Diana Scholz, Dominik Pöltl, Andreas Genewsky, Matthias Weng,

Tanja Waldmann, Stefan Schildknecht and Marcel Leist. *Rapid, complete and large-scale generation of post-mitotic neurons from the human LUHMES cell line.* Journal of Neurochemistry, vol. 119, no. 5, pages 957–971, apr 2011. (Cited on page 97.)

[Schrader *et al.* 2016] Jil Schrader, Fabian Henneberg, Ricardo A. Mata, Kai Tittmann, Thomas R. Schneider, Holger Stark, Gleb Bourenkov and Ashwin Chari. *The inhibition mechanism of human 20Sproteasomes enables next-generation inhibitor design.* Science, vol. 353, no. 6299, pages 594–598, aug 2016. (Cited on pages 76 and 82.)

[Schrödinger, LLC 2015] Schrödinger, LLC. The PyMOL molecular graphics system, version 1.8. November 2015. (Cited on page 82.)

[Sharma 1993] Ashutosh Sharma. *Relationship of thin film stability and morphology to macroscopic parameters of wetting in the apolar and polar systems.* Langmuir, vol. 9, no. 3, pages 861–869, mar 1993. (Cited on page 16.)

[Sharma 1998] Ashutosh Sharma. *Stability and Breakup of Thin Evaporating Water Films: Role of Hydrophobic Interaction.* Journal of Colloid and Interface Science, vol. 199, no. 2, pages 212–214, mar 1998. (Cited on pages 16, 17 and 18.)

[Shrestha & Vertes 2009] Bindesh Shrestha and Akos Vertes. *In Situ Metabolic Profiling of Single Cells by Laser Ablation Electrospray Ionization Mass Spectrometry.* Analytical Chemistry, vol. 81, no. 20, pages 8265–8271, oct 2009. (Cited on page 27.)

[Slavov 2021] Nikolai Slavov. *Single-cell protein analysis by mass spectrometry.* Current Opinion in Chemical Biology, vol. 60, pages 1–9, feb 2021. (Cited on page 24.)

[Squires & Quake 2005] Todd M. Squires and Stephen R. Quake. *Microfluidics: Fluid physics at the nanoliter scale.* Reviews of Modern Physics, vol. 77, no. 3, pages 977–1026, July 2005. (Cited on page 75.)

[Stark & Chari 2015] Holger Stark and Ashwin Chari. *Sample preparation of biological macromolecular assemblies for the determination of high-resolution structures by cryo-electron microscopy.* Microscopy, vol. 65, no. 1, pages 23–34, dec 2015. (Cited on page 73.)

[Syntychaki *et al.* 2019] Anastasia Syntychaki, Luca Rima, Claudio Schmidli, Thomas Stohler, Andrej Bieri, Rosmarie Sütterlin, Henning Stahlberg and Thomas Braun. *'Differential Visual Proteomics': Enabling the Proteome-Wide Comparison of Protein Structures of Single-Cells.* Journal of Proteome

Research, vol. 18, no. 9, pages 3521–3531, jul 2019. (Cited on pages 24 and 94.)

[Tang *et al.* 2009] Fuchou Tang, Catalin Barbacioru, Yangzhou Wang, Ellen Nordman, Clarence Lee, Nanlan Xu, Xiaohui Wang, John Bodeau, Brian B. Tuch, Asim Siddiqui, Kaiqin Lao and M. Azim Surani. *mRNA-Seq whole-transcriptome analysis of a single cell.* Nature Methods, vol. 6, no. 5, pages 377–382, apr 2009. (Cited on page 94.)

[Taylor & Glaeser 1974] K. A. Taylor and R. M. Glaeser. *Electron Diffraction of Frozen, Hydrated Protein Crystals.* Science, vol. 186, no. 4168, pages 1036–1037, dec 1974. (Cited on pages 3, 6 and 56.)

[Taylor & Glaeser 1976] Kenneth A. Taylor and Robert M. Glaeser. *Electron microscopy of frozen hydrated biological specimens.* Journal of Ultrastructure Research, vol. 55, no. 3, pages 448–456, jun 1976. (Cited on page 73.)

[Taylor & Glaeser 2008] Kenneth A. Taylor and Robert M. Glaeser. *Retrospective on the early development of cryoelectron microscopy of macromolecules and a prospective on opportunities for the future.* Journal of Structural Biology, vol. 163, no. 3, pages 214–223, sep 2008. (Cited on page 19.)

[Thompson *et al.* 2016] Rebecca F. Thompson, Matt Walker, C. Alistair Siebert, Stephen P. Muench and Neil A. Ranson. *An introduction to sample preparation and imaging by cryo-electron microscopy for structural biology.* Methods, vol. 100, pages 3–15, may 2016. (Cited on page 73.)

[Tivol *et al.* 2008] William F. Tivol, Ariane Briegel and Grant J. Jensen. *An Improved Cryogen for Plunge Freezing.* Microscopy and Microanalysis, vol. 14, no. 5, pages 375–379, sep 2008. (Cited on page 6.)

[Veesler *et al.* 2013] David Veesler, Melody G. Campbell, Anchi Cheng, Chi yu Fu, Zachary Murez, John E. Johnson, Clinton S. Potter and Bridget Carragher. *Maximizing the potential of electron cryomicroscopy data collected using direct detectors.* Journal of Structural Biology, vol. 184, no. 2, pages 193–202, nov 2013. (Cited on page 33.)

[Wang & Bodovitz 2010] Daojing Wang and Steven Bodovitz. *Single cell analysis: the new frontier in omics.* Trends in Biotechnology, vol. 28, no. 6, page 281290, June 2010. (Cited on pages 24 and 94.)

[Wang & Sigworth 2010] Liguo Wang and Fred J. Sigworth. *Liposomes on a Streptavidin Crystal: A System to Study Membrane Proteins by Cryo-EM.* In Methods in Enzymology, pages 147–164. Elsevier, 2010. (Cited on page 24.)

[Wei *et al.* 2018] Hui Wei, Venkata P. Dandey, Zhening Zhang, Ashleigh Raczkowski, Willam J. Rice, Bridget Carragher and Clinton S. Potter. *Optimizing "self-wicking" nanowire grids.* Journal of Structural Biology, vol. 202, no. 2, pages 170–174, may 2018. (Cited on page 9.)

[White *et al.* 2003] H.D. White, K. Thirumurugan, M.L. Walker and J. Trinick. *A second generation apparatus for time-resolved electron cryo-microscopy using stepper motors and electrospray.* Journal of Structural Biology, vol. 144, no. 1-2, pages 246–252, oct 2003. (Cited on pages 9 and 57.)

[Wickremsinhe *et al.* 2006] Enaksha Wickremsinhe, Gurkeerat Singh, Bradley Ackermann, Todd Gillespie and Ajai Chaudhary. *A Review of Nanoelectrospray Ionization Applications for Drug Metabolism and Pharmacokinetics.* Current Drug Metabolism, vol. 7, no. 8, pages 913–928, dec 2006. (Cited on page 26.)

[Widom 2004] Benjamin Widom. *Capillarity and Wetting Phenomena: Drops, Bubbles, Pearls, Waves Capillarity and Wetting Phenomena: Drops, Bubbles, Pearls, Waves , Pierre-Gilles de Gennes , Françoise Brochard-Wyart , and David Quéré (translated from French by Axel Reisinger) Springer-Verlag, New York, 2004. $69.95 (291 pp.). ISBN 0-387-00592-7.* Physics Today, vol. 57, no. 12, pages 66–67, dec 2004. (Cited on page 16.)

[Yang *et al.* 2017] Yunyun Yang, Yanying Huang, Junhui Wu, Ning Liu, Jiewei Deng and Tiangang Luan. *Single-cell analysis by ambient mass spectrometry.* TrAC Trends in Analytical Chemistry, vol. 90, pages 14–26, may 2017. (Cited on pages 25, 26 and 27.)

[Yip *et al.* 2020] Ka Man Yip, Niels Fischer, Elham Paknia, Ashwin Chari and Holger Stark. *Breaking the next Cryo-EM resolution barrier – Atomic resolution determination of proteins!* may 2020. (Cited on page 56.)

[Yoshimura *et al.* 1994] Hideyuki Yoshimura, Tschangiz Scheybani, Wolfgang Baumeister and Kuniaki Nagayama. *Two-Dimensional Protein Array Growth in Thin Layers of Protein Solution on Aqueous Subphases.* Langmuir, vol. 10, no. 9, pages 3290–3295, sep 1994. (Cited on page 20.)

[Young 1805] Thomas Young. *III. An essay on the cohesion of fluids.* Philosophical Transactions of the Royal Society of London, vol. 95, pages 65–87, dec 1805. (Cited on page 14.)

[Yu *et al.* 2014] Zhan Yu, Lee Chuin Chen, Satoshi Ninomiya, Mridul Kanti Mandal, Kenzo Hiraoka and Hiroshi Nonami. *Piezoelectric inkjet assisted rapid electrospray ionization mass spectrometric analysis of metabolites in plant single cells via a direct sampling probe.* The Analyst, vol. 139, no. 22, pages

5734–5739, 2014. (Cited on page 26.)

[Yu *et al.* 2016] Guimei Yu, Kunpeng Li and Wen Jiang. *Antibody-based affinity cryo-EM grid.* Methods, vol. 100, pages 16–24, May 2016. (Cited on pages 24 and 78.)

[Zemlin 1994] F. Zemlin. *Expected contribution of the field-emission gun to high-resolution transmission electron microscopy.* Micron, vol. 25, no. 3, pages 223–226, jan 1994. (Cited on page 33.)

[Zhang *et al.* 2014] Linwen Zhang, Daniel P. Foreman, Paaqua A. Grant, Bindesh Shrestha, Sally A. Moody, Florent Villiers, June M. Kwak and Akos Vertes. *In Situ metabolic analysis of single plant cells by capillary microsampling and electrospray ionization mass spectrometry with ion mobility separation.* The Analyst, vol. 139, no. 20, pages 5079–5085, jul 2014. (Cited on page 26.)

[Zheng *et al.* 2017] Shawn Q Zheng, Eugene Palovcak, Jean-Paul Armache, Kliment A Verba, Yifan Cheng and David A Agard. *MotionCor2: anisotropic correction of beam-induced motion for improved cryo-electron microscopy.* Nature Methods, vol. 14, no. 4, pages 331–332, April 2017. (Cited on page 81.)

[Zimmermann 2020] Michael Zimmermann. Structural investigation of LRRK2 with microfluidic sample preparation for high-resolution cryo-EM. Master's thesis, University of Basel, November 2020. (Cited on page 109.)

[Zivanov *et al.* 2018] Jasenko Zivanov, Takanori Nakane, Björn O Forsberg, Dari Kimanius, Wim JH Hagen, Erik Lindahl and Sjors HW Scheres. *New tools for automated high-resolution cryo-EM structure determination in RELION-3.* eLife, vol. 7, nov 2018. (Cited on pages 76 and 82.)